

## ABSTRACT

### BEAM MANIPULATION AND ACCELERATION WITH DIELECTRIC-LINED WAVEGUIDES

François Lemery, Ph.D.  
Department of Physics  
Northern Illinois University, 2015  
Philippe Piot, Director

The development of next-generation TeV+ electron accelerators will require either immense footprints based on conventional acceleration techniques or the development of new higher-gradient acceleration methods. One possible alternative is beam-driven acceleration in a high-impedance medium such as a dielectric-lined-waveguide (DLW), where a high-charge bunch passes through a DLW and can excite gradients on the order of GV/m. An important characteristic of this acceleration class is the transformer ratio which characterizes the energy transfer of the scheme. This dissertation discusses alternative methods to improve the transformer ratio for beam-driven acceleration and also considers the use of DLWs for beam manipulation at low energy.

NORTHERN ILLINOIS UNIVERSITY  
DE KALB, ILLINOIS

JUNE 2015

**BEAM MANIPULATION AND ACCELERATION  
WITH DIELECTRIC-LINED WAVEGUIDES**

BY

FRANÇOIS LEMERY  
© 2015 François Lemery

A DISSERTATION SUBMITTED TO THE GRADUATE SCHOOL  
IN PARTIAL FULFILLMENT OF THE REQUIREMENTS  
FOR THE DEGREE  
DOCTOR OF PHILOSOPHY

DEPARTMENT OF PHYSICS

Dissertation Director:  
Philippe Piot

## ACKNOWLEDGEMENTS

I am forever grateful to my family who has supported me to freely pursue my passion; without your support and encouragement, this work may not have been realised. I am also grateful to the teachers and professors who've opened my mind to the big picture, in the order of your appearance in my life: Robert Miller, Johann Rafelski, Steve Steinke, Alan Cooney, Drew Milsom, John Rutherford, Ken Johns, Michael Shupe, Stephen Martin, David Hedin, and Roland Winkler. And additionally to Leon Lederman, Kip Thorne, and Alan Guth whose popular books helped establish my reasoning. Finally I am eternally indebted to my excellent adviser and friend Philippe Piot, thank you for the opportunity to pursue this work, your support and valuable insight significantly improved my capabilities and also helped me see that anything is truly possible. Finally, I thank the third member of my PhD committee, Vladimir Shiltsev for his valuable suggestions and feedback on my dissertation.

This work was supported by the Defense Threat Reduction Agency, Basic Research Award # HDTRA1-10-1-0051, to Northern Illinois University and a Dissertation Completion Award granted by the Graduate School of Northern Illinois University. Part of the work was carried at Fermi National Accelerator Laboratory which is operated by the Fermi Research Alliance, LLC under Contract No. DE-AC02-07CH11359 with the United States Department of Energy.

## DEDICATION

For mankind.



# TABLE OF CONTENTS

	Page
List of Tables . . . . .	vii
List of Figures . . . . .	viii
Chapter	
1 Introduction . . . . .	1
2 Theory of Dielectric-Lined Waveguides . . . . .	3
2.1 Cylindrically-symmetric DLW . . . . .	5
2.2 Slab-symmetric DLWs . . . . .	7
2.3 Alternative slab-symmetric formulation . . . . .	9
2.4 Computation and simulation . . . . .	11
3 Beam-Driven Acceleration . . . . .	14
3.1 Transformer ratio . . . . .	14
3.2 Smooth Shapes . . . . .	17
3.2.1 Linear ramp with sinusoidal head . . . . .	18
3.2.2 Linear ramp with parabolic head . . . . .	20
3.2.3 Comparison with other shapes . . . . .	22
3.3 Photoemission of optimal shapes via laser-shaping . . . . .	23
3.3.1 Case of an ideal laser-shaping technique . . . . .	24
3.3.2 Limitation of a practical laser shaping technique . . . . .	30
3.4 Formation of high-energy tailored bunches for a DWFA LINAC . . . . .	33

Chapter		Page
3.5	Experimental Generation and Characterization of Electron Bunches with Ramped Current Profiles in a Dual-Frequency Superconducting Linear Accelerator . . . . .	39
3.6	Flat-beams for DWFA . . . . .	46
3.7	Experimental Opportunity for DWFA at FAST . . . . .	49
3.8	Start-to-end simulations . . . . .	51
3.8.1	Case of single-mode DLW structures . . . . .	51
3.8.2	Case of multi-mode DLW structures . . . . .	52
4	Ballistic bunching and beam manipulation . . . . .	61
4.1	Introduction . . . . .	61
4.2	Ballistic compression from wakefield-induced energy modulations . . . . .	62
4.3	Numerical modeling and analysis . . . . .	68
4.3.1	Sub-picosecond bunch train formation . . . . .	69
4.3.2	Passive Bunching . . . . .	77
4.3.3	Shaping . . . . .	81
4.4	SUMMARY . . . . .	83
5	Applications . . . . .	85
5.1	THz via Echo-Enabled Harmonic Generation at Low-energy . . . . .	85
5.2	Compact X-ray source . . . . .	88
5.3	Cascaded Acceleration . . . . .	89
5.3.1	Ballistic bunching using a DLW . . . . .	90
5.3.2	Acceleration with compressed bunch . . . . .	91
5.3.3	Selection of accelerated population . . . . .	93

Chapter	Page
5.4 Experimental investigation of THz-pulse propagation in a slab-symmetric dielectric structure . . . . .	94
5.4.1 Simulation and Analysis of a THz pulse propagation in a SLAB DLW . . . . .	94
5.5 Experimental setup . . . . .	97
5.6 Preliminary experimental results. . . . .	101
5.7 THz-based electron gun . . . . .	101
5.7.1 Dispersion Controlled Acceleration . . . . .	103
5.8 Conclusion . . . . .	105
6 Conclusion . . . . .	107
References. . . . .	109
Appendix: PERFORMANCES OF VORPAL-GPU SLAB-SYMMETRIC DLW . . . . .	119

## LIST OF TABLES

Table		Page
3.1	Table comparing several different proposed drive bunch distributions as a function of bunch length and charge. Additionally, the maximum decelerating field ( $E_-^m$ ) is shown for each distribution. Here we consider $\kappa = 1$ . 24	
3.2	Optimized settings for the accelerator parameters needed to produce and accelerate a ramp bunch to $\sim 200$ MeV. The parameter $\alpha$ and $\tau$ are defined in Eq. 3.26. . . . .	35
3.3	Dielectric-line waveguide (DLW) parameters and resulting wakefield values using the current profile shown in Fig 3.12. The “ideal-” and “realistic-compression” entries respectively correspond to the cases when the final current profile is obtained via a simple longitudinal-axis scaling or via particle tracking. . . . .	38
3.4	Settings of accelerator subsystems relevant to the LPS dynamics used in the experiment and simulations. . . . .	43
4.1	Beamline settings and DLW-structure parameters used in the ASTRA simulations. The beamline configuration with some of the associated parameters is depicted in Fig. 4.3. . . . .	70
5.1	Accelerator beamline settings and DLW parameters used in the ASTRA simulations. The relative modes amplitude are normalized to the square sum of the amplitudes. . . . .	90
5.2	Parameters associated to single and multi-mode structure for central-bunching. 105	
A.1	Cartesian grid dimensions and volumes used in this scaling study. . . . .	124

## LIST OF FIGURES

Figure		Page
2.1	A cylindrically-symmetric (a) and slab-symmetric (b) dielectric-lined waveguide (DLW) are shown. In both cases, a dielectric thickness of $b - a$ is surrounded by a metallic jacket; an electron bunch is shown exiting each DLW after inducing a longitudinal electric field (shown as red and blue contours).	4
2.2	The slab-symmetric DLW in Bernhard's formulation; the full dielectric dimension width has length $a$ , the two dielectric slabs have a thickness $t$ , and the transverse open dimension has length $b$ . . . . .	10
2.3	Dispersion relation for the LSM mode for the Bernhard formalism for a structure with parameters $(a, b, t, \epsilon) = (1 \text{ mm}, 1 \text{ cm}, 200 \text{ }\mu\text{m}, 5.7)$ . The diagonal red line corresponds to the speed of light. . . . .	11
2.4	Wake function computed as $w_z(\zeta) = \sum_{l=1}^m w_{z,l}$ for $m = 1, 2, 4, 8$ , and 16 for a DLW structure with parameters $a = 400 \text{ }\mu\text{m}$ , $b = 450 \text{ }\mu\text{m}$ , and $\epsilon_r = 5.7$ . The fundamental-mode (blue trace) wavelength is $\lambda_1 \simeq 1.09 \text{ mm}$ . . . . .	13
3.1	The longitudinal accelerating field is shown for the ramped bunch for a cylindrical structure with parameters $(a, b, \epsilon) = (165 \text{ }\mu\text{m}, 195 \text{ }\mu\text{m}, 5.7)$ . Arrows indicate the maximum accelerating and decelerating fields ( $E_+$ , $E_-$ respectively) and hence the transformer ratio of $\sim 6$ from a bunchlength of $\sim 1.5\lambda$ . . . . .	16
3.2	Example of current profiles described by Eq. 3.8 (shaded line) with the corresponding induced voltages. The parameters are $n = 0$ , $N = 5$ , and plots (a) and (b) respectively correspond to the cases $q = 2$ and $q = 3$ . The head of the bunch is at $kz = 0$ . . . . .	20
3.3	Example of ideal "quadratic" current profiles given by Eq. 3.15 (shaded line) with corresponding induced voltage. The parameters are $\nu = 1$ , and $N = 5$ . The head of the bunch is at $kz = 0$ . . . . .	22

Figure		Page
3.4	Tradeoff curves between $\mathcal{R}$ and $E_+^m$ for the current profiles listed in Tab. 3.1. The “quadratic” and “sin ramps” respectively correspond to the distributions proposed in Sections 3.2.2 and 3.2.1. The Gaussian and ramp distributions are displayed for comparison. This was generated by fixing the charge $Q$ and varying the scaling parameter $a$ . . . . .	25
3.5	Configuration used for the pulse-shaping simulations using a S-band RF gun (a). A temporally shaped laser pulse (b) is optimized to result in a photo-emitted electron-beam with current profile (c) having features similar to the distribution discussed in Sec. 3.2.2. In insets (a) and (b) the tail of the bunch is at $t = 0$ . . . . .	26
3.6	Inverted parabola distribution (black trace), and corresponding electrostatic potential (red trace), electric field (blue trace) and resulting force (blue trace) as a function of the longitudinal coordinate. . . . .	27
3.7	Charge distribution (black trace), and corresponding electrostatic potential (red trace), electric field (blue trace) and resulting force field (blue trace) for $n = 1$ (top), $n = 2$ (middle), and $n = 5$ (bottom). . . . .	29
3.8	Evolution of the electron-bunch current (a) and longitudinal phase space (b) along the beamline at 20 (red), 60 (green), and 100 cm (blue) from the photocathode surface and (c) comparison of the current profile numerically simulated at $s = 50$ cm (red trace) with a fit to equation Eq. 3.15 (blue lines). The head of the bunch is at large values of $z$ . . . . .	30
3.9	Comparison of nominal (“ideal”) shape with the shapes achieved when taking into account the photoemission response time (“cathode”), the laser-pulse-shaping finite bandwidth (“shaping”) and both effects (“cathode + shaper”). The ideal laser temporal profile is described by Eq. 3.26 with $\alpha = 2$ and $\tau = 15$ ps. Insets (b) and (c) are zooms of the areas $t \in [-15200, -13600]$ fs (peak location) and $t \in [-16000, -15020]$ fs (left edge of the profile) respectively. The head of the laser pulse is at $t = 0$ . . . . .	32
3.10	Comparison of the final electron-bunch current at $s = 50$ cm from the cathode surface for the four cases considered in Fig. 3.9. The “cathode” and “shaper” respectively correspond to the inclusion of the cathode response time and shaper bandwidth limitation in the initial particle distribution at $s = 0$ while the ideal case is given by by Eq. 3.26 with $\alpha = 2$ and $\tau = 15$ ps. The head of the bunch corresponds to $z > 0$ . . . . .	33

Figure		Page
3.11	Block diagram of the accelerator configuration explored for the formation of high-energy ramped bunches. The legend is as follows: “QW” stands for quarter-wave, “L0” and “L1” are standard 1.3-GHz cryomodule equipped with 8 TESLA-type SCRF cavities, “L39” is a cryomodule consisting of four 3.9-GHz cavities, and “BC” is a magnetic bunch compressor. . . . .	34
3.12	Final current distribution (green shaded area) and associated wakefield (blue traces) for the “ideal” (a) and “realistic” (b) cases of compression discussed in the text. The head of the bunch corresponds to $z = 0$ . . . . .	36
3.13	Snapshots of the longitudinal phase spaces and associated current profiles (red traces) upstream of L0 (a) and downstream of L0 (b), L39 (c) and BC (d). Simulations up to L39 are carried with ASTRA whereas a one-dimensional longitudinal-dynamics model is used for BC2. The head of the bunch corresponds to $z > 0$ . . . . .	37
3.14	Analytically-computed current profiles for several values of $b_f$ for fixed $a_f = 2.5$ (a) and for several values of $a_f$ with $b_f = 0.7$ (b). The numbers in (a) [resp. (b)] are the values of $b_f$ [resp. $a_f$ ]; for all the cases $\sigma_u = 0.05$ . . . . .	42
3.15	Diagram of the FLASH facility. Only components affecting the longitudinal phase space beam (LPS) dynamics of the bunches are shown. The acronyms ACC, BC, and DBL stand respectively for accelerating modules, bunch compressors, and dogleg beamline (the blue rectangles represent dipole magnets). The transverse deflecting structure (TDS), spectrometer and Ce:YAG screen compose the LPS diagnostics. . . . .	44
3.16	Simulated LPS distribution [(a) and (b)] with associated current profile downstream of BC1 (solid blue trace) and DBL (dash red trace) [(c) and (d)]. The set of plots [(a), (c)] and [(b), (d)] correspond to different $(V_{1,3}, \varphi_{1,3})$ settings. . . . .	45
3.17	Snapshots of the measured longitudinal phase spaces (left column) and associated current profiles (right column) for different settings of the ACC1 and ACC39 accelerating modules. The values $(V_1, \varphi_1; V_3, \varphi_3)$ [in (MV, °, MV, °)] are: (150.5, 6.1; 20.7, 3.8), (156.7, 3.8; 20.8, 168.2), (155.6, 3.6; 20.6, 166.7), and (156.8, 4.3; 20.7, 167.7) for respectively case (a), (b), (c), and (d).. . . .	54
3.18	Cylindrical-symmetric dielectric-loaded waveguide considered (a) and axial wakefield produced by the current profile shown in Fig. 3.17 (c) for $(a, b)=(20,60)$ $\mu\text{m}$ . . . . .	55

Figure		Page
3.19	Simulated transformer ratio versus peak accelerating field (a) for the four measured current profiles (displayed as different colors with label corresponding to cases shown in Fig. 3.17). Transformer ratio (false color map) as a function of the DLW inner radius $a$ and dielectric layer thickness $b - a$ with corresponding $ E^+ $ shown as isoclines with values quoted in MV/m for case (c) of Fig. 3.17. . . . .	55
3.20	Peak accelerating electric field (blue trace) and transformer ratio (red trace) as a function of emittance ratio $\rho = \varepsilon_n^+ / \varepsilon_n^-$ for a 1 nC electron bunch with 4D emittance $\varepsilon_n^u \equiv \varepsilon_n^+ \varepsilon_n^- = 5 \mu\text{m}$ . The structure parameters is $a = 165 \mu$ and $b - a = 30 \mu\text{m}$ (top) and taken to be variable such that $a = 4\sigma_y$ and $b - a = 30 \mu\text{m}$ (bottom). The bunch is taken to be linearly-ramped with total length of 1.2 mm. . . . .	56
3.21	Required normalized transverse emittance ( $\mu\text{m}$ colorscale) as a function of $\beta^*$ function and DLW structure length. The DLW inner aperture is taken to be $a = 165 \mu\text{m}$ and the beam Lorentz factor is $\gamma = 500$ . . . . .	57
3.22	Layout of the FAST photoinjector. L1 and L2 are solenoids, and CAV1 and 2 SCRF cavities. The red and green rectangle represent quadrupole magnets. X124 is a Ce:YAG screen . . . . .	58
3.23	The zero-charge betatron functions (left) and the transverse RMS beam sizes (right) along the FAST accelerator with flat beams. . . . .	59
3.24	Longitudinal phase spaces (a,c) and associated transverse distributions at X124 (b,d) without (a,b) and with (c,d) a DLW structure. The DLW structure used for (c,d) has parameters $a=100 \mu\text{m}$ , $b = 120 \mu\text{m}$ , and $\varepsilon_r = 5.7$	59
3.25	Longitudinal phase spaces (a,c) and associated transverse distributions at X124 (b,d) for a dielectric thickness of $\delta = 50$ (a,b) and $100 \mu\text{m}$ (c,d) DLW structure. The DLW structure other parameters are $a = 100 \mu\text{m}$ , $b = a + \delta$ , and $\varepsilon_r = 5.7$ . . . . .	60
4.1	Charge distributions (top) and corresponding wake potential (bottom) for the same structure parameters as shown in Fig. 2.4 and for a 1-nC Gaussian bunch with variance (Gaussian distribution) or hard-edge half size (other distributions) of 1 mm. The green, blue, red, and turquoise traces respectively correspond to the case of a Gaussian, parabolic, uniform, and linearly-ramped current distributions. The head of the bunch is at $z \leq 0$ . . . . .	63



Figure		Page
4.2	Charge distributions (a) and corresponding wake potential (b) for two cases of ratio between the rms bunch length $\sigma_z$ and fundamental-mode wavelength $\lambda_1$ . The DLW structure parameters are identical to one used in Fig. 2.4. The head of the bunch corresponds to $z \leq 0$ . The wake potential associated to the $\sigma_z = 0.5\lambda_1$ case is scaled by a factor 50 for clarity. . . . .	65
4.3	Overview of the photoinjector setup used for the numerical simulations. The distances $Z_{SOL}$ and $Z_{DLW}$ correspond respectively to the location of the center of the solenoid and DLW structure referenced to the photocathode surface, and $Z_{drift}$ represents the drift distance downstream of the DLW structure necessary for ballistic bunching. . . . .	67
4.4	Bunch form factor (BFF) (a) and bunch longitudinal density (b) evolution as a function of the drift length referenced with respect to the DLW exit. The simulations correspond to the parameters listed under the “S-band” column in Tab. 4.1. . . . .	71
4.5	Current profiles (a) and associated longitudinal phase spaces (LPS) (b) simulated at the exit of the DLW (blue trace) and at the location of maximum bunching (red trace) $z = 1.3$ m from the photocathode. Bunch form factor (BFF) (c) obtained at $z = 1.3$ m from the photocathode. The simulations correspond to the parameters listed under the “S-band” column in Tab. 4.1. . . . .	72
4.6	Current profiles (a) and associated longitudinal phase spaces (LPS) (b) simulated at maximum compression 31 cm downstream of the DLW (red traces) and at the location of slight over-compression 52 cm downstream of the DLW (blue traces). Bunch form factor (BFF) (c) obtained at the similar locations. The simulations correspond to the parameters listed under the “S-band” column in Tab. 4.1 with the exception of the geometric parameters of the DLW structure selected to be $a = 350 \mu\text{m}$ , and $b = 393 \mu\text{m}$ . . . . .	74
4.7	Transverse horizontal $\sigma_x$ and vertical $\sigma_y$ rms beam sizes (a), corresponding transverse emittances (b) and bunch form factor (BFF) (c) evolution along the beamline. The BFF is evaluated at $f_1 = 1$ THz (blue trace) and at the second (green trace) and third (red trace) harmonics. The simulations correspond to the parameters listed under the “S-band” column in Tab. 4.1. . . . .	75
4.8	Bunch form factor (BFF) (a) and bunch longitudinal density (b) evolution as a function of the drift length referenced with respect to the DLW exit. The simulations correspond to the parameters listed under the “L-band” column in Tab. 4.1. . . . .	76

Figure		Page
4.9	Maximum peak current as function of the fundamental-mode wavelength $\lambda_1$ . The observed noise comes from numerical errors in precisely determining the value of the the axial position where the peak current is maximized. These simulations are carried with the beam parameters summarized in Tab. 4.1 “L-band” column but for a DLW structure with inner radius $a = 650 \mu\text{m}$ . The fundamental-mode wavelength is varied by changing the structure outer radius $b$ . . . . .	78
4.10	Current profiles (a) and longitudinal phase spaces (LPS) (b) at the entrance of the DLW structure (red traces) and at location of maximum compression (blue traces). The simulation correspond to the case $\lambda = 2.06 \text{ mm}$ in Fig. 4.9. The inset in plot (a) corresponds to a zoom of plot (a) around the $\sim 12\text{-kA}$ peak with its origin of the temporal axis corresponding to $z = 0.693 \text{ mm}$ in plot (a) axial coordinate. Maximum bunching, in this scenario occurs $43.9 \text{ cm}$ downstream of the DLW. . . . .	79
4.11	Example of bunch-tail (left) and central (right) bunching. For each cases, the current (top) and longitudinal phase space (bottom) are shown immediately downstream of the DLW (red trace), and $1.2 \text{ m}$ (left) or $1.13 \text{ m}$ (right) downstream of the DLW (blue trace). . . . .	80
4.12	Current profiles (a) and longitudinal phase spaces (b) at the entrance (red traces) and exit (red traces) of the DLW structure and $0.2\text{-m}$ downstream of the structure ( $s \simeq 0.54 \text{ m}$ from the photocathode surface) where a quasi-linear current profile is achieved (green traces). . . . .	82
4.13	Longitudinal wakefield (blue trace) produced behind a bunch with the longitudinal distribution (green trace) identical to the one shown in Fig. 4.12 [plot (a), green trace] for a bunch charge of $1 \text{ nC}$ . The structure used for the wakefield generation has the geometric parameters $a = 165 \mu\text{m}$ , $b = 197 \mu\text{m}$ and $\varepsilon_r = 5.7$ . . . . .	83
5.1	Generation of EEHG with two DLWs: A plateau distribution is shown immediately before (red trace) and after (blue trace) passing through a DLW with $f_0^{(1)} = 0.6 \text{ THz}$ (top left). A snapshot of the bunch after a $1.6 \text{ m}$ drift (top right) before entering the second DLW with $f_0^{(2)} = 0.4 \text{ THz}$ . Finally, the bunch is shown immediately after the second DLW (lower left), and after a $25 \text{ cm}$ drift (lower right). In each figure the longitudinal phase space and current distributions are shown (as lower and upper sub-plots respectively). . . . .	87

Figure		Page
5.2	BFF evolution downstream of the second DLW for the same configuration as presented in Fig. 5.1. . . . .	87
5.3	Overview of the compact source scheme: a photoinjected electron bunch passes through a series of DLWs for cascaded acceleration, the resulting high energy electrons are used with a laser to generate inverse Compton scattering. . . . .	88
5.4	Longitudinal phase spaces (b) and current projection (a) before (red) and after (blue) DLW1 (with parameters listed in Tab. 5.1). The tail of the bunch corresponds to $z < 0$ . . . . .	91
5.5	Longitudinal wake generated at the location of the second DLW (blue trace) from corresponding current (green trace). The tail of the bunch corresponds to $z < 0$ . . . . .	92
5.6	Longitudinal phase space (b) and current projection (a) of before (red) and after (blue) cascaded acceleration. The tail of the bunch corresponds to $z < 0$ . . . . .	93
5.7	Dispersion relation associated to the LSM modes in a slab-symmetric DLW with parameter $a = 100 \mu m$ and $b = 120 \mu m$ . The red diagonal line correspond to $k_z = \omega c$ . . . . .	95
5.8	A diagram of the slab from the x-transverse direction (a) and the from the z-longitudinal direction (b). The slab is composed of a dielectric coating with dielectric permittivity $\epsilon_r$ surrounded by a perfectly conductive boundary (PCB). In the VORPAL simulation, we inject the THz pulse using a current $\vec{J}$ to drive a short pulse in z. Lastly, to remove reflections and to artificially produce the pulse leaving the structure we implement a perfectly matched layer (PML). We record the signal on axis, near the PML. . . . .	95
5.9	Fourier transform of the pulse at the entrance of the structure $ E_y(x = 0, y = 80 \mu m, z = 0, f) $ (top) and a Fourier transform of the pulse at the end of the structure $ E_y(x = 0, y = 80 \mu m, z = 2 cm, f) $ (bottom). . . . .	96
5.10	Frequency-time maps for the 1.4 THz (top) and 1.6 THz (bottom) components of the signal transmitted through the structure. . . . .	98
5.11	Schematic of the A0 laser system. A Ti:Saph “Octavius” laser oscillator outputs 81.25 MHz 150 fs pulses and is regeneratively amplified to $\sim 4$ mJ per pulse. The amplified laser is used to generate photoelectrons and also in our laser-based THz-generation scheme. . . . .	99

Figure	Page
5.12 Experimental setup; an 800 nm laser comes from the right onto a beam splitter; 95% is used for the tilted wavefront THz generation; the rest of the beam passes through a delay stage before being recombined for EO detection. ....	100
5.13 Data of the unbalanced EO detection (left) and its corresponding spectrum (right). ....	101
5.14 Unbalanced EO signal as a function of probe delay in mm. We show two inner gap results of 1.5 mm and 2 mm where there is noticable slower group velocity in the smaller structure. ....	102
5.15 Section, top view and side view (respectively on top, bottom left and top right) of the proposed “THz gun” electron source. ....	103
5.16 A transverse view of a dielectric loaded waveguide (DLW). ....	104
5.17 A transverse view of a dielectric loaded waveguide (DLW). ....	104
5.18 The inner radius of the structure shown as a function of longitudinal coordinate for the numerical solution discussed above. ....	105
A.1 A diagram of the slab seen from the y-transverse direction (a) and the from the x-longitdinal direction (b). The slab is composed of a dielectric coating with dielectric permittivity $\epsilon_r$ surrounded by a PCB. In the VORPAL simulation, we use a wave launcher to drive a short pulse in z. Lastly, to remove reflections and to artificially produce the pulse leaving the structure we implement a PML. We record the signal on axis, near the PML. ....	122
A.2 Strong and weak scaling of VORPAL-GPU on GAIA. On the horizontal, N GPU refers to the number of GPUs used for a given simulation (see below for list). The vertical axis shows the inverse of the time per step. ....	124
A.3 Comparison plot between VORPAL-GPU and an analytical code. The small and medium volume sizes correspond to the first two volumes in Tab. tab:gridsize. The structure has dimensions $a = 100\mu m$ with $b = 120\mu m$ with $\epsilon = 5.7$ . ...	126
A.4 A contour plot of the simulation carried out with VORPAL-GPU shown from a slice in $z=0$ plane on a L grid volume. A gaussian bunch ( $1nC$ , $\sigma_x = 100\mu m$ ) passes through a dielectric structure exciting a wake. The transverse-extended shape corresponds to the combination of the LSE and LSM modes. The peak accelerating field (blue) corresponds to 150 MV/m. The structure has dimensions $a = 100\mu m$ with $b = 120\mu m$ with $\epsilon = 5.7$ . ....	126

# CHAPTER 1

## INTRODUCTION

The development of particle accelerators has led to an incredible wave of advancements across many fields in science and technology. From the first accelerators developed by John Cockroft and Ernest Walton in 1930, which led to the Nobel Prize (1951) winning experiment for splitting the atom, to the recent discovery of the Higgs boson in Large Hardon Colliders (LHC) Run #1, particle accelerators have been essential to the development of fundamental physics and ultimately, the Standard Model. In particle physics we are generally interested in probing higher-energy mechanisms which require correspondingly large collision energies; a modern collider like the LHC has a design center-of-mass collision energy of 14 TeV and is quite expensive; a recent estimate put the total cost of finding the Higgs boson to  $\sim \$13.25BN$  (see [1, 2, 3] for more detailed costs pertaining to accelerators). Accelerators have more recently also become essential tools to explore other fundamental sciences like biology and chemistry where the development of modern electron-based light sources can generate high-repetition rate X-ray pulses to image biological and chemical reactions on ultra-fast timescales.

The relatively small mass of the electron (511 keV) compared to the proton (938 MeV) generally increases the difficulty of producing energetic electron beams due to the increase in synchrotron-radiation power losses which scale as  $\gamma^4$ ; where the Lorentz factor  $\gamma = \frac{E}{mc^2}$ . Therefore, state-of-the-art electron beams are generally produced in linear accelerators (or linacs). In a linac, unlike circular machines, a bunch of charged particles only passes through an accelerating structure once: it is not recirculated. This significantly increases the cost per energy. Additionally, conventional accelerating structures based on the radiofrequency

(RF) technology have limited acceleration gradients of  $\sim 100$  MV/m. Superconducting radiofrequency (SRF) technology provides much more efficient acceleration at significantly higher repetition rates, but their acceleration gradients are limited to 35 MV/m and also require costly cooling infrastructure. These complications have motivated research into other alternative particle acceleration techniques which are generally divided into two categories using laser-based and beam-driven approaches. In the former methods, a high power laser is used to excite a plasma which leads to acceleration gradients on the order of GV/m. In beam-driven approaches [4], a high-charge “drive” bunch passes through a high-impedance medium and loses energy to an electromagnetic wake; a properly delayed “witness” bunch can experience large acceleration gradients from this wake. The techniques are limited by repetition rates of power of high-power lasers and the required high-energy accelerator infrastructures in beam-driven schemes.

In this dissertation, we cover several topics involving dielectric-lined waveguides (DLW) for beam acceleration and manipulation which can lead to improvements in beam-driven acceleration. We begin in chapter 2, with a quantitative description of cylindrically-symmetric and slab-symmetric dielectric lined waveguides. In chapter 3 we review the transformer ratio in detail, and also discuss alternative longitudinal shapes and shaping techniques to improve the efficiency of beam-driven technique. In Chapter 4 we discuss the use of DLWs for ballistic bunching and beam manipulation. In Chapter 5 we discuss several applications of our work and include an experimental portion consisting of the development of a laser-based THz source for the characterization of a slab-symmetric DLW which was to be used in an experiment at Fermilab Accelerator Science and Technology (FAST) facility in a beam-driven experiment. We also include a preliminary investigation into a THz-based electron gun which would match the phase and group velocities with an accelerating low-energy electron bunch. Such a “THz-gun” is based on a longitudinally tailored DLW structure to control the dispersion of a THz pulse.

## CHAPTER 2

### THEORY OF DIELECTRIC-LINED WAVEGUIDES

Most of the work discussed in this dissertation involves dielectric-lined waveguides (DLW). Generally, dielectric-lined waveguides are normal conducting waveguides with a thin dielectric coating on the interior of the waveguide; the dielectric coating serves as an impedier to slow down a traveling electromagnetic wave. DLWs can generally take any geometry, however we will mostly focus on cylindrically-symmetric and slab-symmetric geometries for beam-driven acceleration. In a cylindrical-symmetric DLW is a hollow dielectric cylinder surrounded in a conducting sleeve. A slab-symmetric DLW consists of two dielectric slabs usually placed in parallel with a conductive coating on the outside slab surfaces. In Fig. 2.1, we show an electron “drive” bunch passing through each geometry and exciting an electromagnetic wake; the red and blue contour traces correspond to the longitudinal accelerating field; a properly delayed “witness” bunch can be accelerated in such a wake.

Both geometries offer their own distinct advantages; the closed, cylindrical geometry offers the largest accelerating field; while the open, slab geometry allows for a tunable aperture which directly influences the fundamental wavelength of the waveguide. Generally, a single charge passing through such a single-mode DLW with fundamental wavelength  $\lambda$  will generate a longitudinal wake of the form

$$W_z(z) = \kappa \cos kz \tag{2.1}$$

where  $\kappa$  is the loss factor attributed to the attenuation of a mode in the DLW and depends on geometrical and material properties; and  $k = 2\pi/\lambda$  (see Ref. [5]). It is worth

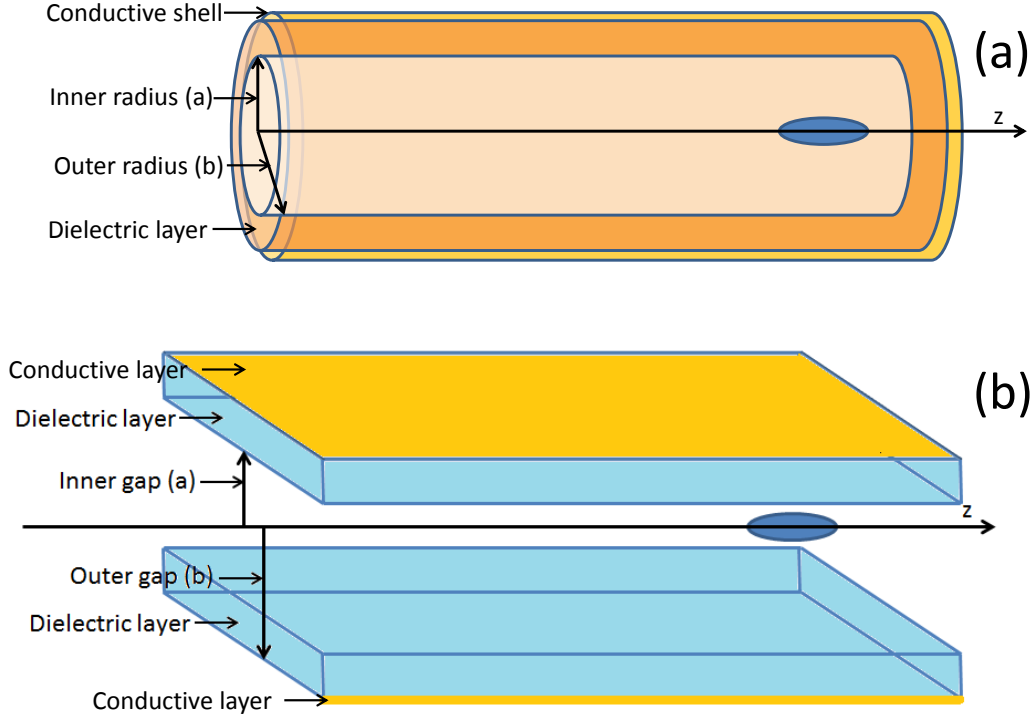


Figure 2.1: A cylindrically-symmetric (a) and slab-symmetric (b) dielectric-lined waveguide (DLW) are shown. In both cases, a dielectric thickness of  $b - a$  is surrounded by a metallic jacket; an electron bunch is shown exiting each DLW after inducing a longitudinal electric field (shown as red and blue contours).

noting that for a single mode structure  $\kappa = |V|^2/4W$  where  $V$  and  $U$  are the voltage and stored energy of the excited mode respectively (see 3). Note that the field in Eq. 2.1 and the wake function have no dependence on the transverse coordinates. The expected change in longitudinal momentum for a particle within and behind a bunch with line-charge current distribution  $\Lambda(z)$  is obtained from the convolution integral

$$\Delta E(z) \simeq c\Delta p_z(z) = L_{dlw} \int_{-\infty}^z dz' \Lambda(z - z') w_z(z'), \quad (2.2)$$

where  $L_{dlw}$  is the length of the DLW structure and  $z$  the longitudinal coordinate within the bunch.



In the following we will give a brief introduction to the cylindrically-symmetric and slab-symmetric waveguides.

## 2.1 Cylindrically-symmetric DLW

For a dielectric-lined cylindrical waveguide, the theory was well completed by M. Rosing and W. Gai in Ref. [6]. Here we go through the important and relevant results of the derivation to calculate wakefields for arbitrary current profiles.

The derivation for these types of problems follows a boundary value approach where Maxwell's equations are solved in the geometry and matched to a source; for the cylindrical geometry, this leads to Bessel solutions. While there are an infinite number of solutions, the leading contributions arise from the monopole ( $m = 0$ ) and dipole ( $m = 1$ ) modes. For acceleration purposes, we are primarily interested in the monopole modes which are solely excited drive bunches travelling on axis. Additionally, these solutions are taken in the relativistic limit where  $v/c \rightarrow 1$  and therefore the trailing wakes are static with respect to the drive bunch.

For the monopole mode ( $m = 0$ ), the dispersion relation for an ultra-relativistic beam ( $\beta \rightarrow 1$ ) is given by

$$R'_0(sa) - \frac{sa}{2\epsilon_r} = 0 \quad (2.3)$$

where  $R_m$  and  $R'_m$  are given by

$$R_m(s) = N_m(sb)J_m(sr) - J_m(sb)N_m(sr) \quad (2.4)$$

$$R'_m(sr) = N_m(sb)J'_m(sr) - J_m(sb)N'_m(sr), \quad (2.5)$$

where  $J_m$  and  $N_m$  are  $m$ th-order Bessel functions of the first and second kinds respectively,  $s = (\frac{\omega}{c})^2 \sqrt{\epsilon_r \beta^2 - 1}$ ,  $r$  is the radius,  $a$  is the inner radius,  $\epsilon$  is the relative dielectric permittivity of the structure and  $\omega$  is the angular frequency.

Once the zeros of the dispersion relation are found ( $s_\lambda$ ) one can find the longitudinal electric field produced by a single electron

$$E_z(r, z_0) = \frac{4e}{\epsilon_r a} \sum_{\lambda} \left( \frac{R_0(sa)}{\frac{d}{ds} \left( R'_0(sa) - \frac{sa}{2\epsilon_r} R_0(sa) \right)} \right)_{s=s_\lambda} \cos \frac{\omega_\lambda z_0}{c} \quad (2.6)$$

where  $z_0$  is the longitudinal distance behind the charge. For arbitrary current profiles, the field can be calculated via a convolution between this Green's function and a current distribution.

The transverse wakefields can be calculated using the Panofsky-Wenzel theorem [7]

$$\frac{\partial \mathbf{F}_\perp}{\partial z} = e \nabla_\perp E_z, \quad (2.7)$$

giving

$$F_r = e(E_r - \beta B_\theta) = e \int \frac{\partial E_z}{\partial r} dz, \quad (2.8)$$

$$F_\theta = e(E_\theta + \beta B_r) = e \int \frac{\partial E_z}{r \partial \theta} dz. \quad (2.9)$$

The absence of dependence on  $r$  and  $\theta$  in 2.6 results in a longitudinal field with no transverse forces. However for  $m \geq 1$  (e.g. off-axis beam), wakefields do have transverse forces which can lead to significant focusing/defocusing forces. These forces can lead to beam breakup (BBU) instabilities for non-centered or transversely asymmetric beams. Ultimately such dipole-modes ( $m=1$ ) can result in transverse fields on the order of  $1/a^3$  (Ref. [8]) which

has more recently shifted interest toward slab-symmetric DLWs which are less prone to such detrimental fields as explained in Ref. [9].

## 2.2 Slab-symmetric DLWs

Slab-symmetric structures are an attractive alternative to cylindrical-symmetric DLWs for beam-driven acceleration for a number of reasons discussed ahead. We use a theoretical model from colleague Daniel Mihalcea ([10]) which is based on [9, 11] for all beam-driven calculations with slab-symmetric DLWs. The approach also develops a Green's function to compute the 3D electromagnetic fields in the waveguide; however now the rectangular axisymmetric fields take two sets of modes; the longitudinal section electric (LSE) and longitudinal section magnetic (LSM) which are based on more conventional transverse electric (TE) and transverse magnetic (TM) modes in a rectangular conducting waveguide, but include the dielectric contribution. We are particularly interested with the LSM<sub>11</sub> mode for beam-driven acceleration.

The approach uses the Hertzian vector potential method ([12]) to derive the LSM dispersion relation

$$\coth k_{x,m} a \cot k_y (b - a) = \frac{k_y}{\epsilon_r k_{x,m}}. \quad (2.10)$$

Here  $k_{x,m}$  and  $k_{y,n}$  are wavenumbers for an infinite set of modes in the open ( $\hat{x}$ ) and dielectric ( $\hat{y}$ ) planes;  $m$  and  $n$  are integers for these directions respectively, and the eigenfrequencies are related via

$$k_{x,m}^2 + k_{y,n}^2 = \frac{\omega_{m,n}^2}{c^2} (\epsilon_r - 1) \quad (2.11)$$

where  $\epsilon_r$  is the relative dielectric permittivity of the structure.

$$\begin{aligned}
E_{x,m,n} &= \begin{cases} -\frac{iE_{0;m,n}k_{x,m}}{k_z} \sin(k_{x,m}x) \cosh(k_{x,m}y) & 0 < y < a \\ -\frac{iE_{0;m,n}k_{x,m}}{k_z} \frac{\cosh(k_{x,m}a)}{\sin[k_{y,n}(b-a)]} \sin(k_{x,m}x) \sin[k_{y,n}(b-y)] & a < y < b \end{cases} \\
E_{y,m,n} &= \begin{cases} \frac{iE_{0;m,n}}{k_{x,m}k_z} (k_{x,m}^2 + k_z^2) \cos(k_{x,m}x) \sinh(k_{x,m}y) & 0 < y < a \\ \frac{iE_{0;m,n} \cosh(k_{x,m}a)}{k_{y,n}k_z \sin[k_{y,n}(b-a)]} (k_z^2 + k_{x,m}^2) \cos(k_{x,m}x) \cos[k_{y,n}(b-y)] & a < y < b \end{cases} \\
E_{z,m,n} &= \begin{cases} E_{0;m,n} \cos(k_{x,m}x) \cosh(k_{x,m}y) & 0 < y < a \\ E_{0;m,n} \frac{\cosh(k_{x,m}a)}{\sin[k_{y,n}(b-a)]} \cos(k_{x,m}x) \sin[k_{y,n}(b-y)] & a < y < b \end{cases} \\
H_{x,m,n} &= \begin{cases} -\frac{iE_{0;m,n}k_z\epsilon_r c}{k_{x,m}} \cos(k_{x,m}x) \sinh(k_{x,m}y) & 0 < y < a \\ -\frac{iE_{0;m,n}k_z\epsilon_r c}{k_{x,m}} \frac{\cosh(k_{x,m}a)}{\sin[k_{y,n}(b-a)]} \cos(k_{x,m}x) \cos[k_{y,n}(b-y)] & a < y < b \end{cases} \\
H_{y,m,n} &= 0 \\
H_{z,m,n} &= \begin{cases} E_{0;m,n}\epsilon_r c \sin(k_{x,m}x) \sinh(k_{x,m}y) & 0 < y < a \\ \frac{E_{0;m,n}k_{x,m}\epsilon_r c}{k_{y,n}} \frac{\cosh(k_{x,m}a)}{\sin[k_{y,n}(b-a)]} \sin(k_{x,m}x) \cos[k_{y,n}(b-y)] & a < y < b \end{cases} \quad (2.12)
\end{aligned}$$

where

$$E_{0;m,n}^{LSM} = \frac{1}{2\epsilon_0} \frac{\lambda_m \cosh(k_{x,m}y_0)}{\frac{\sinh(2k_{x,m}a)}{2k_{x,m}} + \frac{\epsilon_r \cosh^2(k_{x,m}a)}{\sin^2[k_{y,n}(b-a)]} \left\{ \frac{b-a}{2} \left( 1 + \frac{\epsilon_r k_{x,m}^2}{k_{y,n}^2} \right) - \frac{\sin[2k_{y,n}(b-a)]}{4k_{y,n}} \left( 1 - \frac{\epsilon_r k_{x,m}^2}{k_{y,n}^2} \right) \right\}}. \quad (2.13)$$

Finally for an arbitrary longitudinal charge density  $\rho$ , the longitudinal wakefield takes the form

$$W_z(z) = \sum_{m=0,1,\dots} \sum_{n=0,1,\dots} \int_z^\infty \rho(z') E_{z,m,n}(z - z') dz'. \quad (2.14)$$

### 2.3 Alternative slab-symmetric formulation

We also looked at two alternative approaches from Bernhard ( [13]) and Xiao ( [11]) to slab-symmetric fomulations for arbitrary phase velocities in effort to understand dispersion related discussions ahead. The papers use different techniques to obtain the fields and dispersion equations for the LSE and LSM modes. Bernhard's method uses the traditional Hertzian potential to calculate the  $E$  and  $B$  fields using the Lorentz conditions. With the exception of a small typo described below, Bernhard's method is mathematically correct. Xiao uses another technique with circuit equivalence to jump directly to the dispersion equations and works backwards to attain the electromagnetic fields. The authors also use different variables to describe the geometry, for consistency we reexpress the Xiao formulation into Bernhard's (see Fig. 2.2 for corresponding description).

In this notation the wavevectors take the form for the dielectric ( $k_{x1}$ ) and hollow ( $k_{x2}$ ) sections

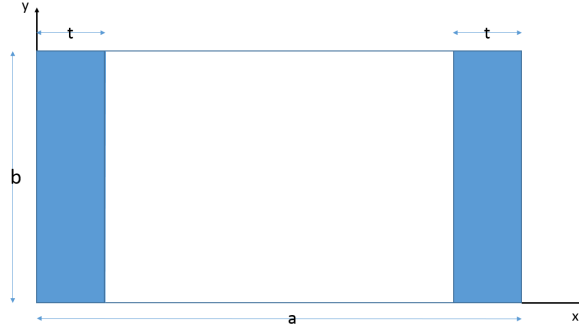


Figure 2.2: The slab-symmetric DLW in Bernhard's formulation; the full dielectric dimension width has length  $a$ , the two dielectric slabs have a thickness  $t$ , and the transverse open dimension has length  $b$ .

$$\begin{aligned} k_{x_1}^2 &= \frac{\omega^2}{c^2} \epsilon_r - k_z^2 - k_y^2 \\ k_{x_2}^2 &= \frac{\omega^2}{c^2} - k_z^2 - k_y^2. \end{aligned} \quad (2.15)$$

This leads to the LSM modes for Bernhard and Xiao respectively

$$\begin{aligned} 0 &= k_{x_1}^2 \sin^2 k_{x_1} t \sin k_{x_2} (a - 2t) - \epsilon_r^2 k_{x_2}^2 \cos^2 k_{x_1} t \sin k_{x_2} (a - 2t) \\ &\quad - 2\epsilon_r k_{x_1} k_{x_2} \sin k_{x_1} t \cos k_{x_1} t \cos k_{x_2} (a - 2t) \end{aligned} \quad (2.16)$$

$$0 = k_{x_1} \sin k_{x_1} t \sin k_{x_2} \left(\frac{a}{2} - t\right) - \epsilon_r k_{x_2} \cos k_{x_2} \left(\frac{a}{2} - t\right) \cos k_{x_1} t.$$

The dispersion equations are transcendental and generally do not have closed form solutions; fortunately modern computing power can easily solve these equations numerically. We developed a C++ code and as an example, we illustrate the dispersion for the LSM modes in a structure with parameters  $(a, b, t, \epsilon) = (1 \text{ mm}, 1 \text{ cm}, 200 \text{ } \mu\text{m}, 5.7)$  in Fig. 2.3. Here we solve for  $k_z$  as a function of  $\omega$ ; as usual the phase and group velocities can be obtained via  $\omega/k_z$  and  $\partial\omega/\partial k_z$  respectively.

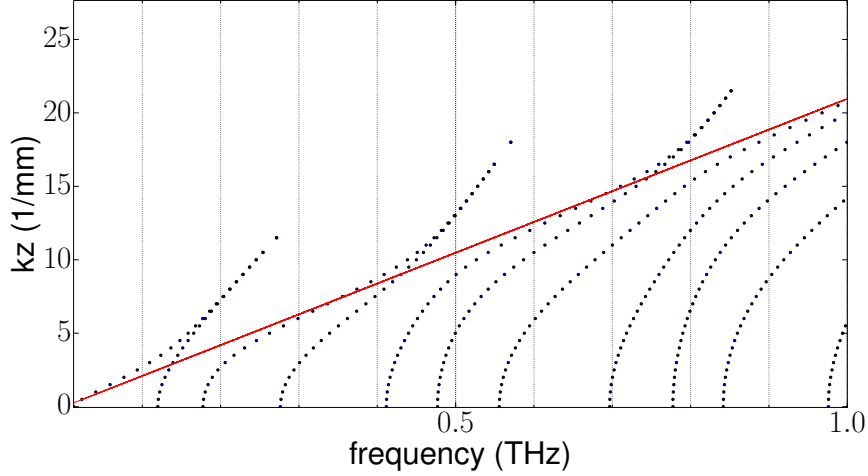


Figure 2.3: Dispersion relation for the LSM mode for the Bernhard formalism for a structure with parameters  $(a, b, t, \epsilon) = (1 \text{ mm}, 1 \text{ cm}, 200 \text{ } \mu\text{m}, 5.7)$ . The diagonal red line corresponds to the speed of light.

## 2.4 Computation and simulation

Much of the work that ensues requires computational simulation to depict the real-world physical dynamics. In the following we have used a combination of ASTRA [27], VORPAL [51], and ELEGANT [63] for different purposes; here we briefly introduce each of these codes. ASTRA is a particle tracking code which is capable of 2+1/2 D and full-3D computation which includes space-charge forces. We use this code especially for low-energy beams where space charge has a significant impact on the beam dynamics. ASTRA is capable of wakefield calculations for a longitudinal (and transverse) Green's function; this is accomplished via the convolution integral in 2.2 and the Green's function is calculated in an auxiliary file.

VORPAL is a three-dimensional electromagnetic and electrostatic PIC code. VORPAL uses a conformal finite difference-time domain (FDTD) method to solve Maxwell's equations and that includes an advanced technique known as cut-cell boundaries to allow accurate

representation of curved geometries within a rectangular grid. We use VORPAL to compare with results from other codes.

ELEGANT is a particle tracking code that does not include space charge. It is especially useful to simulate and optimize beamline configurations for particular applications (e.g. fitting a beam through a DLW). ELEGANT is based on an optics-approach where transfer-matrices are defined for each beamline element; the resulting multiplication of these matrices leads to a comprehensive transfer matrix for the entire beamline and results in a relatively fast code capable of tracking a large number of particles.

We also developed a C++ which calculates wakefields for arbitrary geometries  $(a, b, \epsilon_r)$  and currents  $(S(z))$ . The code works by solving the dispersion relation in a conventional step-by-step approach; for an arbitrary current profile input into the program, the code interpolates across the current and calculates the convolution integral via the Runge-Kutta-4 method. A subsequent routine is ran after the wake calculation to determine the maximum accelerating and decelerating fields to ultimately calculate the transformer ratio. This code was used throughout the dissertation in various parameter scans in various studies for the cylindrical-symmetric DLW.

An example of a computed Green's function for a structure with parameters  $(a, b, \epsilon_r) = (400 \mu m, b = 450 \mu m, \epsilon_r = 5.7)$  (corresponding to diamond) appears in Fig. 2.4. The Green's function converges after the inclusion of 4 modes (the  $50\text{-}\mu m$  thickness of the structure supports multiple modes with significant axial fields).



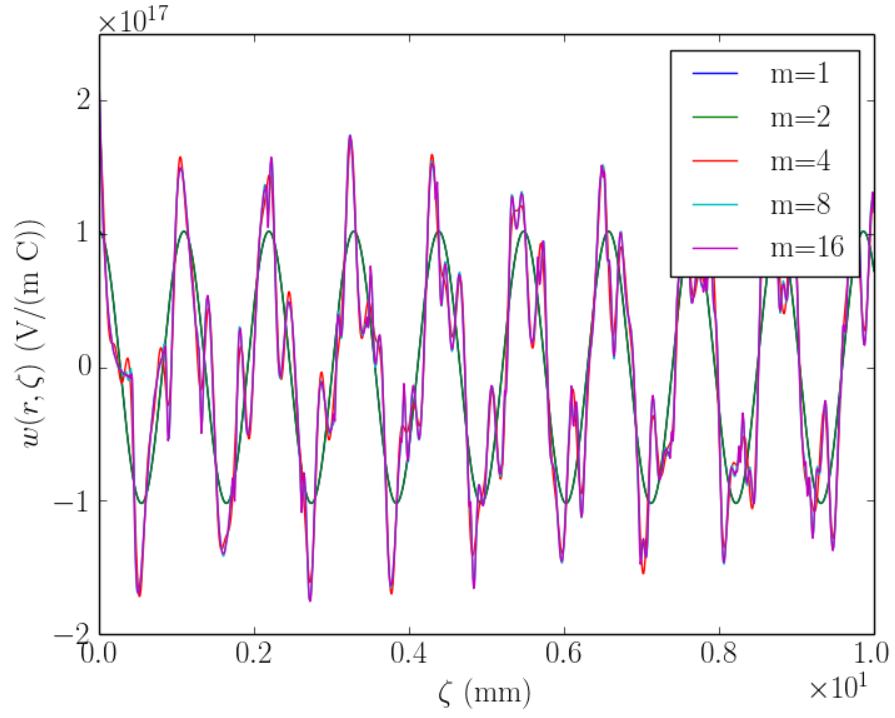


Figure 2.4: Wake function computed as  $w_z(\zeta) = \sum_{l=1}^m w_{z,l}$  for  $m = 1, 2, 4, 8$ , and  $16$  for a DLW structure with parameters  $a = 400 \mu\text{m}$ ,  $b = 450 \mu\text{m}$ , and  $\epsilon_r = 5.7$ . The fundamental-mode (blue trace) wavelength is  $\lambda_1 \simeq 1.09 \text{ mm}$ .

## CHAPTER 3

### BEAM-DRIVEN ACCELERATION

Increasing the energy of an electron beam can be useful for many applications ranging from fundamental physics to the development of coherent light-sources for biological or even nuclear science. Conventional RF-based acceleration technologies are limited to acceleration gradients of  $\sim 100$  MV/m; future TeV+ accelerators based on conventional acceleration techniques will necessarily carry large footprint and costs. An alternative is beam-driven acceleration ([4]) where a high-charge “drive” bunch passes through a high-impedance medium such as a DLW or plasma and experiences a decelerating field; and a properly delayed trailing “witness” bunch can experience a large accelerating field.

#### 3.1 Transformer ratio

A figure of merit to beam-driven acceleration which is proportional to the efficiency of the scheme is the transformer ratio, defined as

$$\mathcal{R} \equiv \left| \frac{E_+}{E_-} \right|, \tag{3.1}$$

where  $E_+$  is the maximum accelerating field and  $E_-$  is the maximum decelerating experienced by the drive bunch; assuming the drive bunch is fully decelerated, the final energy gain of the witness bunch can be approximated by  $\mathcal{E}_f = \mathcal{E}_i \mathcal{R}$  where  $\mathcal{E}_i$  is the initial beam energy.

Generally the transformer ratio is limited to values  $\mathcal{R} \leq 2$  due to the fundamental beam-loading theorem [14] which states that from energy conservation, the energy lost of a driving bunch must be equal to the work done by the induced voltage on itself. However larger values can be produced using drive bunches with tailored (asymmetric) current profiles. Take for example the standard reference in discussing the transformer ratio, the “ramped” or “triangular” distribution defined as

$$S(z) = az. \quad (3.2)$$

For a single mode structure, the Green’s function is given by  $W_z = 2k_0 \cos kz$  (where  $k_0$  is the loss factor). We impose the normalization condition:  $aL^2/2 = Q$  where  $Q$  is the charge of the bunch, and  $L$  is the bunch length, this leads to the following decelerating and accelerating fields respectively

$$\begin{aligned} E_-(z) &= \int_0^z I(x)W_z(z-x) dx = \frac{4Qk_0}{L^2k^2}(1 - \cos kz) \\ E_+(z) &= \int_0^L I(x)W_z(z-x) dx = \frac{4Qk_0}{L^2k^2}(\cos k(L-z) - \cos kz - Lk \sin k(L-z)). \end{aligned} \quad (3.3)$$

Altogether, the transformer ratio can be locally maximized to give  $\mathcal{R} = N\pi$  by choosing bunchlengths  $L = \frac{2\pi N}{k} = N\lambda$ ; and generally we see  $\mathcal{R} \approx \pi L$  and  $E_+ \approx \frac{2}{\pi^2 L^2}$ ; see Fig. 3.4. The oscillating decelerating field  $E_-$  diminishes the total energy which can be extracted from the drive beam.

Furthermore, it can be shown that both  $\mathcal{R}$  and  $E_+$  for a given charge are maximized when the decelerating field over the drive bunch is constant [15]. Additionally, bunch current profiles that minimize the accumulated energy spread within the drive bunch are desirable as they enable transport of the drive bunch over longer distances.

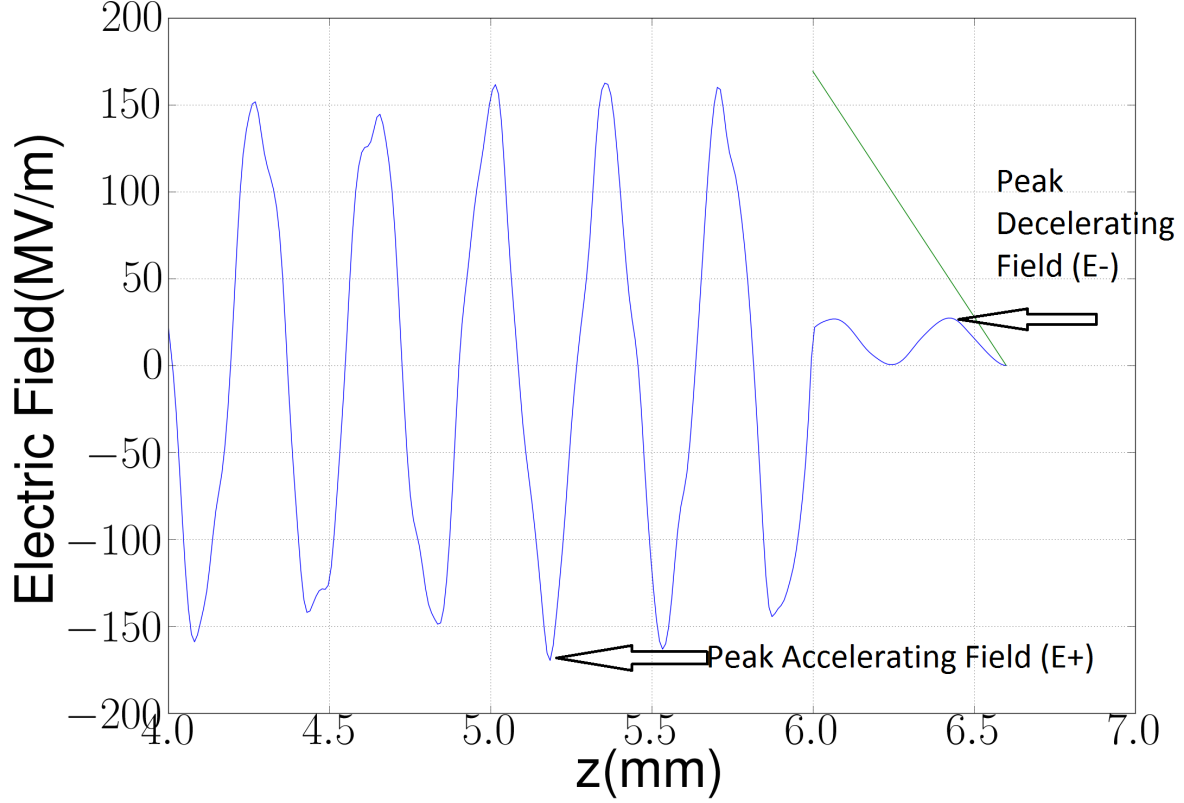


Figure 3.1: The longitudinal accelerating field is shown for the ramped bunch for a cylindrical structure with parameters  $(a, b, \epsilon) = (165 \mu m, 195 \mu m, 5.7)$ . Arrows indicate the maximum accelerating and decelerating fields ( $E_+$ ,  $E_-$  respectively) and hence the transformer ratio of  $\sim 6$  from a bunchlength of  $\sim 1.5\lambda$ .

To date, several current profiles capable of generating transformer ratios  $\mathcal{R} > 2$  have been proposed [15, 16, 17]. These include linearly ramped profiles combined with a doorstep or exponential initial distribution [18]. In our notation the “doorstep” distribution is defined as

$$S(z) = \begin{cases} a & \text{if } 0 \leq z < \xi, \\ a\left(\frac{2\pi(z-\xi)}{\lambda} + 1\right) & \text{if } \xi \leq z \leq Z, \\ 0 & \text{elsewhere.} \end{cases} \quad (3.4)$$

More recently a piecewise “double-triangle” current profile was suggested as an alternative with the advantage of being experimentally realizable [19]; in our notation this is defined as

$$S(z) = \begin{cases} akz & \text{if } 0 \leq z < \xi, \\ a(kz - 1) & \text{if } \xi \leq z \leq Z, \\ 0 & \text{elsewhere.} \end{cases} \quad (3.5)$$

We note that both of these currents only lead to constant decelerating fields when  $\xi = \lambda/4$ ; we omit the “exponential-ramp” due to the overlying difficulty of experimentally realizing the shape.

A main limitation common to all these shapes resides in their discontinuous character which make their experimental realization either challenging or relying on complicated beam-manipulation techniques [20, 21]. In addition these shapes are often foreseen to be formed in combination with an interceptive mask [22, 23] which add further challenges when combined with high-repetition-rate linacs [8] (where, e.g., high-power beams can melt and destroy masks, or require cooling infrastructure).

### 3.2 Smooth Shapes

We consider a smooth function  $S(z)$  to be non vanishing on two intervals  $[0, \xi]$  (the bunch-head) and  $[\xi, Z]$  (bunch-tail) and zero elsewhere. We also constrain our search to functions where  $S(z)$  and  $S'(z) \equiv dS/dz$  are continuous at  $z = \xi$ . Introducing the function  $f(z)$  (to be specified later), we write the charge distribution as

$$S(z) = \begin{cases} f(z) & \text{if } 0 \leq z < \xi, \\ f'(\xi)z - f'(\xi)\xi + f(\xi) & \text{if } \xi \leq z \leq Z, \\ 0 & \text{elsewhere.} \end{cases} \quad (3.6)$$

### 3.2.1 Linear ramp with sinusoidal head

Based on our previous work [24] we first consider the following function

$$f(z) = az + b \sin(qkz), \quad (3.7)$$

where  $a$  and  $b$  are positive constants,  $k$  is again the wavenumber associated to a structure, and  $q > 0$  is an integer. Consequently, using Eq. 3.6, the axial bunch profile is written as

$$S(z) = \begin{cases} az + b \sin(qkz) & \text{if } 0 \leq z < \xi, \\ ax + bqk(x - \xi) \cos(q\xi k) \\ + b \sin(q\xi k) & \text{if } \xi \leq z \leq Z, \\ 0 & \text{elsewhere.} \end{cases} \quad (3.8)$$

In this section we report only on solutions pertaining to  $\xi = \lambda/2$ . Additional, albeit more complicated, solutions also exist for larger  $\xi$ ; however, these solutions lead to additional oscillations which ultimately lowers the transformer ratio.

From Eq. 3.3, the decelerating field then takes the form

$$E_-(z) = \kappa \begin{cases} \frac{\lambda}{\pi^2} \left( a\lambda \sin^2 \left( \frac{\pi z}{\lambda} \right) + \frac{\pi b q \left( \cos \left( \frac{2\pi z}{\lambda} \right) - \cos \left( \frac{2\pi q z}{\lambda} \right) \right)}{q^2 - 1} \right) & z < \lambda/2 \\ \frac{\lambda \left( (q^2 - 1)(a\lambda + 2\pi b(-1)^q q) + \cos \left( \frac{2\pi z}{\lambda} \right) (2\pi b q ((-1)^q q^2 + 1) - a(q^2 - 1)\lambda) \right)}{2\pi^2(q^2 - 1)} & z \geq \lambda/2 \end{cases} \quad (3.9)$$

The oscillatory part in the tail ( $\lambda/2 \leq z$ ) can be eliminated under the condition

$$b = \frac{a(q^2 - 1)\lambda}{2\pi q((-1)^q q^2 + 1)}, \quad (3.10)$$

which leads to the following decelerating and accelerating fields respectively

$$E_-(z) = \kappa \begin{cases} \frac{a\lambda^2(2(-1)^q q^2 \sin^2 \left( \frac{\pi z}{\lambda} \right) - \cos \left( \frac{2\pi q z}{\lambda} \right) + 1)}{2\pi^2((-1)^q q^2 + 1)} & z < \lambda/2 \\ \frac{a((-1)^q(2q^2 - 1) + 1)\lambda^2}{2\pi^2((-1)^q q^2 + 1)} & z \geq \lambda/2 \end{cases} \quad (3.11)$$

$$\begin{aligned} E_+(z) &= \int_0^{N\lambda} s(z') \omega(z - z') dz' \\ &= \kappa \frac{a\lambda^2 \left( \pi((-1)^q((4N - 1)q^2 - 2N + 1) + 2N) \sin \left( 2\pi \left( N - \frac{z}{\lambda} \right) \right) + ((-1)^q(2q^2 - 1) + 1) \cos \left( 2\pi \left( N - \frac{z}{\lambda} \right) \right) \right)}{2\pi^2((-1)^q q^2 + 1)}. \end{aligned} \quad (3.12)$$

Finally, the transformer ratio can be calculated by taking the ratio of the maximum accelerating field over the maximum decelerating field which yields

$$\mathcal{R} = \frac{\sqrt{\pi^2((-1)^q((4N - 1)q^2 - 2N + 1) + 2N)^2 + ((-1)^q(2q^2 - 1) + 1)^2}}{(-1)^q(2q^2 - 1) + 1}. \quad (3.13)$$

Two sets of solutions occur for even and odd  $q$  which can be interpreted as a phase shift in the oscillatory part. Additionally, larger multiples of even and odd  $q$  lead to more

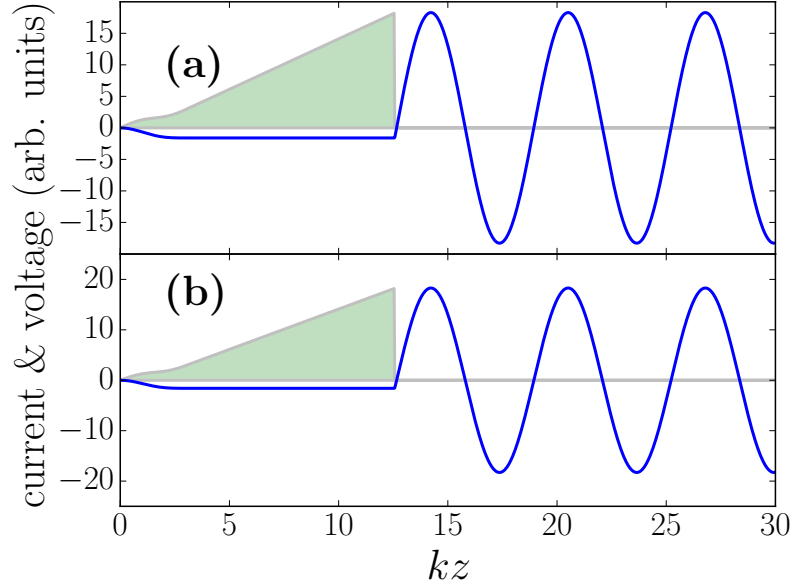


Figure 3.2: Example of current profiles described by Eq. 3.8 (shaded line) with the corresponding induced voltages. The parameters are  $n = 0$ ,  $N = 5$ , and plots (a) and (b) respectively correspond to the cases  $q = 2$  and  $q = 3$ . The head of the bunch is at  $kz = 0$ .

oscillations in the head which ultimately reduce the transformer ratio. In Fig. 3.2 we illustrate the simplest even (a) and odd (b) solutions corresponding to  $q = 2$  and  $q = 3$  respectively.

### 3.2.2 Linear ramp with parabolic head

We now consider an even simpler quadratic shape taking the form

$$f(z) = az^2, \quad (3.14)$$



which leads to the current profile

$$S(z) = \begin{cases} az^2 & \text{if } 0 \leq z < \xi, \\ 2a\xi z - a\xi^2 & \text{if } \xi \leq z \leq Z, \\ 0 & \text{elsewhere.} \end{cases} \quad (3.15)$$

The resulting decelerating field within the bunch is

$$E_-(z) = 2\kappa \begin{cases} -2a \frac{\sin(kz) - kz}{k^3} & \text{if } 0 \leq z < \xi, \\ 2a \frac{\sin[k(z-\xi)] - \sin(kz) + 2k\xi}{k^3} & \text{if } \xi \leq z \leq Z, \\ 0 & \text{elsewhere.} \end{cases}$$

Again, the decelerating field can be made constant for  $z \in [\xi, Z]$  when  $\xi = \nu\lambda$  with  $\nu \in \mathbb{N}$ .

In such a case the previous equations simplifies to

$$E_-(z) = 2\kappa \begin{cases} -2a \frac{\sin(kz) - kz}{k^3} & \text{if } 0 \leq z < \nu\lambda, \\ \frac{4\pi a\nu}{k^3} & \text{if } \nu\lambda \leq z \leq Z, \\ 0 & \text{elsewhere.} \end{cases}$$

$$E_+(z) = -\frac{8\pi\nu a\kappa}{k^3} [\pi(2N - \nu) \sin(kz) - \cos(kz)], \quad (3.16)$$

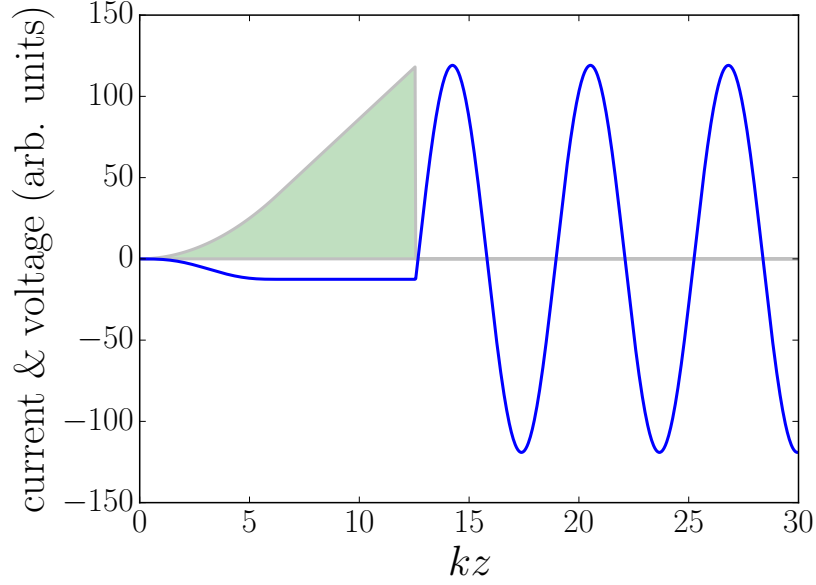


Figure 3.3: Example of ideal “quadratic” current profiles given by Eq. 3.15 (shaded line) with corresponding induced voltage. The parameters are  $\nu = 1$ , and  $N = 5$ . The head of the bunch is at  $kz = 0$ .

yielding the transformer ratio

$$\mathcal{R} = [1 + \pi^2(2N - \nu)^2]^{1/2}. \quad (3.17)$$

In Fig. 3.3 we illustrate an example of the quadratic shape (green trace) as well as its corresponding longitudinal electric field (blue trace) for  $\nu = 1$  and  $N = 5$ .

### 3.2.3 Comparison with other shapes

We now turn to compare the smooth longitudinal shapes from the previous Section with the doorstep [18] and double-triangle [19] which also provide constant decelerating fields over the bunch-tail. For a fair comparison, we stress the importance of comparing the various

current profiles with equal charge. Consequently, we normalize each of the current profile to the same bunch charge

$$Q = \int_0^{N\lambda} dz S(z, a); \quad (3.18)$$

where  $a$  is the scaling parameter associated with each bunch shape, and  $N\lambda$  is the total bunch length which is assumed to be larger than the given shape's bunch-head length ( $N\lambda > \xi$ ). For each distribution, the charge normalization generates a relationship between  $a$  and  $N\lambda$  which enables us to reexpress  $\mathcal{R}$  in terms of  $Q$  and  $a$ . In Tab. 3.1 we tabulate the analytical results for  $\mathcal{R}(N)$  (the conventional notation [18, 19]) and  $\mathcal{R}(Q, a)$ , and also list the maximum decelerating field  $E_-^m$  for each distribution. Additionally in Fig. 3.4 we illustrate these results in a log-log plot where, for each distribution, the scaling parameter ( $a$ ) was varied for a fixed charge and wavelength. To complete our comparison we also added the linear-ramp and Gaussian distributions.

The results indicate that all of the distributions with constant decelerating fields over the bunch-tail ‘live’ on the same curve; additionally, by varying the scaling parameter  $a$  for a distribution, you can shift a distribution to have a larger (resp. smaller)  $\mathcal{R}$  (resp.  $E_+$ ) and vice-versa. Ultimately, this suggests that the distribution which is simplest to make is as useful as any other and it can be scaled accordingly ( $\mathcal{R}, E_+$ ) for a specific application. These results confirm our previous studies regarding the numerical investigation of the trade-off between  $\mathcal{R}$  and  $E_+$  [25].

### 3.3 Photoemission of optimal shapes via laser-shaping

In this section we investigate the realization of the quadratic distribution discussed in Section 3.2 by longitudinally tailoring a laser pulse impinging on a photocathode in a photoinjector. The resulting electron distribution is then accelerated in an RF-gun and expands

Table 3.1: Table comparing several different proposed drive bunch distributions as a function of bunch length and charge. Additionally, the maximum decelerating field ( $E_-^m$ ) is shown for each distribution. Here we consider  $\kappa = 1$ .

distribution	$\mathcal{R}(N)$	$\mathcal{R}(Q)$	$E_-^m$
doorstep [18]	$\sqrt{1 + (1 - \pi/2 + 2\pi N)^2}$	$\sqrt{2 + \pi(\frac{4Q}{a\lambda} - 1)}$	$\frac{a\lambda}{\pi}$
double triangle [19]	$\sqrt{1 + (2\pi N - 1)^2}$	$\sqrt{2 + \pi(\frac{4Q}{a\lambda} - 1)}$	$\frac{a\lambda}{\pi}$
sin ( $q = 2$ )	$\frac{1}{8}\sqrt{\pi^2(3 - 16N)^2 + 64}$	$\frac{1}{8}\sqrt{64 - 15\pi^2 + \frac{48\pi Q}{a\lambda}}$	$\frac{16a\lambda}{3\pi}$
sin ( $q = 3$ )	$\frac{1}{2}\sqrt{\pi^2(1 - 4N)^2 + 4}$	$\frac{1}{6}\sqrt{44 - 9\pi^2 + \frac{24\pi Q}{a\lambda}}$	$\frac{6a\lambda}{\pi}$
quadratic	$\sqrt{1 + \pi^2(2N - 1)^2}$	$\sqrt{1 + \pi^2(\frac{4Q}{a\lambda^3} - \frac{1}{3})}$	$\frac{a\lambda^3}{\pi^2}$

via space charge forces. If the charge density of the emanating electron bunch is sufficiently low, the resulting distribution will be relativistically preserved through a drift; however for larger charge densities, the original longitudinal distribution will morph according to the integrated space charge forces inside the bunch. The setup we consider throughout this section is depicted in Fig. 5.3 and consists of a typical  $1 + \frac{1}{2}$ -cell BNL/SLAC/UCLA S-band RF-gun operating at 2.856 GHz surrounded by a solenoidal lens [26]. The large ( $\sim 140$  MV/m) acceleration gradients in the gun help preserve larger charge densities compared with e.g. L-band guns. The simulations are carried with ASTRA [27], a particle-in-cell beam-dynamics program that includes a quasi-static cylindrically-symmetric space charge algorithm. The simulation also includes the image-charge effect which arises during the photoemission process, in our simulations the electron bunch is represented by 200,000 macro-particles.

### 3.3.1 Case of an ideal laser-shaping technique

The relatively simple form and smoothness of the quadratic-ramp proposed above invites the possibility of generating it via laser-shaping in a photoinjector where the space-charge forces naturally blow-out a given distribution smoothly (e.g. a discontinuous shape will

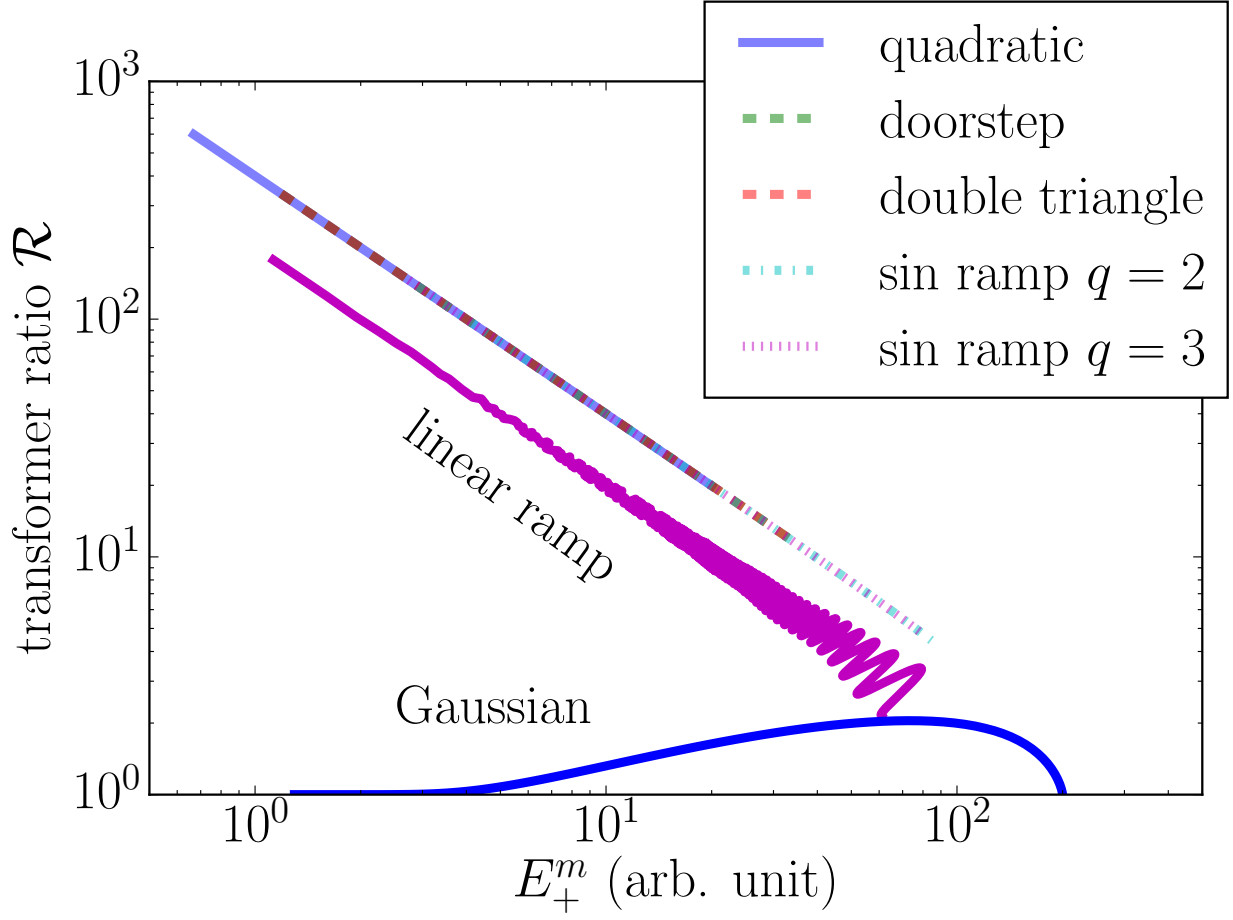


Figure 3.4: Tradeoff curves between  $\mathcal{R}$  and  $E_+^m$  for the current profiles listed in Tab. 3.1. The “quadratic” and “sin ramps” respectively correspond to the distributions proposed in Sections 3.2.2 and 3.2.1. The Gaussian and ramp distributions are displayed for comparison. This was generated by fixing the charge  $Q$  and varying the scaling parameter  $a$ .

morph into smooth one). In this perspective there exists two possibilities first, generate the exact quadratic-ramp distribution with small enough longitudinal charge density to preserve the shape is completely preserved under acceleration in the photoinjector, or second, generate a distribution which will blow-out into the quadratic ramp while being accelerated; in principle the second alternative could generate longitudinally shorter bunches with higher charge densities which are more attractive to generate larger accelerating fields. For a given distribution, there is no general solution to the evolution of a charge distribution. However,

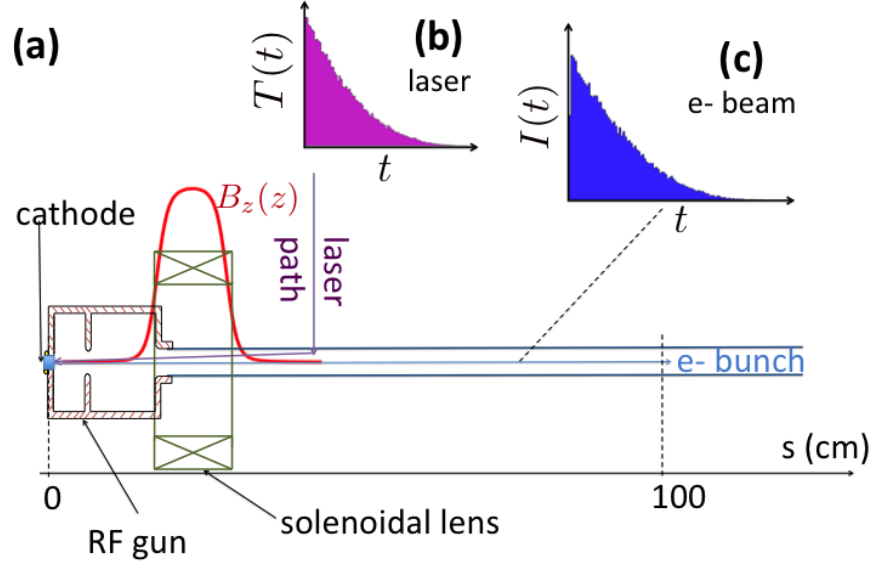


Figure 3.5: Configuration used for the pulse-shaping simulations using a S-band RF gun (a). A temporally shaped laser pulse (b) is optimized to result in a photo-emitted electron-beam with current profile (c) having features similar to the distribution discussed in Sec. 3.2.2. In insets (a) and (b) the tail of the bunch is at  $t = 0$ .

there are some elementary examples, such as the inverted parabola, which can be understood nearly completely due to the linear nature of the electric fields and forces within the bunch. The asymmetry of the ramped bunch destroys the possibility of preserving its shape with linear space charge fields.

The calculation of the longitudinal electric field in the rest frame of the distribution is usually calculated via [?]  $E(x) = -\frac{g}{4\pi\epsilon_0} \frac{\partial\rho(x)}{\partial x}$ , where  $g$  is a geometry factor and  $\epsilon_0$  the vacuum electric permittivity; however, this equation is only valid for closed symmetric bunches and does not give any valuable insight into the longitudinal electric field in the distribution above. Therefore to investigate such space charge effects, we develop a very simple 1-D model from elementary principles. Working in the bunch reference frame and assuming a "cold" beam with no energy spread, we consider the unit less 1-D Green's function for electrostatics

$$G(x, x') = \frac{1}{2}|x - x'|, \quad (3.19)$$

and compute the scalar potential via the convolution

$$\Phi(x) = \int_0^L \frac{1}{2} |x - x'| \rho(x') dx'. \quad (3.20)$$

This method recovers very similar fields for the familiar inverted parabola [?] in dimensionless units  $I(x) = x(1 - x)$ . in particular the corresponding potential is found to be

$$\Phi(x) = \frac{1}{24} (1 - 2(x - 2x^3 + x^4)) \quad (3.21)$$

giving rise to the electric field  $E(x) = \frac{1}{12}(-1 + 6x^2 - 4x^3)$  and force dependence  $F(x) = \frac{x}{12}(1 - 6x^2 + 4x^3)(x - 1)$  as illustrated in Fig. 3.6.

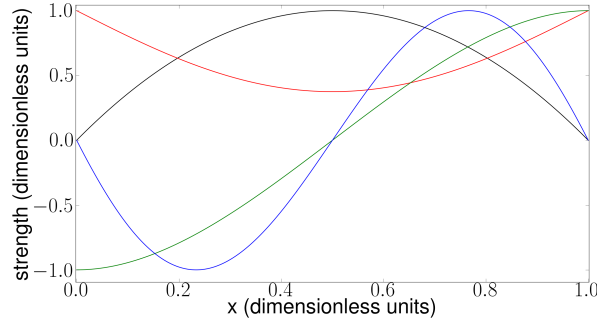


Figure 3.6: Inverted parabola distribution (black trace), and corresponding electrostatic potential (red trace), electric field (blue trace) and resulting force (blue trace) as a function of the longitudinal coordinate.

As a guess we explore the power function

$$\rho(x) = \begin{cases} x^n, & \text{for } 0 < x < 1 \\ 0, & \text{elsewhere,} \end{cases} \quad (3.22)$$

This respectively leads to the electrostatic potential, electric field and force field

$$\Phi(z) = \frac{1 + n - 2z - nz + 2z^{2+n}}{4 + 6n + 2n^2}, \quad (3.23)$$

$$E(z) = \frac{2z^{1+n} - 1}{2(1+n)}, \text{ and} \quad (3.24)$$

$$F(z) = z^n \frac{2z^{1+n} - 1}{2(1+n)}. \quad (3.25)$$

In Figure 3.7 we explore the electrostatic potential, field and force associated to power-law distributions with  $n = 1, 2$ , and  $5$ . In particular, we notice for values of  $n > 1$  (e.g.  $n=2,5$ ) the fields scale and maintain their shape across the distribution; moreover, the asymmetry of the fields will push the bunch apart about the zero-force point. In the  $n=2$  case for example, the maximum force in  $-\hat{x}$  occurs near  $0.6$ ; during expansion, this portion of the bunch will wash-out toward the left which will help make a quasi-linear shape. However the nonlinearity of the fields makes an accurate prediction quite complicated and we rely on simulations in the following section.

We now formalize the description above for a laser intensity distribution of the form  $I(r, t) = T(t)R(r)$ , where  $T(t)$  is now the longitudinal temporal profile rewritten as

$$T(t) = T_0 t^\alpha H(\tau - t), \quad (3.26)$$

and  $R(r)$  the transverse laser envelope assumed to be Gaussian;  $T_0$  is a normalization constant,  $\alpha > 0$  is the polynomial power,  $\tau$  is the ending time of the pulse, and  $H(t)$  is the Heaviside function.

Additionally, the transverse spot size of the laser pulse on the photocathode also controls the longitudinal electric fields but also influences the transverse “thermal” emittances. It is also possible to reduce the electric fields and the associated blowout rate by using longer laser pulses; in this scenario, the resulting electron bunch will evolve at a slower rate but



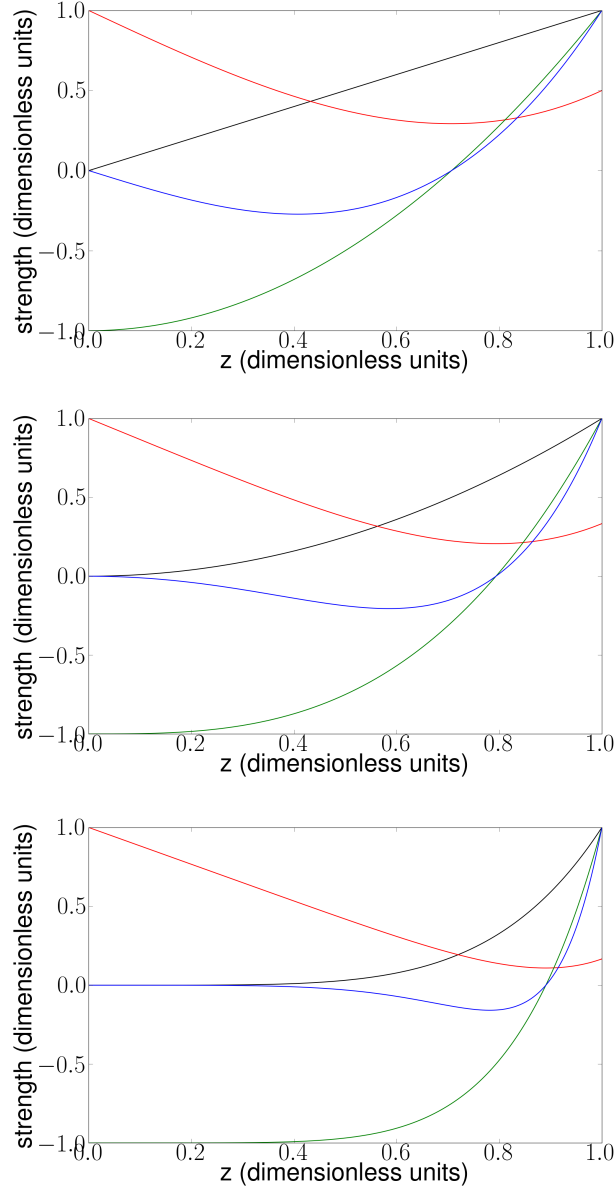


Figure 3.7: Charge distribution (black trace), and corresponding electrostatic potential (red trace), electric field (blue trace) and resulting force field (blue trace) for  $n = 1$  (top),  $n = 2$  (middle), and  $n = 5$  (bottom).

the resulting bunch distribution will have a smaller peak current compared to when starting with smaller values of  $\tau$ . A smaller current will impact the performances of the wakefield accelerator (or require the implementation of a longitudinal compression scheme). Finally,

it would also be possible to use a longer, e.g.  $2 + \frac{1}{2}$ -cell, RF gun or another acceleration cavity in close proximity to the gun to preserve larger charge densities which could effectively alleviate the need for a bunch compressor to drive large accelerating fields in the subsequent wakefield accelerator.

Figure 3.8 shows simulated longitudinal phase space snapshots and corresponding currents at different axial locations downstream of the gun for a 1-nC bunch. For this simulation a 1-mm rms laser spot size on the photocathode was used. The initial laser distribution was described by Eq. 3.26 with  $\alpha = 2$  and  $\tau = 15$  ps. A fit of the current distribution at  $s = 50$  cm from the photocathode is shown in Fig 3.8 and indicates that the final electron bunch distribution is indeed accurately described by Eq. 3.15.

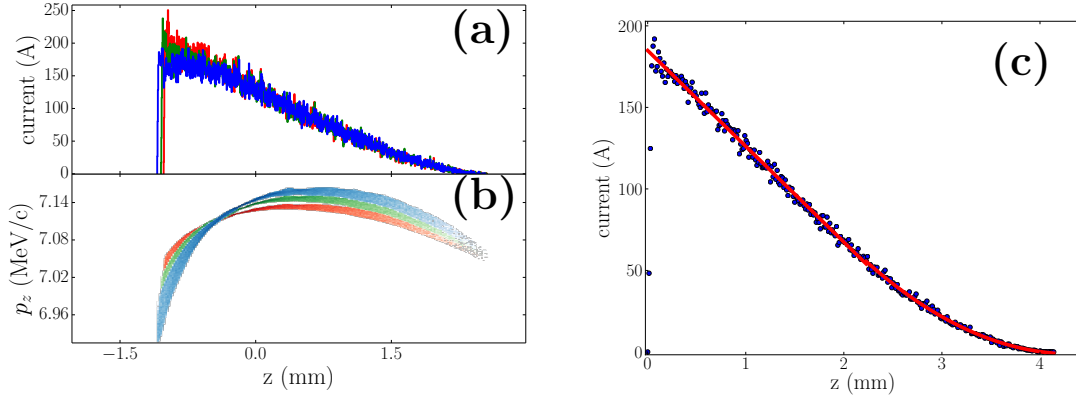


Figure 3.8: Evolution of the electron-bunch current (a) and longitudinal phase space (b) along the beamline at 20 (red), 60 (green), and 100 cm (blue) from the photocathode surface and (c) comparison of the current profile numerically simulated at  $s = 50$  cm (red trace) with a fit to equation Eq. 3.15 (blue lines). The head of the bunch is at large values of  $z$ .

### 3.3.2 Limitation of a practical laser shaping technique

As a first step toward a realistic model for the achievable shaped we consider the photoemission process to be resulting from frequency tripling of a  $\lambda_0 = 800$ -nm amplifier infrared

(IR) pulse impinging a fast-response time cathode (with typical work functions corresponding to ultraviolet photon energy  $\sim \lambda_0/3$ ). Such a setup is commonly used in RF photoinjectors such as the one discussed in the previous sections. We further assume that the frequency up-conversion process does not affect the original laser's temporal shape (e.g. the UV-pulse temporal shape is identical to the IR-pulse temporal shape). Under such an assumption, the formation of the ideal temporal shape discussed in the previous Subsection is limited by the finite laser bandwidth and frequency response of the shaping process.

We consider an incoming amplified IR pulse with intensity  $I_{in}(r, t) = I_0(r)\text{sech}^2(t/\tau)$  downstream of the last-stage amplification, where  $\tau$  is the laser pulse duration. We model the IR pulse laser-shaping process via the convolution  $I_{out}(r, t) = \int_{-\infty}^{+\infty} I_{in}(r, t - t')R(t')dt'$  where  $I_{out}(t)$  and  $R(t)$  represent the shaped-pulse intensity and response function of the shaping method respectively.

Given the desired output shape and incoming laser pulse profile, the response function of the shaping process has to be set to satisfy [30]

$$\tilde{R}(\omega) = \frac{\tilde{I}_{out}(\omega)}{\tilde{I}_{in}(\omega)}, \quad (3.27)$$

where the upper tilde represents the Fourier transformation  $\tilde{f}(\omega) = \int_{-\infty}^{+\infty} f(t)e^{i\omega t}$ . In practice  $I_{in}(\omega)$  is defined over a finite range of frequency  $\omega = \omega_0 \pm \frac{\delta\omega}{2}$  where  $\omega_0 \equiv \frac{2\pi c}{\lambda_0}$  is the central laser frequency and  $\delta\omega \equiv \frac{\omega_0}{\lambda_0}\delta\lambda$  is the laser pulse bandwidth ( $\delta\lambda$  is the wavelength span of the pulse spectrum).

The typical shape considered in the previous section after laser shaping is shown in Fig. 3.9; the limited bandwidth has very little effect except for the well-known ringing effect at the sharp discontinuities [31]; see Fig. 3.9 (b) and (c).

Another potential limitation to our shaping scheme arises with a high-efficiency (semicon-

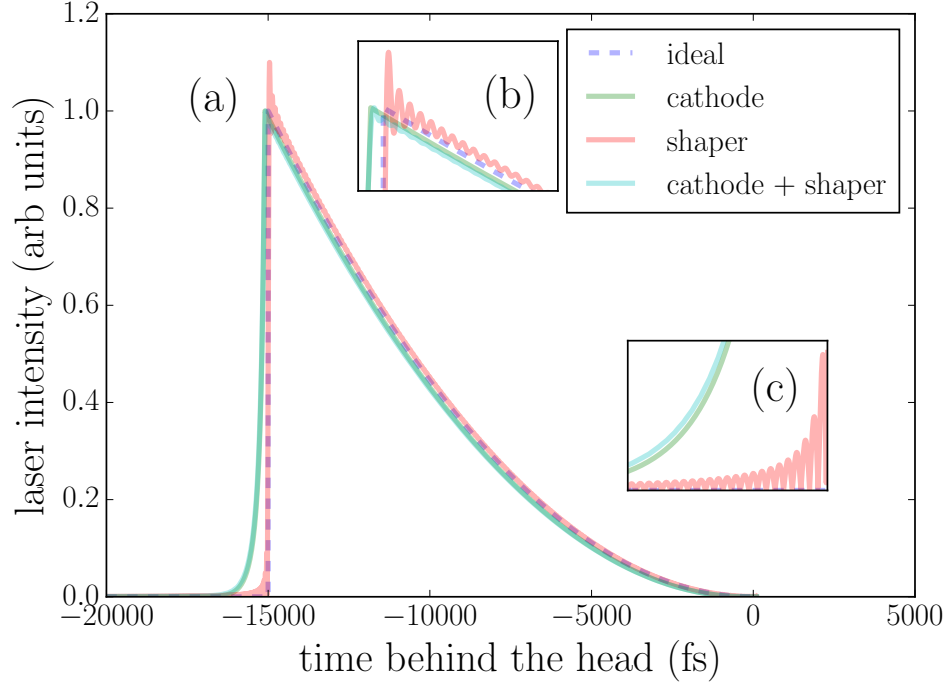


Figure 3.9: Comparison of nominal (“ideal”) shape with the shapes achieved when taking into account the photoemission response time (“cathode”), the laser-pulse-shaping finite bandwidth (“shaping”) and both effects (“cathode + shaper”). The ideal laser temporal profile is described by Eq. 3.26 with  $\alpha = 2$  and  $\tau = 15$  ps. Insets (b) and (c) are zooms of the areas  $t \in [-15200, -13600]$  fs (peak location) and  $t \in [-16000, -15020]$  fs (left edge of the profile) respectively. The head of the laser pulse is at  $t = 0$ .

ductor) photocathode. We consider as an example the case of  $\text{Cs}_2\text{Te}$  photocathodes because of their wide use in high-current photoinjectors. The response-time limitation is investigated using the parameterized impulsional time response of  $\text{Cs}_2\text{Te}$  described in Ref. [32] based on numerical simulations presented in Ref. [33]. The impulsional response is convolved with the distribution used in the previous section and the results are gathered in Fig. 3.9. Again this effect appears to be marginal. For the sake of completeness, the various profiles shown in Fig. 3.9 are tracked with ASTRA and the final current distributions at  $s = 50$  cm are found to be indiscernibly close to the ideal shape considered in the previous Section; see Fig. 3.10. Such a result gives further confidence in the proposed shaping approach.

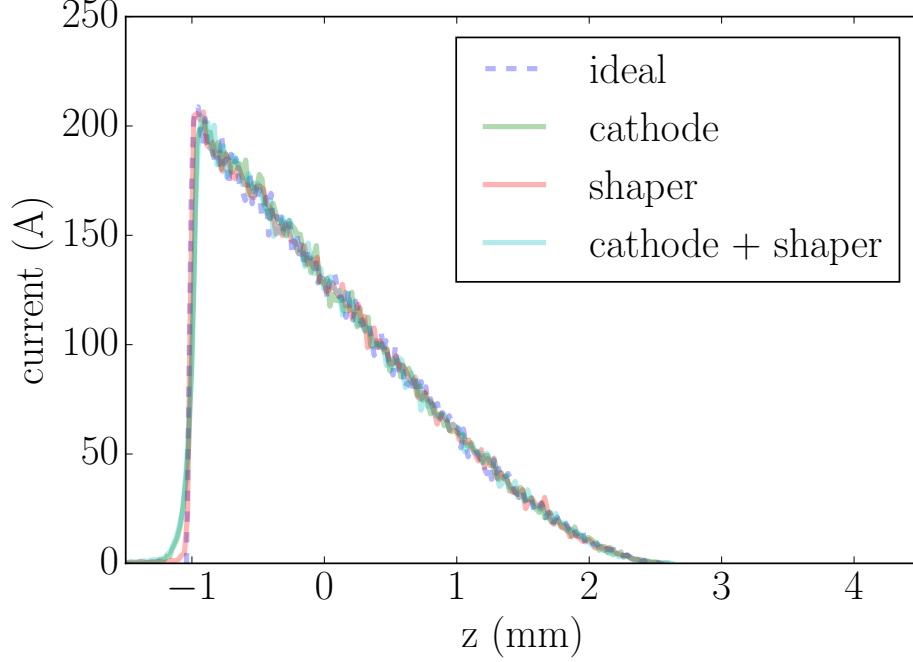


Figure 3.10: Comparison of the final electron-bunch current at  $s = 50$  cm from the cathode surface for the four cases considered in Fig. 3.9. The “cathode” and “shaper” respectively correspond to the inclusion of the cathode response time and shaper bandwidth limitation in the initial particle distribution at  $s = 0$  while the ideal case is given by Eq. 3.26 with  $\alpha = 2$  and  $\tau = 15$  ps. The head of the bunch corresponds to  $z > 0$ .

### 3.4 Formation of high-energy tailored bunches for a DWFA LINAC

We finally investigate the combination of the tailored current-profile generation scheme with subsequent acceleration in a linac located downstream of the RF gun. Such a configuration could be useful to form tailored relativistic electron bunches for direct injection in wakefield-acceleration structures. For this example, we consider a high-repetition drive bunch with parameters consistent with a recently proposed beam-driven accelerator for a short-wavelength free-electron laser (FEL) [8]. We adopt a different approach than Ref [8]

and instead choose a 1.3-GHz superconducting RF (SCRF) linac (L0 and L1) composed of TESLA cavities [34] coupled to a quarter-wave 200-MHz SCRF gun [35, 36] originally designed for the WiFEL project [37]; see diagram in Fig. 3.11. The accelerator also includes a 3.9-GHz accelerating cavity (L39) section to remove nonlinearities in the longitudinal phase space [38, 39]. For this study we explored the use of polynomial laser profile described by Eq. 3.26 and let  $\alpha$  and  $\tau$  as free parameters.

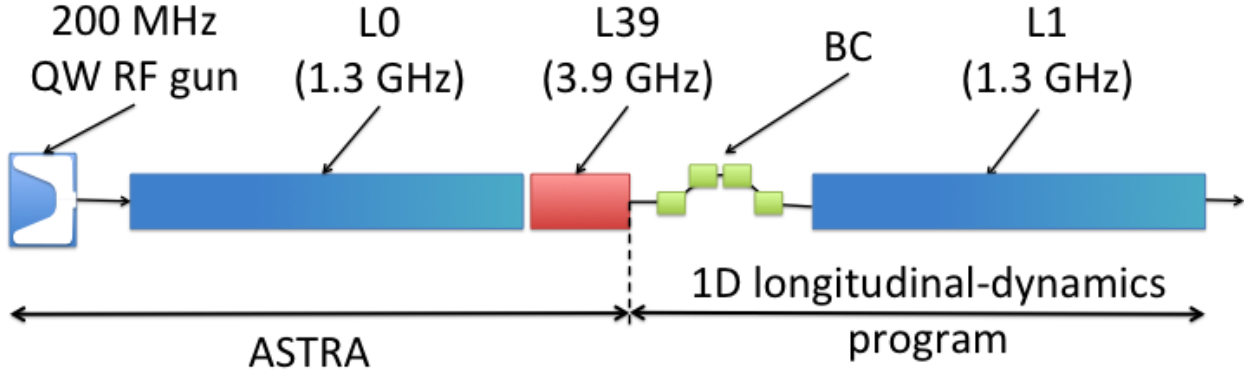


Figure 3.11: Block diagram of the accelerator configuration explored for the formation of high-energy ramped bunches. The legend is as follows: “QW” stands for quarter-wave, “L0” and “L1” are standard 1.3-GHz cryomodule equipped with 8 TESLA-type SCRF cavities, “L39” is a cryomodule consisting of four 3.9-GHz cavities, and “BC” is a magnetic bunch compressor.

The laser-profile parameters and accelerator settings were optimized using a genetic optimizer [40] to result in a final distribution with current profile consistent to achieve a high transformer ratio. The optimized accelerator settings are summarized in Tab. 3.2. In our optimization, we chose the wakefield structure to be a dielectric-lined waveguide with parameters tabulated in Tab. 3.3 and we introduce a longitudinal scaling factor  $\eta$  as free parameter such that the axial coordinate is scaled following  $z \rightarrow z' = \eta z$ . The optimization converged to a value  $\eta = 0.16$ . The obtained wakefield and scaled shape are shown in Fig. 3.12 (a).

Table 3.2: Optimized settings for the accelerator parameters needed to produce and accelerate a ramp bunch to  $\sim 200$  MeV. The parameter  $\alpha$  and  $\tau$  are defined in Eq. 3.26.

parameter	value	units
laser rms spot size $\sigma_r$	2.5	mm
laser ramp $\alpha$ parameter	19.86	—
laser ramp duration $\tau$	96.8	ps
bunch charge $Q$	5	nC
peak E-field on cathode	40	MV/m
laser injection phase	71.0	deg (200 MHz)
gun output beam momentum	5.15	MeV/c
acc. voltage L0	165	MV/m
off-crest phase L0	-12.35	deg (1.3 GHz)
acc. voltage L39	24.1	MV
off-crest phase L39	-192.35	deg (3.9 GHz)
beam momentum after L39	$\sim 143$	MeV/c
final beam momentum after L1	$\sim 350$	MeV/c

For the wakefield calculations we followed the formalism detailed in Ref. [6] and use the first four modes in the wakepotential used for the beam dynamics simulations.

Given the devised configuration, a one-dimensional model of the longitudinal beam dynamics was employed to assess the viability of the required compression and especially explore the possible impact of nonlinearities in the longitudinal phase space on the achieved current profile. We considered the current could be longitudinally compressed using a conventional magnetic bunch compressor (BC) with longitudinal linear and second order dispersions  $R_{56}$  and  $T_{566} \equiv -\frac{3}{2}R_{56}$  [41]. In our simulations the longitudinal dispersion was taken to  $R_{56} = -20$  cm following similar designs [42]. The phase of L0 and phase and amplitude of L39 were empirically optimized and the resulting longitudinal phase space  $(z_0, \delta_0)$  was tracked through the BC via the transformation  $z_0 \rightarrow z = z_0 + R_{56}\delta_0 + T_{566}\delta_0^2$ . An optimum set of phases and amplitudes was found and listed in Tab. 3.2 and the sequence of the longitudinal phase spaces along the injector appear in Fig. 3.13. The final wakefield excited in

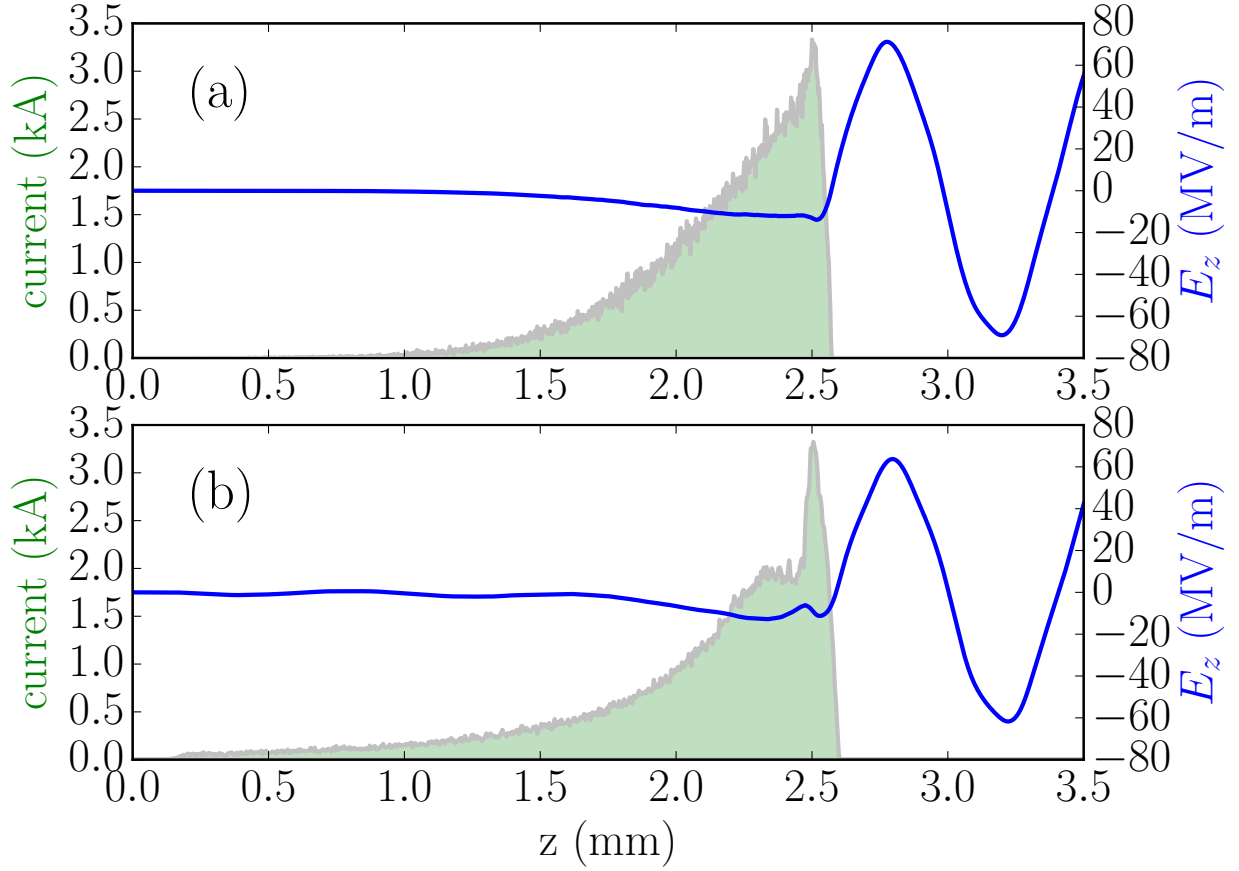


Figure 3.12: Final current distribution (green shaded area) and associated wakefield (blue traces) for the “ideal” (a) and “realistic” (b) cases of compression discussed in the text. The head of the bunch corresponds to  $z = 0$

the structure with parameters listed in Table 3.3 is displayed in Fig. 3.12 (b) – the achieved field and transformer ratio values are summarized in Table 3.3. We remark that the inclusion of a refined model of longitudinal dynamics leads to the apparition of features [e.g. a small current spike in the bunch tail; see Fig. 3.12 (b) or 3.13 (d)] that were absent in the optimization process implementing a simple scaling of the longitudinal coordinates; see Fig. 3.12 (a). The origin of the small current spike can be traced back to the nonlinear correlation imposed by space charge in the early stages of the bunch-transport process (i.e. in the drift space upstream of L0); see Fig. 3.13 (a). Nevertheless the achieved peak field and transformer



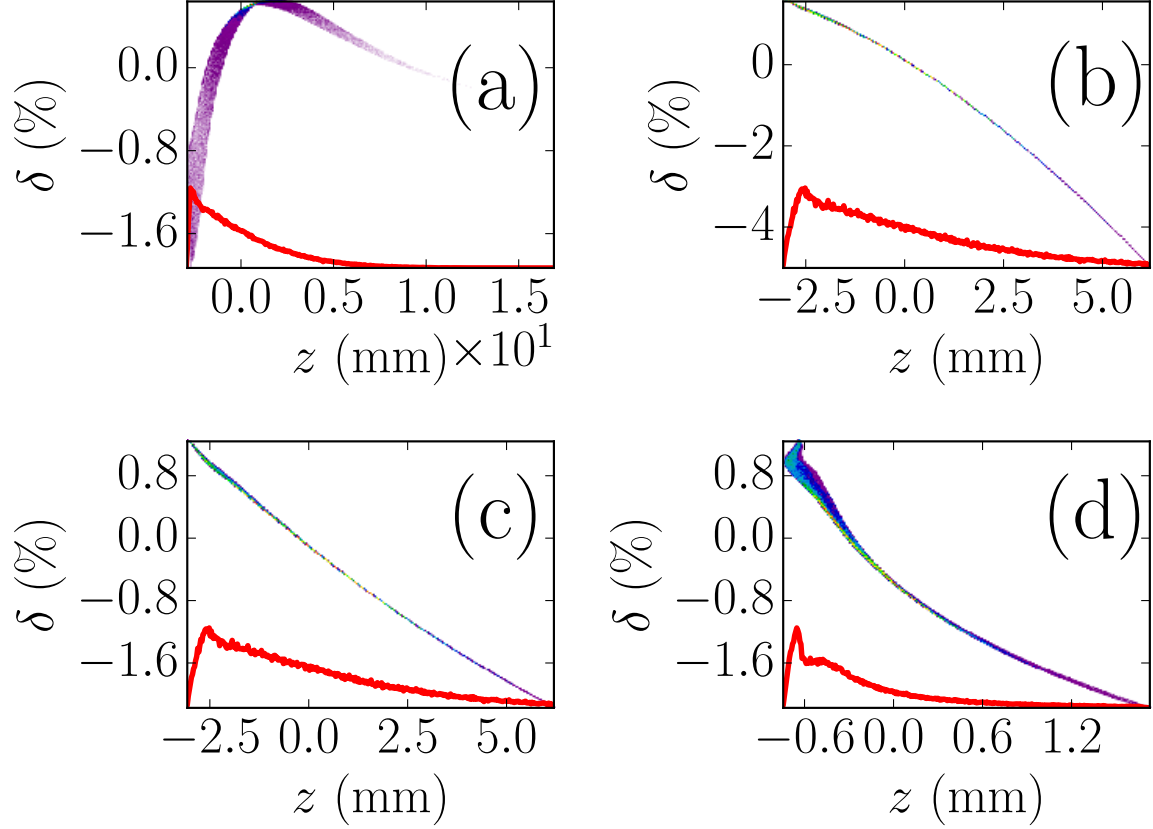


Figure 3.13: Snapshots of the longitudinal phase spaces and associate current profiles (red traces) upstream of L0 (a) and downstream of L0 (b), L39 (c) and BC (d). Simulations up to L39 are carried with ASTRA whereas a one-dimensional longitudinal-dynamics model is used for BC2. The head of the bunch corresponds to  $z > 0$ .

ratio as the bunch passes through the DLW are very close (within 10%) to the ones obtained with the scaled distribution. These results indicate that our proposed injector concept appears to produce the required current profile. Further studies, including a transverse beam dynamics optimization and the inclusion of collective effects such as coherent synchrotron radiation and space charge downstream of L39 and throughout the bunch compressor, will be needed to formulate a detailed design of the injector. We nevertheless stress that the simple model presented above confirms a plausible longitudinal-beam-dynamics capable of

preserving the formed current profiles after acceleration and compression. The final energies and peak currents are all within the parameters suggested in Ref. [8].

Table 3.3: Dielectric-line waveguide (DLW) parameters and resulting wakefield values using the current profile shown in Fig 3.12. The “ideal-” and “realistic-compression” entries respectively correspond to the cases when the final current profile is obtained via a simple longitudinal-axis scaling or via particle tracking.

parameter, symbol	value	units
DLW inner radius, $r_i$	750	$\mu\text{m}$
DLW outer radius, $r_o$	795	$\mu\text{m}$
DLW relative permittivity, $\epsilon_r$	5.7	–
DLW fundamental mode, $f_1$	369.3	GHz
<b>ideal compression:</b>		
Peak decelerating field, $ E_- $	14.01	MV/m
Peak accelerating field, $ E_+ $	75.55	MV/m
transformer ratio, $\mathcal{R}$	5.39	
<b>realistic compression:</b>		
Peak decelerating field, $ E_- $	12.84	MV/m
Peak accelerating field, $ E_+ $	63.87	MV/m
transformer ratio, $\mathcal{R}$	4.95	

We finally note that the generated current profiles are capable of supporting electric fields and transformer-ratios in a DLW structure with performances that strike a balance between the two cases listed as “case 1” and “case 2” in Table 1 of Ref. [8]; see Tab. 3.3. A simple estimate indicates that our drive bunch would require a DWFA linac of  $\sim 30$  m in order to accelerate an incoming 350-MeV witness bunch to a final energy of  $\sim 2$  GeV.

### 3.5 Experimental Generation and Characterization of Electron Bunches with Ramped Current Profiles in a Dual-Frequency Superconducting Linear Accelerator

It has long been recognized that linacs operating at multiple frequencies could be used to correct for longitudinal phase space (LPS) distortions and improve the final peak current [43, 44]. We show analytically and demonstrate experimentally how a two frequency linac could be operated to tailor the nonlinear correlations in the LPS thereby providing control over the current profile.

We first elaborate the proposed method using a 1D-1V single-particle model of the LPS dynamics and take an electron with coordinates  $(z, \delta)$  where  $z$  refers to the longitudinal position of the electron with respect to the bunch barycenter (in our convention  $z > 0$  corresponds to the head of the bunch) and  $\delta \equiv p/\langle p \rangle - 1$  is the fractional momentum spread ( $p$  is the electron's momentum and  $\langle p \rangle$  the average momentum of the bunch). Considering a photo-emission electron source, the LPS coordinates downstream are  $(z_0, \delta_0 = a_0 z_0 + b_0 z_0^2 + \mathcal{O}(z_0^3))$  where  $a_0$ , and  $b_0$  are constants that depend on the bunch charge and operating parameters of the electron source. For sake of simplicity we limit our model to second order in  $z_0$  and  $\delta_0$ . Next, we examine the acceleration through a linac operating at the frequencies  $f_1$  and  $f_n \equiv n f_1$  with total accelerating voltage

$$V(z) = V_1 \cos(k_1 z + \varphi_1) + V_n \cos(k_n z + \varphi_n), \quad (3.28)$$

where  $V_{1,n}$  and  $\varphi_{1,n}$  are respectively the accelerating voltages and operating phases of the two linac sections, and  $k_{1,n} \equiv 2\pi f_{1,n}/c$ . In our convention, when the phases between the linac sections and the electron bunch are  $\varphi_{1,n} = 0$  the bunch energy gain is maximum (this is refer

to as on-crest operation). Under the assumption  $k_{1,n}z_0 \ll 1$  and neglecting non-relativistic effects, the electron's LPS coordinate downstream of the linac are

$$(z_l = z_0, \delta_l = a_l z_0 + b_l z_0^2), \quad (3.29)$$

where

$$a_l \equiv a_0 - e(k_1 V_1 \sin \varphi_1 + k_n V_n \sin \varphi_n) / \bar{E}_l, \quad (3.30)$$

$$b_l \equiv b_0 - e(k_1^2 V_1 \cos \varphi_1 + k_n^2 V_n \cos \varphi_n) / (2\bar{E}_l) \quad (3.31)$$

with  $e$  being the electronic charge and  $\bar{E}_l$  the beam's average energy downstream of the linac. Finally, we study the passage of the bunch through an achromatic current-enhancing dispersive section [henceforth referred to as “bunch compressor” (BC)]. The LPS dynamics through a BC is approximated by the transformation

$$z_f = R_{56} \delta_l + T_{566} \delta_l^2, \quad (3.32)$$

where  $R_{56}$  (also referred to as longitudinal dispersion), and  $T_{566}$  are the coefficients of the Taylor expansion of the transfer map  $\langle z_f | \delta_l \rangle$  of the BC. Therefore the final position is given as function of the initial coordinates following

$$z_f = a_f z_0 + b_f z_0^2, \quad (3.33)$$

where

$$a_f \equiv 1 + a_l R_{56}, \quad (3.34)$$

and

$$b_f \equiv b_l R_{56} + a_l^2 T_{566}. \quad (3.35)$$

Taking the initial current to follow the Gaussian distribution

$$I_0(z_0) = \hat{I}_0 \exp[-z_0^2/(2\sigma_{z,0}^2)], \quad (3.36)$$

(where  $\hat{I}_0$  is the initial peak current), and invoking the charge conservation

$$I_f(z_f)dz = I_0(z_0)dz_0, \quad (3.37)$$

gives the final current distribution

$$I_f^u(z_f) = \hat{I}_0/\Delta^{1/2}(z_f) \exp[-(a_f + \Delta^{1/2}(z_f))^2/(8b_f^2\sigma_{z,0}^2)]\Theta[\Delta(z_f)] \quad (3.38)$$

where  $\Delta(z_f) \equiv a_f^2 + 4b_f z_f$  and  $\Theta()$  is the Heaviside function. The latter current distribution does not include the effect of the initial uncorrelated fractional momentum spread  $\sigma_{\delta,0}^u$ . The final current, taking into account  $\sigma_{\delta,0}^u$ , is given by the convolution

$$I_f(z_f) = \int d\tilde{z}_f I_f^u(\tilde{z}_f) \exp[-(z_f - \tilde{z}_f)^2/(2\sigma_u^2)] \quad (3.39)$$

where  $\sigma_u \equiv R_{56}\sigma_{\delta,0}^u$ . The final current shape is controlled via  $a_f$  and  $b_f$  and can be tailored to follow a linear ramp as demonstrated in Fig. 3.14.

The experiment described in this section was performed at the Free-electron LASer in Hamburg (FLASH) facility [45]. In the FLASH accelerator, diagrammed in Fig. 3.15, the electron bunches are generated via photoemission from a cesium telluride photocathode located on the back plate of a 1+1/2 cell normal-conducting rf cavity operating at 1.3

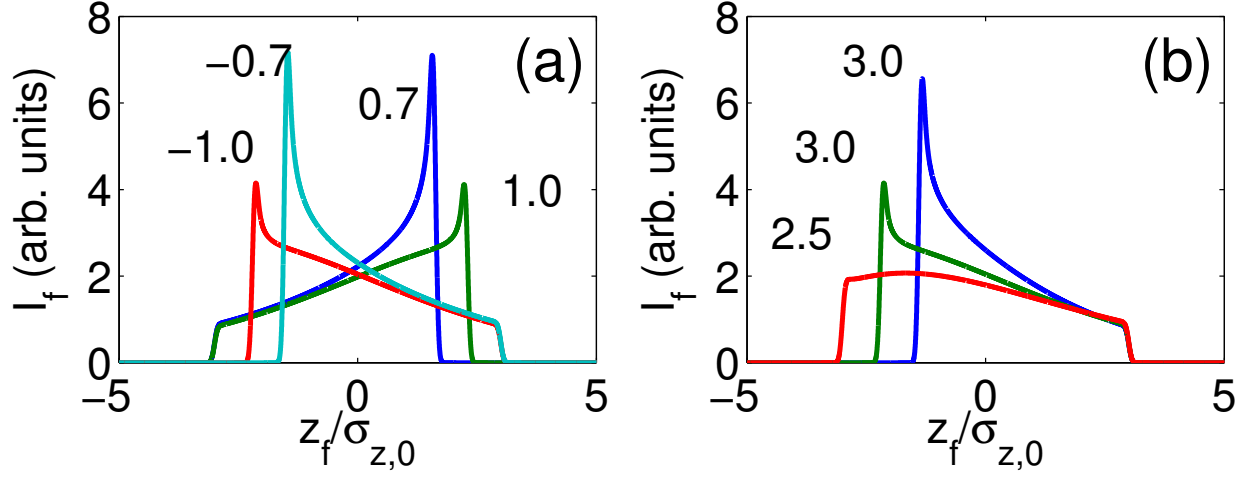


Figure 3.14: Analytically-computed current profiles for several values of  $b_f$  for fixed  $a_f = 2.5$  (a) and for several values of  $a_f$  with  $b_f = 0.7$  (b). The numbers in (a) [resp. (b)] are the values of  $b_f$  [resp.  $a_f$ ]; for all the cases  $\sigma_u = 0.05$ .

GHz on the  $\text{TM}_{010}$   $\pi$ -mode (rf gun). The bunch is then accelerated in a 1.3-GHz and 3.9-GHz superconducting accelerating modules (respectively ACC1 and ACC39) before passing through a bunch compressor (BC1). The ACC39 3rd-harmonic module was installed to nominally correct for nonlinear distortions in the LPS and enhance the final peak current of the electron bunch [46]. Downstream of BC1, the bunch is accelerated and can be further compressed in BC2. A last acceleration stage (ACC4/5/6/7) brings the beam to its final energy (maximum of  $\sim 1.2$  GeV). The beam's direction is then horizontally translated using a dispersionless section referred to as dogleg beamline (DLB). Nominally, the beam is sent to a string of undulators to produce ultraviolet light via the self-amplified stimulated emission free-electron laser (FEL) process. For our experiment, the bunches were instead vertically sheared by a 2.856-GHz transverse deflecting structure (TDS) operating on the  $\text{TM}_{110}$ -like mode and horizontally bent by a downstream spectrometer [47]. Consequently the transverse density measured on the downstream Cerium-doped Yttrium Aluminum Garnet (Ce:YAG) scintillating screen is representative of the LPS density distribution. The horizontal and vertical coordinates at the Ce:YAG screen are respectively  $x_s \simeq \eta \delta_F$ , where  $\eta \simeq 0.75$  m is

the horizontal dispersion function, and  $y_s \simeq \kappa z_F$  where  $\kappa \simeq 20$  is the vertical shearing factor and  $(z_F, \delta_F)$  refers to the LPS coordinate upstream of the TDS. The exact values of  $\eta$  and  $\kappa$  are experimentally determined via a beam-based calibration procedure.

Table 3.4: Settings of accelerator subsystems relevant to the LPS dynamics used in the experiment and simulations.

parameter	symbol	value	unit
ACC1 voltage	$V_1$	[140-157]	MV
ACC1 phase	$\varphi_1$	[-10,10]	deg
ACC39 voltage	$V_3$	[13,21]	MV
ACC39 phase	$\varphi_3$	[160-180]	deg
ACC2/3 voltage	$V_{1,2-3}$	311	MV
ACC2/3 phase	$\varphi_{1,2-3}$	0	deg
ACC4/5/6/7 voltage	$V_{1,4-7}$	233.9	MV
ACC4/5/6/7 phase	$\varphi_{1,4-7}$	0	deg
BC1 longitudinal dispersion	$R_{56}^{(1)}$	$\sim 170$	mm
BC2 longitudinal dispersion	$R_{56}^{(2)}$	$\sim 15$	mm
Single-bunch charge	$Q$	0.5	nC
Bunch energy	$E$	$\sim 690$	MeV

The accelerator parameters settings are gathered in Tab. 3.4. The nominal settings of BC2 were altered to reduce its longitudinal dispersion  $R_{56}^{(2)}$  and the ACC2/3 and ACC4/5/6/7 accelerating modules were operated on crest. Such settings insure that the BC2 and the DBL sections do not significantly affect the LPS beam dynamics. Therefore the measured current profile is representative of the profile downstream of BC1.

In order to validate the simple analytical model described above, numerical simulations of the LPS beam dynamics were carried using a multi-particle model. The simulations also enable the investigation of possible detrimental effects resulting from collective effects such as longitudinal space charge (LSC) and beam self interaction via coherent synchrotron radiation (CSR) [48]. In these simulations, the beam dynamics in the rf-gun was modeled with the particle-in-cell program ASTRA [27] and the obtained distribution was subsequently tracked

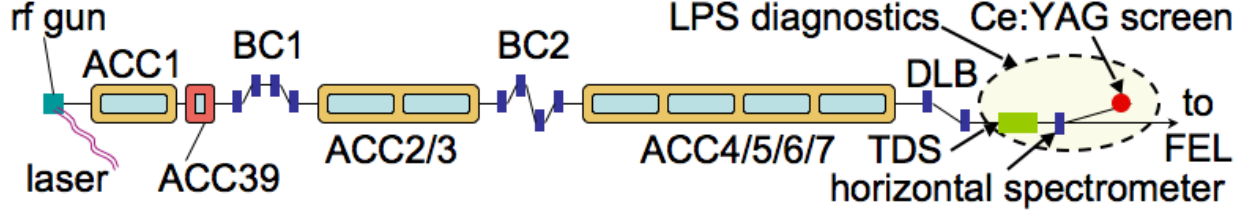


Figure 3.15: Diagram of the FLASH facility. Only components affecting the longitudinal phase space beam (LPS) dynamics of the bunches are shown. The acronyms ACC, BC, and DLB stand respectively for accelerating modules, bunch compressors, and dogleg beamline (the blue rectangles represent dipole magnets). The transverse deflecting structure (TDS), spectrometer and Ce:YAG screen compose the LPS diagnostics.

in the accelerating modules using a 1D-1V program that incorporates a one-dimensional model of the LSC. The program CSRTRACK [49], which self-consistently simulates CSR effects, was used to model the beam dynamics in the BC1, and BC2 sections. An example of simulated LPS distributions and associated current profiles computed for different settings of ACC1 and ACC39 parameters appear in Fig. 3.16. The results indicate that the production ramped bunches is possible despite the intricate LPS structures developing due to the collective effects and higher-order nonlinear effects not included in our analytical model. The simulations also confirm that the current profile upstream of the TDS (as measured by the LPS diagnostics) is representative of the one downstream of BC1.

Figure 3.17 displays examples of measured LPS distributions with associated current profiles obtained for different settings of ACC1 and ACC39. As predicted, the observed current profiles are asymmetric and can be tailored to be ramped with the head of the bunch ( $z > 0$ ) having less charge than the tail; see Fig. 3.17 (b-d). The latter feature is in contrast with the nominal compression case at FLASH where the LPS distortion usually results in a low-charge trailing population as seen in Fig. 3.17 (a).

We now quantify the performance of the produced current profiles to enhance beam-driven acceleration techniques by considering a drive bunch injected in a cylindrical-symmetric



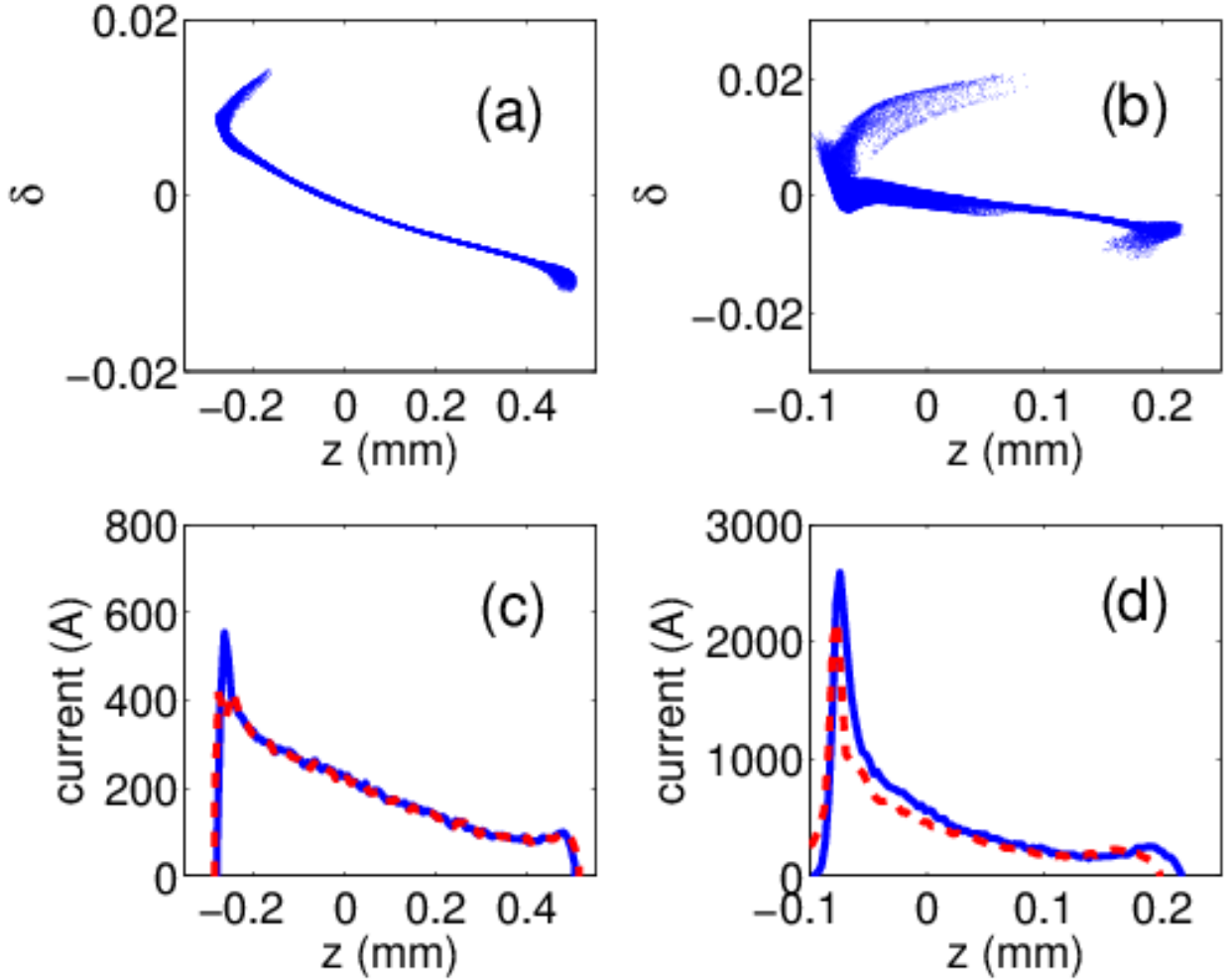


Figure 3.16: Simulated LPS distribution [(a) and (b)] with associated current profile downstream of BC1 (solid blue trace) and DBL (dash red trace) [(c) and (d)]. The set of plots [(a), (c)] and [(b), (d)] correspond to different  $(V_{1,3}, \varphi_{1,3})$  settings.

dielectric-lined waveguide (DLW) [50]. The DLW consists of a hollow dielectric cylinder with inner and outer radii  $a$  and  $b$ . The cylinder is taken to be diamond (relative electric permittivity  $\epsilon_r = 5.7$ ); and its outer surface is contacted with a perfect conductor; see Fig. 3.18 (a). The measured current profiles are numerically convolved with the Green's function associated to the monopole mode to yield the axial electric field [6]. These semi-analytical calculations were benchmarked against finite-difference time-domain electromagnetic simulations executed with VORPAL [51]. The transformer ratio is numerically inferred

as  $\mathcal{R} \equiv |E_+/E_-|$  where  $E_-$  (resp.  $E_+$ ) is the decelerating (resp. accelerating) axial electric field within (resp. behind) the electron bunch; see Fig. 3.18 (b). The achieved  $\mathcal{R}$  and  $E_+$  values as the structure geometry is varied are shown in Fig. 3.19. As  $a \in [20, 300] \mu\text{m}$  and  $b \in a + [20, 300] \mu\text{m}$  are varied the wavelengths of the excited wakefield modes change. The simulations show that profiles (b) and (c) of Fig. 3.17 can yield values of  $\mathcal{R} > 2$ . A possible configuration with  $(a, b) = (20, 60) \mu\text{m}$ , results in  $\mathcal{R} \simeq 5.8$  with  $E^+ \simeq 0.75 \text{ GV/m}$ ; see corresponding wake in Fig. 3.18 (b). Such high-field with transformer ratio significantly higher than 2 and driven by bunches produced in a superconducting linac could pave the way toward compact high-repetition-rate short-wavelength FELs [17].

Finally, the proposed technique could be adapted to non-ultrarelativistic energies using a two- (or multi-) frequency version of the velocity-bunching scheme [52]. Such an implementation would circumvent the use of a BC and would therefore be immune to CSR effects.

In summary we proposed and experimentally demonstrated a simple method for shaping the current profile of relativistic electron bunches. The technique is especially useful to convert Gaussian current profiles into asymmetric current profiles which can support large transformer ratios. Additionally, the relativistic regime in which this scheme was done can lead to current profiles with large charge densities as well which can support wakefields on the order of  $\sim \text{GV/m}$ . Finally the technique could be further refined by, e.g., including several harmonic frequencies.

### 3.6 Flat-beams for DWFA

So far our work has focussed on cylindrically-symmetric DLWs as discussed in 2. An attractive alternative to cylindrically-symmetric DLWs are slab-symmetric DLWs. Slab-symmetric DLWs natively mitigate a dipole mode which can deflect a beam and lead to beam

breakup (BBU) (see Ref. [9]). Although slabs generally offer smaller acceleration gradients, the open slab geometry allows the possibility of an adjustable inner aperture. Additionally, this also reduces the difficulty of practical concerns when aligning DLWs with a beam. One avenue worth exploring is the use of a “flat-beam” with a slab-symmetric structure, where in principle smaller gap apertures can be used with flatter beams which ultimately decreases the fundamental wavelength of the structure and increases the transformer ratio.

A flat beam can be formed using simple linear transformations directly out of a photoinjector as proposed in Ref. [53]. The method consists in generating an angular-momentum-dominated beam (also termed as “magnetized” beam) by immersing the photocathode in an axial magnetic field. The beam, after acceleration is then transformed into a flat beam using a set of skew quadrupoles. Upon proper tuning of the transformer, the expected normalized flat-beam emittances,  $\varepsilon_n^\pm$ , are given by [54]

$$(\varepsilon_n^+, \varepsilon_n^-) = \left( \frac{(\varepsilon_n^u)^2}{2\beta\gamma\mathcal{L}}, 2\beta\gamma\mathcal{L} \right), \quad (3.40)$$

where  $\varepsilon_n^u \equiv \beta\gamma\varepsilon_u$  is the normalized uncorrelated emittance of the magnetized beam prior to the transformer,  $\beta = v/c$ ,  $\gamma$  is the Lorentz factor,  $\mathcal{L} \equiv \langle L \rangle / 2p_z$ ,  $p_z$  is the longitudinal momentum, and  $\langle L \rangle \equiv eB_0\sigma_c^2$ , where  $e$  is the electron charge,  $B_0$  the axial magnetic field on the photocathode surface, and  $\sigma_c$  the root-mean-square (rms) transverse size of the drive-laser spot on the photocathode. An experimental investigation of angular-momentum-dominated beams and their flat-beam conversion was pioneered at Fermilab; see Ref. [55, 56]. At FAST the beam emittance for charge  $Q \in [0.02, 3.2]$  nC scales as  $\varepsilon_\perp^n = 2.11Q^{0.69} \mu\text{m}$  (where  $Q$  is the charge in nC) according to optimization performed in Ref. [57]. Taking the round-beam emittance value to correspond to  $\varepsilon_u = \varepsilon_\perp$ , the flat beam emittances will be  $\varepsilon_-^n$  and  $\varepsilon_+^n = (\varepsilon_u^n)^2 / \varepsilon_-^n$ . Therefore requiring the smallest emittance to be  $\varepsilon_-^n = 0.5 \mu\text{m}$  implies that  $\varepsilon_+^n = 50 \mu\text{m}$  to be consistent with a round-beam emittance of  $5 \mu\text{m}$  yielding to an emittance

ratio  $\rho \equiv \varepsilon_+^n / \varepsilon_-^n = 100$ . Numerical simulation of the FAST photoinjector setup to provide flat beams have confirmed this type of scaling.

Consider for example, a ramped bunch (recall  $\mathcal{R} = N\pi$ ) electron bunch with  $\varepsilon_n^u = 5 \mu\text{m}$ . Figure 3.20(top) presents the transformer ratio and peak accelerating field as a function of  $\rho$  for a 1-nC drive bunch given a structure with half-gap  $a = 165 \mu\text{m}$  and dielectric thickness of  $30 \mu\text{m}$ . If the DLW structure's gap is varied such that for a given emittance ratio the condition  $a = 4\sigma_y$  is satisfied, higher accelerating fields are possible; see Fig. 3.20(bottom). The total bunch length was taken to be 1.2 mm which leads to an increase of transformer ratio as  $a$  (and consequently the fundamental-mode wavelength) decreases.

The choice of the DLW structure geometry sets the maximum achievable accelerating field for a given bunch current distribution but is also constrained by the beam's transverse emittances. Here, we impose the DLW module to accelerate the incoming 250-MeV beam to 500 MeV within a maximum footprint of 10 m assuming a filling factor of 30% (3 meter total of active acceleration length). This sets a moderate requirement of  $\sim 100 \text{ MV/m}$  for the accelerating field. Taking a cylindrical-symmetric DLW, there are stringent requirements on the normalized transverse emittance  $\varepsilon_\perp$  for a given betatron function. Considering a structure with aperture radius  $a$  and length  $L$ , and requiring a transmission of  $3\sigma_\perp \leq a$  (where  $\sigma_\perp$  is the transverse beam size at the entrance/exit of the DLW) we can derive such a relationship; beginning with the usual beam-waist equation for a betatron function  $\beta(s)$

$$\beta(s) = \beta^* + \frac{s^2}{\beta^*} \quad (3.41)$$

where  $\beta^*$  is the minimum betatron value at  $s = 0$ , and recalling that the relationship between betatron function and physical beam size

$$\sigma = \sqrt{\frac{\beta(L/2)\epsilon^*}{\gamma}} \quad (3.42)$$

where  $\epsilon^*$  is the normalized emittance and  $\gamma$  is the Lorentz factor, we can establish

$$\varepsilon_{\perp} \leq \frac{4\gamma a^2 \beta^{*2}}{9(4\beta^{*2} + L^2)}, \quad (3.43)$$

For anticipated betatron functions of  $\sim 1$  m, the required transverse emittance would be  $\varepsilon_{\perp} \simeq 0.5 \mu\text{m}$ ; see Fig. 3.21. Such a low-emittance value is challenging to achieve for the anticipated nC charge need in the drive bunch. Simulations indicate that a minimum emittance around  $\varepsilon_{\perp} \sim 5 \mu\text{m}$  are achievable at the FAST photoinjector for  $Q = 3.2$  nC.

### 3.7 Experimental Opportunity for DWFA at FAST

The FAST facility at Fermilab is an L-band (1.3-GHz) superconducting linear accelerator, with a high-brightness photoinjector [57], with the possible future inclusion of advanced phase space manipulations such as flat-beam generation [58] and transverse-to-longitudinal exchange [59]. One application of FAST is to explore alternative acceleration schemes based on collinear beam-driven methods including dielectric-wakefield acceleration [10] and channeling-acceleration [60] methods.

The beamline configuration for our DWFA experiment is diagrammed in Fig. 3.22. The beamline comprises a L-band RF gun followed by two SCRF accelerating cavities (CAV1 and 2). The RF gun is nested in a pair of solenoidal lenses that can be used to produce beam with large angular momentum. Such a beam can be decoupled by a set of three skew quadrupole magnets downstream of CAV2 to produce flat beams — beams with high transverse emittance ratio — that can then be compressed using a magnetic chicane (BC1). The skew quadrupole magnets insertion is referred to as round-to-flat-beam transformer (RFBT). Downstream of

BC1, a triplet is used to focus the beam inside the DLW structure mounted in a 2-way goniometer; additionally, 2 linear stages will give control over the aperture of the DLW. The beam is finally drifted to the vertical spectrometer and directed to a Ce:YAG screen (X124). The screen has a vertical size of 38 mm and located at a dispersion of  $\eta_y = 0.44$  m permitting the measurement of beam spectrum of  $\delta p/p \sim 9$  % relative momentum spread. The high-resolution CCD (Prosilica GC 2450) could in principle enable resolution below  $\delta p/p \sim 10^{-4}$  for an ideal zero-emittance beam. The zero-charge betatron functions at X124 viewer are shown in Fig. 3.23 as a function of betatron functions obtained at the waist ( $\alpha_x = \alpha_y = 0$ ) in the DLW structure. The focusing between the DLW structure and X124 screen is solely achieved by the dipole (no quadrupole magnets are presently installed in this section).

For a vertical beta function of  $\beta^* \simeq 2$  m at the center of the DLW, the resulting  $\beta$  function at X124 is  $\beta_y^{X124} \simeq 1$  m limiting the energy resolution of the spectrometer to  $1.8 \times 10^{-4}$  (for a geometric emittance of  $\sim 6.3$  nm (corresponding to  $0.5 \mu\text{m}$  normalized with a Lorentz factor  $\gamma \simeq 80$ )).

Finally, a diagnostics station located downstream of the vertical spectrometer will enable the detection and autocorrelation of THz radiation generated by the bunch passing through the DLW structure.

Our experiment relies on the production of a flat beam, i.e., a beam with large transverse emittance ratio [61]. In our setup we produce flat beams with a low vertical emittance to mitigate horizontal-emittance-dilution effects arising in BC1 via space charge and coherent synchrotron radiation. Another benefit of this configuration is the low betatron contribution to the beam size at X124 given a vertical normalized emittance as low as  $\varepsilon_y \simeq 0.3 \mu\text{m}$ . An important challenge to overcome is the formation of compressed flat beam as described elsewhere [61].

### 3.8 Start-to-end simulations

The start-to-end simulations detailed below from cathode to a spectrometer were performed using particle-in-cell beam-dynamics program including ASTRA [27] and IMPACT-T [62]. The distribution downstream of the compressor was then matched to a waist at the DLW structure location with ELEGANT [63]. To model the beam self-interaction with its wakefield in the DLW, we use a modified version of IMPACT-T described in Ref. [10]. The dielectric-wakefield model is based on a 3-D Green's function approach discussed in 2. We consider a DLW structure composed of two parallel dielectric slabs. The separation between the inner surface and outer (metallized) surfaces is respectively  $2a$  and  $2b$ . The dielectric thickness is  $b - a$  and its relative permittivity is taken to be  $\varepsilon_r = 5.7$  to correspond to diamond.

#### 3.8.1 Case of single-mode DLW structures

Single-mode structures have the advantage to produce sinusoidal fields with known wavelengths. However since the beam's energy couples to a single mode, the resulting accelerating fields are generally smaller than the accelerating gradients achieved in multimode structures.

Due to the limited measurement apparatus in the planned experiment, we must establish a method of decoding the information from the projected energy modulated beam onto X124. Figure 3.24(a,b) illustrates the nominal LPS and the associated transverse beam distribution at the X124 location when no DLW structure is inserted in the beam path.

A complication arising from the long photocathode laser pulse regards the accumulation of a strong quadratic distortion on the LPS during acceleration in CAV1 and CAV2 which, after bunch compression results in a highly distorted distribution. The distribution has some

benefits to the investigation of wakefields as the charge concentration in the bunch head lead to high peak current ( $\sim 5$  kA) that excites strong wakes while the long trailing electron population samples this wake over several periods. This feature is clearly demonstrated in Fig. 3.24(c) where the LPS immediately downstream of a DLW structure with parameters  $a=100\text{ }\mu\text{m}$ ,  $b = 120\text{ }\mu\text{m}$ , and  $\varepsilon_r = 5.7$  is shown. The resulting transverse distribution on X124 shows some horizontal bands that correspond to the local maxima of the observed energy modulations on the LPS. Because of the large number of modulations, some smearing occurs at X124. In addition, we note that the Cherenkov pattern resulting from the dependence of the accelerating field on the transverse coordinates can be clearly resolved at X124 and could provide insightful measurements for precise benchmarking of the 3-D model.

### 3.8.2 Case of multi-mode DLW structures

As we mentioned above, the high-peak current and narrow width of the bunch head is capable of exciting the multi-THz regime. Therefore it is interesting to investigate the use of multi-mode structures which are generally comprised of thicker dielectric thicknesses. Additionally, this generally leads to higher axial peak fields in the DLW as multiple modes can constructively add up at the price of an uncontrollable accelerating-field region.

Figure. 3.25 shows examples of LPS and transverse beam distribution simulated at X124 for two dielectric structures with inner radius  $a = 100\text{ }\mu\text{m}$  and outer radius  $b = 150$  and  $200\text{ }\mu\text{m}$  for a DLW length of 2 cm. The experimental advantage for using multimode structures are the lower number of energy modulations which leads to fewer (and brighter) energy (horizontal) bands at X124.

For the case of multimode structures the peak accelerating field are 110 and 120 MV/m for respectively a dielectric thickness of  $\delta = 50$  [Fig. 3.25(a,b)] and  $100\text{ }\mu\text{m}$  [Fig. 3.25(c,d)] while



the single-mode structure was supporting a field amplitude of 105 MV/m [Fig. 3.24(c,d)]. We again mention that using a flatter beam would allow smaller inner-apertures which could lead to larger accelerating fields. However, due to the limited X124 screen size of 38 mm, the measurement of larger accelerating gradients would requier either shorter length DLWs or lower charge bunches.

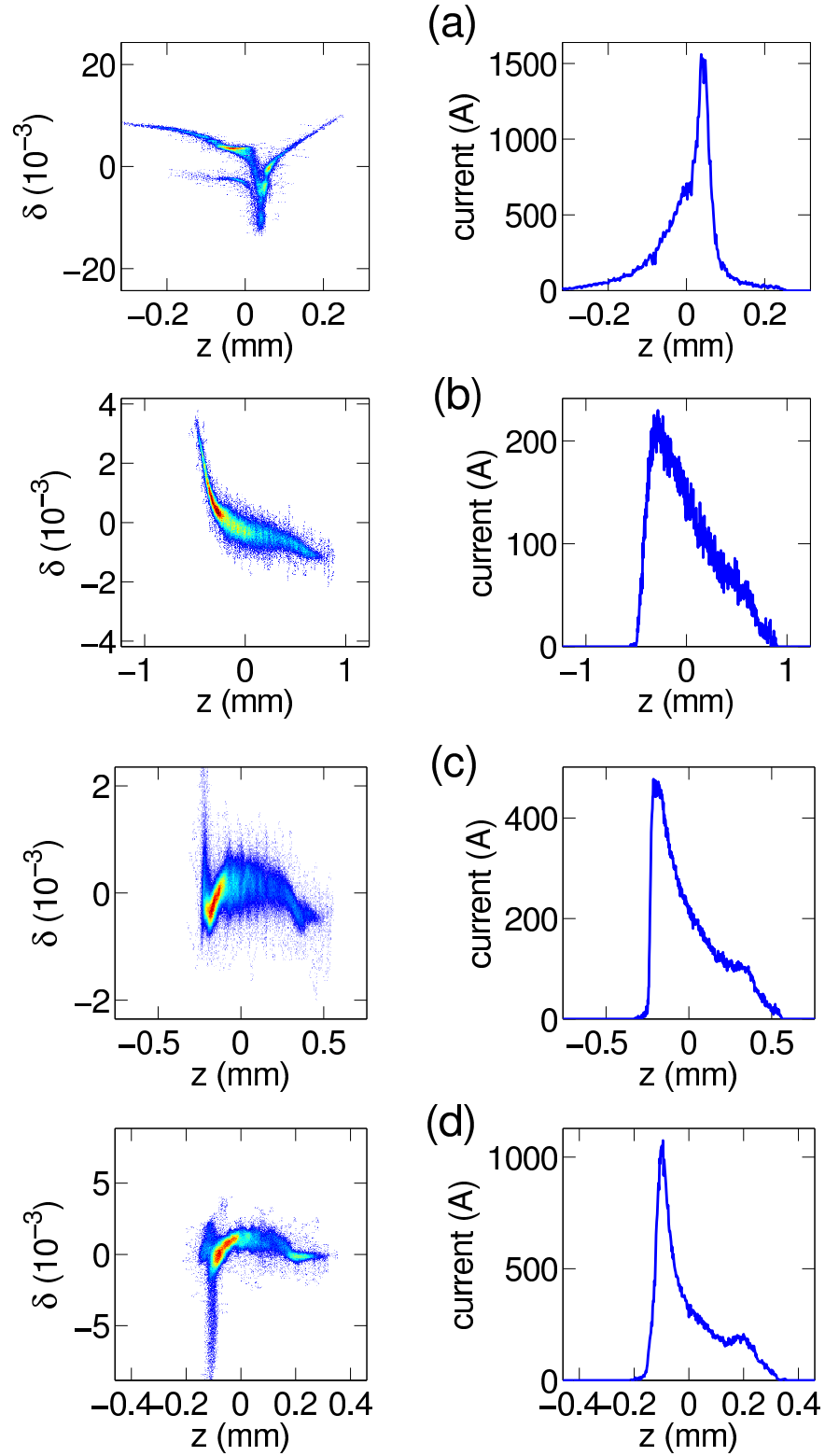


Figure 3.17: Snapshots of the measured longitudinal phase spaces (left column) and associated current profiles (right column) for different settings of the ACC1 and ACC39 accelerating modules. The values  $(V_1, \varphi_1; V_3, \varphi_3)$  [in (MV, °, MV, °)] are: (150.5, 6.1; 20.7, 3.8), (156.7, 3.8; 20.8, 168.2), (155.6, 3.6; 20.6, 166.7), and (156.8, 4.3; 20.7, 167.7) for respectively case (a), (b), (c), and (d).

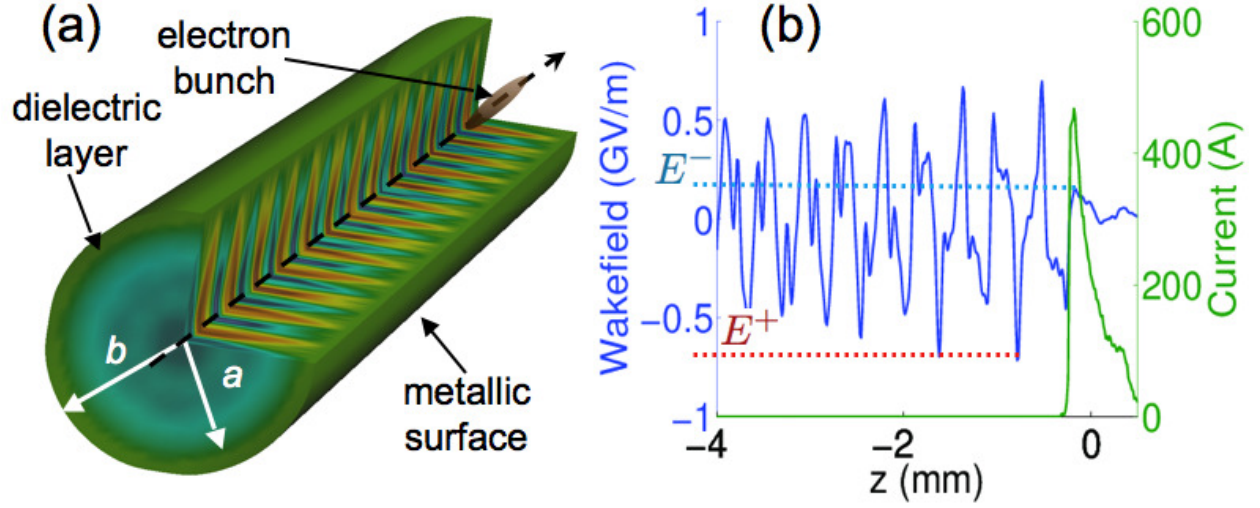


Figure 3.18: Cylindrical-symmetric dielectric-loaded waveguide considered (a) and axial wakefield produced by the current profile shown in Fig. 3.17 (c) for  $(a, b) = (20, 60) \mu\text{m}$ .

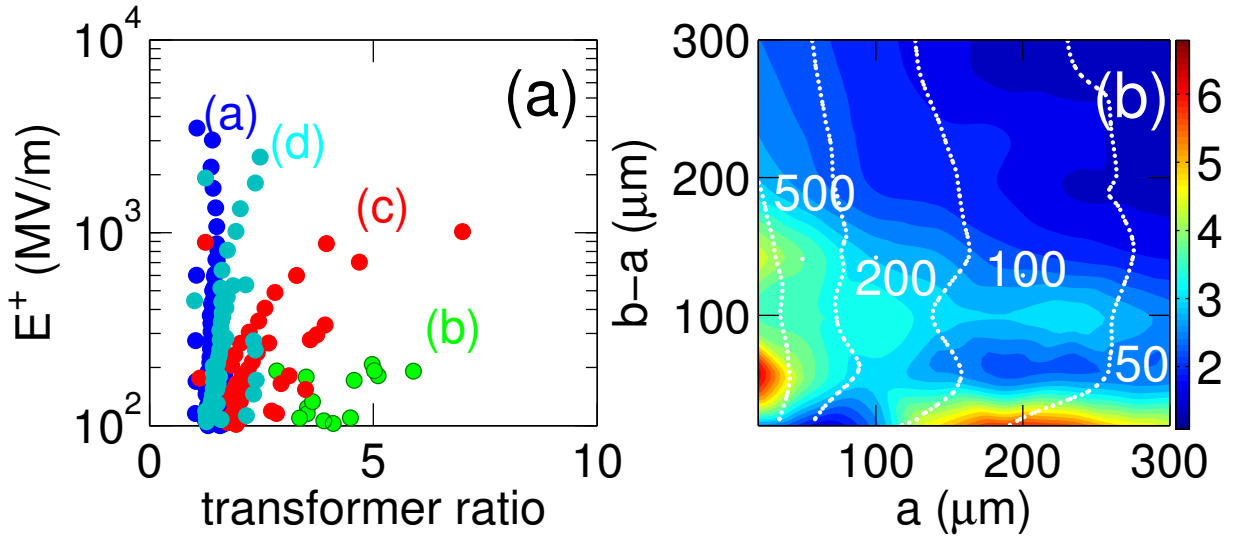


Figure 3.19: Simulated transformer ratio versus peak accelerating field (a) for the four measured current profiles (displayed as different colors with label corresponding to cases shown in Fig. 3.17). Transformer ratio (false color map) as a function of the DLW inner radius  $a$  and dielectric layer thickness  $b-a$  with corresponding  $|E^+|$  shown as isoclines with values quoted in MV/m for case (c) of Fig. 3.17.

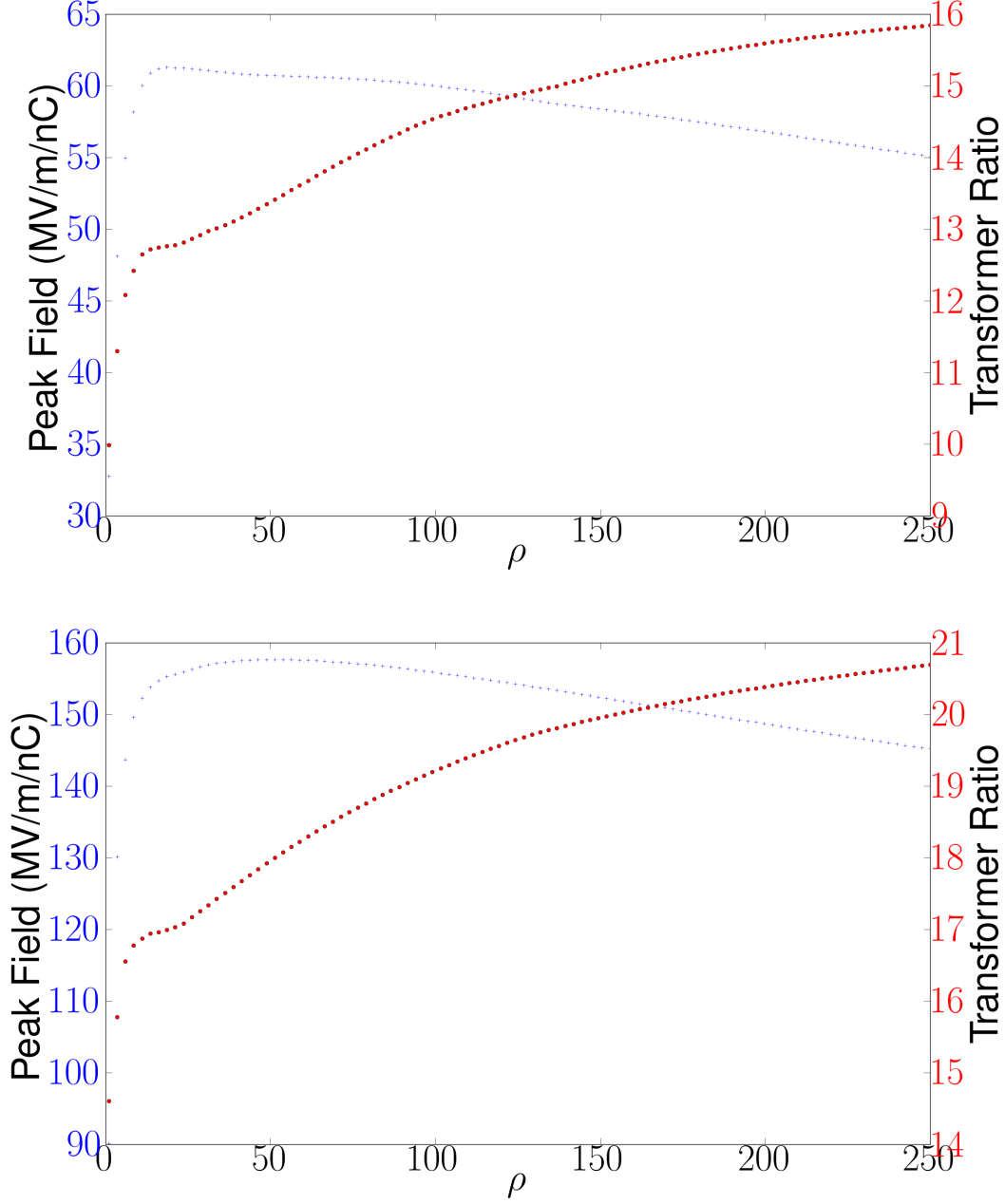


Figure 3.20: Peak accelerating electric field (blue trace) and transformer ratio (red trace) as a function of emittance ratio  $\rho = \varepsilon_n^+/\varepsilon_n^-$  for a 1 nC electron bunch with 4D emittance  $\varepsilon_n^u \equiv \varepsilon_n^+\varepsilon_n^- = 5 \mu\text{m}$ . The structure parameters is  $a = 165 \mu$  and  $b - a = 30 \mu\text{m}$  (top) and taken to be variable such that  $a = 4\sigma_y$  and  $b - a = 30 \mu\text{m}$  (bottom). The bunch is taken to be linearly-ramped with total length of 1.2 mm.

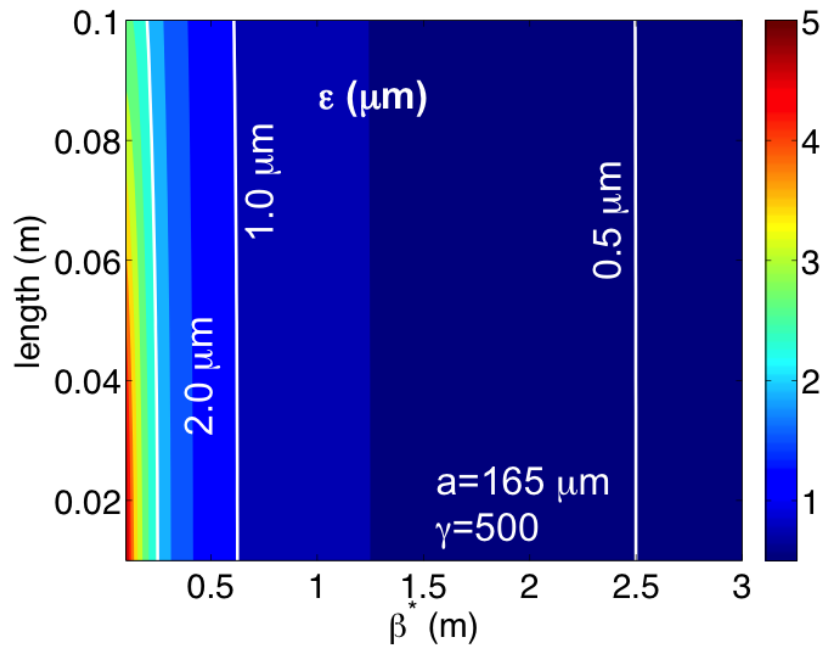


Figure 3.21: Required normalized transverse emittance ( $\mu\text{m}$  colorscale) as a function of  $\beta^*$  function and DLW structure length. The DLW inner aperture is taken to be  $a = 165 \mu\text{m}$  and the beam Lorentz factor is  $\gamma = 500$ .

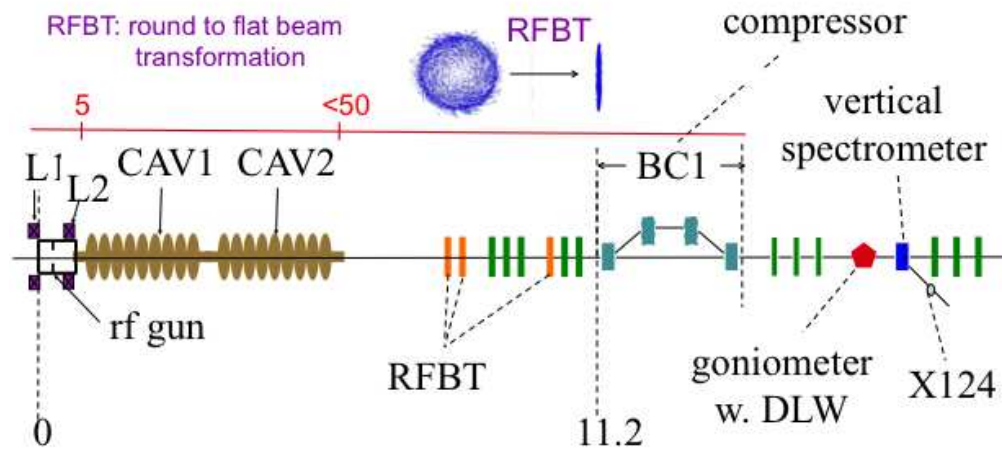


Figure 3.22: Layout of the FAST photoinjector. L1 and L2 are solenoids, and CAV1 and 2 SCRF cavities. The red and green rectangle represent quadrupole magnets. X124 is a Ce:YAG screen

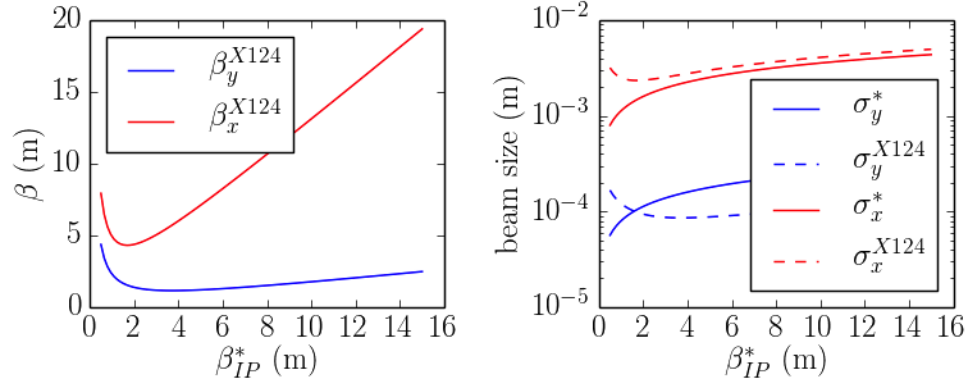


Figure 3.23: The zero-charge betatron functions (left) and the transverse RMS beam sizes (right) along the FAST accelerator with flat beams.

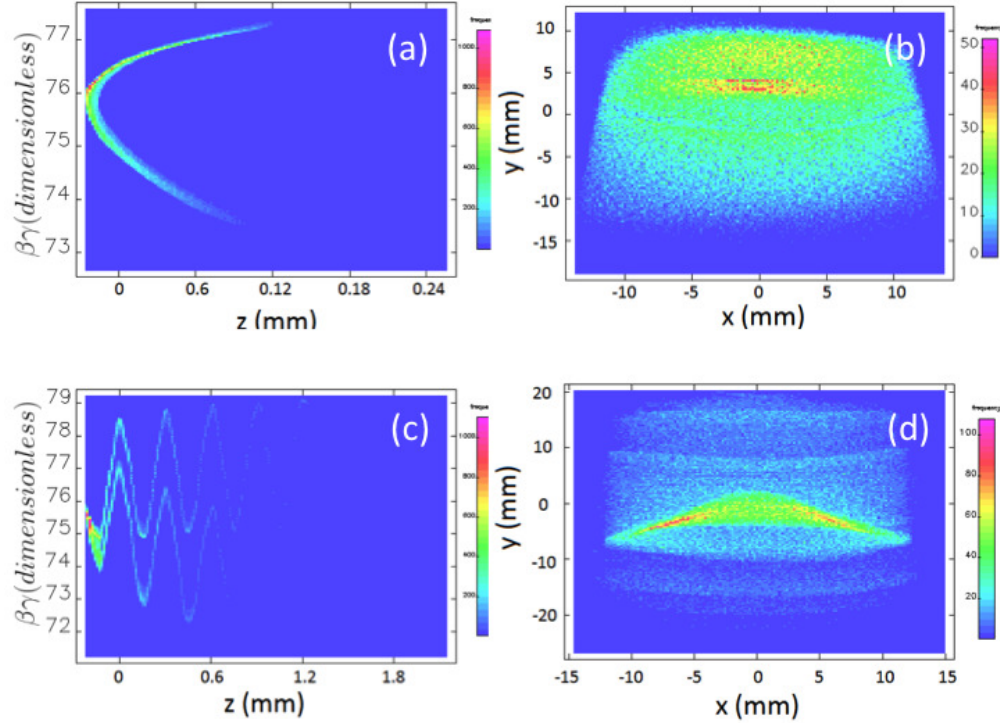


Figure 3.24: Longitudinal phase spaces (a,c) and associated transverse distributions at X124 (b,d) without (a,b) and with (c,d) a DLW structure. The DLW structure used for (c,d) has parameters  $a=100 \mu\text{m}$ ,  $b = 120 \mu\text{m}$ , and  $\varepsilon_r = 5.7$

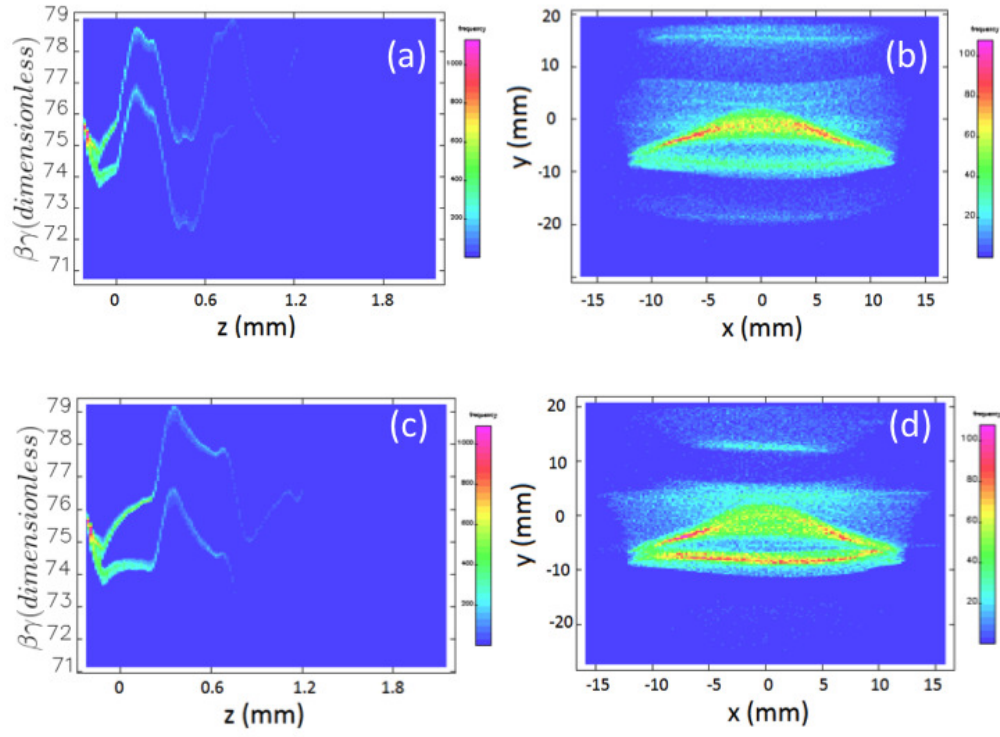


Figure 3.25: Longitudinal phase spaces (a,c) and associated transverse distributions at X124 (b,d) for a dielectric thickness of  $\delta = 50$  (a,b) and  $100$   $\mu\text{m}$  (c,d) DLW structure. The DLW structure other parameters are  $a = 100$   $\mu\text{m}$ ,  $b = a + \delta$ , and  $\varepsilon_r = 5.7$ .



## CHAPTER 4

# BALLISTIC BUNCHING AND BEAM MANIPULATION

### 4.1 Introduction

Low-energy ( $\lesssim 10$  MeV) electron beams are conventionally produced in photoemission electron sources based on radio frequency (RF) guns or “photoinjectors”. The final bunch length downstream of a photoinjector is dictated by the initial parameters including the photocathode-laser pulse duration, transverse spot size, the electric-field amplitude in the gun cavity and its phase relative to the laser. Typically, bunch lengths on the order of picoseconds are commonly produced in L- and S-bands RF guns. Shortening these bunches or producing trains of sub-ps microbunches is appealing to a variety of applications including ultra-fast electron diffraction [64, 65], coherent accelerator-based, e.g., THz light sources [66, 67], and injectors for short-wavelength advanced-accelerator concepts [68, 69].

To date, bunch compression to produce kA peak currents is often realized after acceleration to  $\gtrsim 100$  MeV by employing dispersive sections arranged as, e.g., magnetic chicanes [70]. Alternative methods to shorten a relativistic bunch also include velocity bunching [71, 72, 73, 74], and ballistic bunching using an accelerating cavity operating at zero crossing. The latter method demonstrated bunching at the sub-100-fs time scale [29] and could possibly produce shorter temporal structures [75]. Similar methods have been extended to the mm-wave regime, e.g., by coupling laser-produced THz pulses to the beam using undulators [76] or dielectric waveguides [77].

In addition, several techniques have demonstrated narrow-band THz radiation generation with photoinjector beams by coupling a density-modulated bunch with electromagnetic-radiation mechanisms (using e.g. coherent transition radiation) [20, 22, 46, 78, 79]. Among these techniques, two of them are based on impressing a density modulation using a temporally-modulated photocathode-laser pulse [78, 79, 80]. The use of such a temporally-modulated laser was also experimentally shown to support the formation of short-current spikes via wave breaking seeded by nonlinear longitudinal space-charge effects [81].

Recently, a technique to produce trains of microbunches based on a dielectric-lined waveguide (DLW) was realized in a  $\sim 70$ -MeV accelerator [82]. In the latter experiment a density modulation was produced using a small chicane to provide the longitudinal dispersion necessary to convert the energy modulation imparted by the beam self-interaction with its short-range wakefield in the DLW structure.

In this chapter, we propose a simple method extending the mechanism proposed in Ref. [82] to low-energy beams. In our configuration a  $\sim 5$ -10 MeV ps-duration beam is energy-modulated as it passes through a DLW and ballistically bunches in a subsequent drift. Our approach is similar to the bunching technique commonly used in klystrons [83, 84]. Owing to the low intrinsic energy spread typically achieved in photoinjectors, final beam currents in excess of kA's could be produced.

## 4.2 Ballistic compression from wakefield-induced energy modulations

In contrast with an energy modulation imparted by external fields (e.g. from lasers or RF cavities), the modulation imparted via wakefields depends on the longitudinal bunch

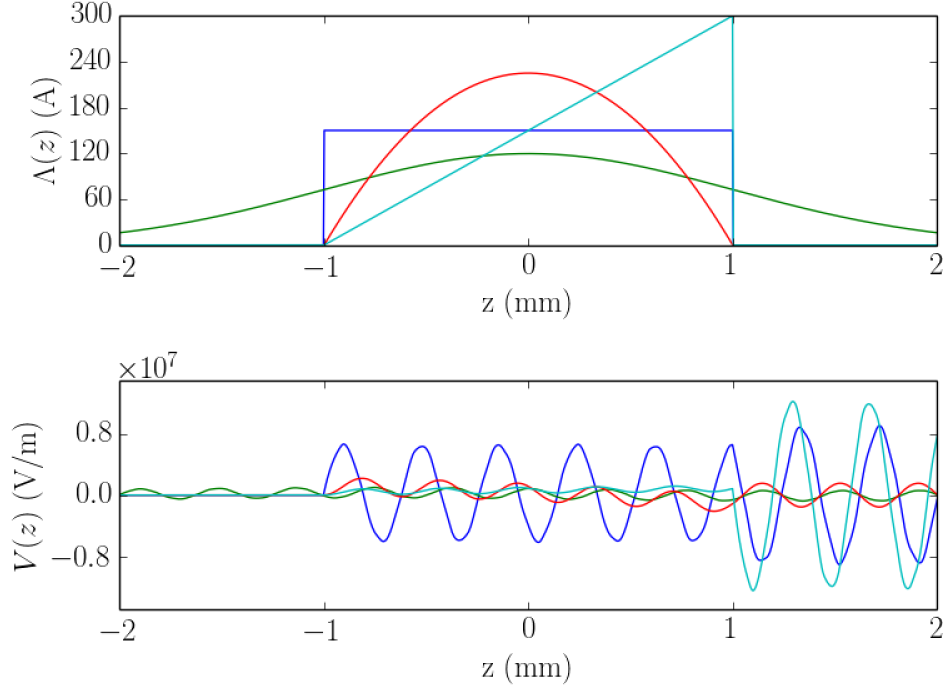


Figure 4.1: Charge distributions (top) and corresponding wake potential (bottom) for the same structure parameters as shown in Fig. 2.4 and for a 1-nC Gaussian bunch with variance (Gaussian distribution) or hard-edge half size (other distributions) of 1 mm. The green, blue, red, and turquoise traces respectively correspond to the case of a Gaussian, parabolic, uniform, and linearly-ramped current distributions. The head of the bunch is at  $z \leq 0$ .

shape. In particular, given the selected parameters for the DLW structure, one should ideally select an electron-bunch distribution with spectral contents capable of exciting the mode(s) supported by the structure; see Fig. 4.1.

In order to illustrate the proposed concept we elaborate a simple model based on the ideal case of a line-charge electron bunch with a parabolic charge-density profile  $\Lambda(z) = [3Q/(2a^3)](a^2 - z^2)$  for  $|z| \leq a$  where  $Q$  is the total bunch charge and  $a$  the half width of the

distribution; see Fig. 4.2(a). The corresponding change in energy along the bunch is given by

$$\Delta E(z) \simeq \sum_{m=1}^{+\infty} \mathcal{E} \{ \sin[k_m(z+a)] - k_m a \cos[k_m(z+a)] + k_m z \}, \quad (4.1)$$

where  $\mathcal{E} \equiv \frac{3\kappa_m L_{dlw} Q}{2k_m^3 a^3}$ . Considering only the fundamental mode ( $m = 1$ ) and assuming a “cold” initial LPS with no correlation so that  $(z_i, \delta_i = 0)$  (for all  $i$ ), where  $z_i$  and  $\delta_i$  are respectively is the axial coordinate and fractional momentum spread associated to the  $i^{th}$  electron. The final fractional momentum spread downstream of the DLW structure becomes

$$\delta_f(z_f) \simeq \frac{E_i + \Delta E(z_f)}{E_f} - 1, \quad (4.2)$$

where  $E_i$  is the bunch’s initial mean energy,  $E_f \equiv E_i + 1/Q \int \Delta E(z) \Lambda(z) dz$  its final mean energy, and  $z_f = z_i$ . For the case of short modulation  $ka \gg 1$  the final energy can be approximated as  $E_f \simeq E_i - \frac{3L_{dow}\kappa_1 Q}{2a^4 k_1^4} \simeq E_i$

After a section with longitudinal dispersion  $R_{56}$ , the energy modulation induces a density modulation and the final longitudinal coordinate of an electron is mapped as  $z_d = z_f + R_{56}\delta_f$  under a linear single-particle dynamics approximation.

We first consider the case when the root-mean-square (rms) bunch length satisfies  $\sigma_{z,i} \equiv \langle z_i^2 \rangle^{1/2} \gtrsim \lambda_1 \equiv 2\pi/k_1$  so that an energy modulation along the bunch can be impressed; Fig. 4.2(b, red trace). In such a case the second term in Eq. 4.1 dominates the short-wavelength modulation structure and the final longitudinal coordinate is approximately given by

$$z_d \simeq z_i - \frac{R_{56}\mathcal{E}}{E_i} \cos[k_1(z_f + a)]. \quad (4.3)$$

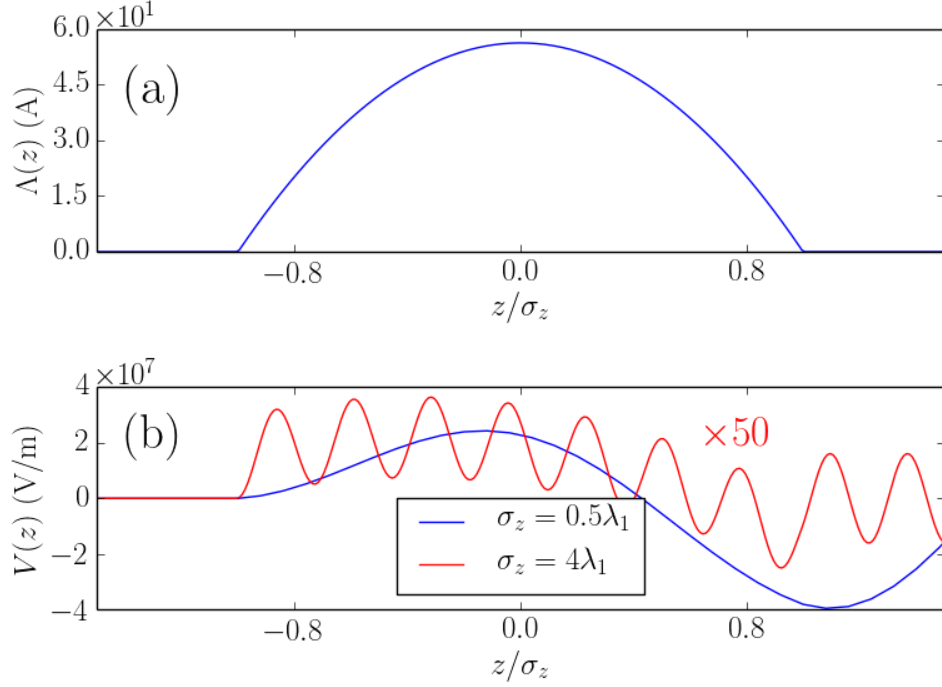


Figure 4.2: Charge distributions (a) and corresponding wake potential (b) for two cases of ratio between the rms bunch length  $\sigma_z$  and fundamental-mode wavelength  $\lambda_1$ . The DLW structure parameters are identical to one used in Fig. 2.4. The head of the bunch corresponds to  $z \leq 0$ . The wake potential associated to the  $\sigma_z = 0.5\lambda_1$  case is scaled by a factor 50 for clarity.

At the zero-crossing locations, i.e. the locations along the bunch  $z_{f,n}$  such that  $\delta_f(z_{f,n}) \propto \cos[k_1(z_{f,n} + a)] = 0$ , the local LPS correlation is given by

$$\mathcal{C} \equiv \left. \frac{d\delta_f}{dz_f} \right|_{z_{f,n}} \simeq \frac{k_1 \mathcal{E}}{E_i}. \quad (4.4)$$

The maximum bunching occurs at these zero-crossing points when the following beamline provides a longitudinal dispersion  $R_{56} = -\frac{1}{\mathcal{C}}$ . The characteristic length of the microbunches formed is approximately given by  $\sigma_z \simeq R_{56} \tilde{\sigma}_\delta$  where  $\tilde{\sigma}_\delta$  is the uncorrelated (or slice) rms fractional momentum spread. The microbunches' separation is  $\Delta z \equiv z_{f,n} - z_{f,n-1} \simeq \lambda_1$  for

an incoming beam with vanishing correlated energy spread.

At relativistic energies, the longitudinal dispersion  $R_{56}$  necessary to form the microbunches is often provided by a dispersive section, e.g., a bunch-compressor chicane [70] as accomplished in Ref. [82]. Here we note that at energies below  $\sim 10$  MeV (non-ultra-relativistic regime), the large LPS slope resulting from the large axial fields supported in a DLW requires a relatively small  $R_{56}$  that can be readily produced by a drift space. A drift with length  $D$  has a longitudinal dispersion

$$R_{56} \simeq -\frac{D}{\gamma^2}, \quad (4.5)$$

where  $\gamma$  is the bunch's Lorentz factor and we take  $\beta \equiv (1 - 1/\gamma^2)^{1/2} \simeq 1$  for simplicity.

Practically, for a  $\sim 5$ -MeV electron bunch passing through a 10-cm long DLW structure capable of supporting  $\sim 0.5$  MV/m peak field a “local” chirp  $\mathcal{C} \simeq 10^3 \text{ m}^{-1}$  can be obtained for a 0.5-mm modulation wavelength. The corresponding local density spike could form via ballistic bunching after a drift of length below  $D \leq 1$  m. The expected modulation amplitude  $\sim 0.5$  MeV is much larger than the typical uncorrelated energy spread of a few keV routinely achieved in RF guns [85, 86]. Additionally, the relatively low  $R_{56}$  and small uncorrelated energy spread are also beneficial to the production of very short ( $< 100$ -fs) density spikes. This simple estimate motivates further investigation of the scheme using a bunch generated by a conventional photoemission electron gun.

In addition, furthering our point about the dependence of the energy modulation on bunch shape we now examine the case when the rms bunch length fulfills  $\sigma_{z,i} \simeq \lambda_1/2$ ; see Fig. 4.2(b, blue trace). In this regime, the induced energy change along the bunch produces

an energy depression between the head and tail of the bunch and has the proper sign to be compressed via ballistic bunching. Although the introduced chirp is nonlinear, it can eventually lead to the production of a high peak current. This approach, however, only bunches a fraction of the bunch and actually debunches the head of the bunch. Despite this drawback, this scheme is appealing given its simplicity and absence of need for a precisely synchronized external field as used in ballistic bunching using a buncher cavity [29]. This passive bunching method is therefore inherently self-synchronized and in principle not subject to time jitter (the main source of jitter is associated to charge fluctuations that impact the imparted energy modulation and could consequently result in shot-to-shot fluctuations of the peak current).

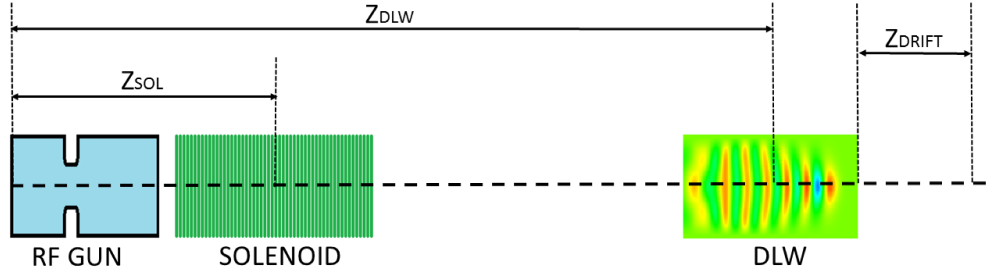


Figure 4.3: Overview of the photoinjector setup used for the numerical simulations. The distances  $Z_{SOL}$  and  $Z_{DLW}$  correspond respectively to the location of the center of the solenoid and DLW structure referenced to the photocathode surface, and  $Z_{drift}$  represents the drift distance downstream of the DLW structure necessary for ballistic bunching.

Finally, it should be pointed out that higher-order (e.g. dipole) modes can also affect the bunch transverse dynamics but are neglected in the present treatment as we assume the bunch is cylindrical-symmetric and axially centered on the DLW axis. Given the short length of the DLW considered in the remainder of this chapter, possible detrimental effects on the transverse beam dynamics can be practically corrected, e.g., by mounting the DLW structure on translational stages.

### 4.3 Numerical modeling and analysis

To explore the possibilities discussed in the previous section we perform beam-dynamics simulations. The numerical simulations are carried with the beam-dynamics program ASTRA [27] (see 2.4). The beam-DLW interaction is modeled via the Green's function approach briefly outlined above and detailed in Ref. [87]. The Green's function employed in our simulations throughout this chapter is constructed using the wake associated to the four modes of the considered structure as supported by Fig. 2.4. In most of our simulations the electron bunch is modeled as an ensemble of 100,000 macroparticles. The grid used to bin the macroparticle distribution within the cylindrical-symmetric space charge algorithm is typically setup with a number of radial and longitudinal bins  $n_r = 11$  and  $n_z = 500$ . The large number of longitudinal bins ensures a temporal resolution at the sub-50-fs scale is realized for most of the current distribution generated throughout this chapter. We note however, that binary collisions (Boersch effect [88]) are not taken into account in the mean-field space-charge algorithm employed in ASTRA and might result in a degradation of the peak current quoted in this chapter.

To characterize the temporal structure of the bunch, we represent the macroparticles' temporal distribution as  $\Lambda(z) = \frac{1}{N} \sum_{i=1}^N \delta(z - z_i)$  and compute the bunch form factor (BFF)  $\tilde{F}(\omega) = |1/(2\pi) \int_{-\infty}^{+\infty} \Lambda(z/c) e^{-i\omega t}|^2$  as

$$\tilde{F}(\omega) = \frac{1}{N^2} \left( \left| \sum_i^N \cos \frac{\omega z_i}{c} \right|^2 + \left| \sum_i^N \sin \frac{\omega z_i}{c} \right|^2 \right), \quad (4.6)$$

where  $N$  is the number of macroparticles used in the simulation. The BFF is commonly used to characterize the performance of accelerator-based radiation source [89]. We note that in some cases, e.g. for the production of short-wavelength coherent radiation, transverse



suppression effects might be prominent and should be properly accounted for by utilizing a three-dimensional expression for the BFF; see, e.g., Ref. [48].

### 4.3.1 Sub-picosecond bunch train formation

We first investigate the practical realization of the scheme described in section 4.2 to produce trains of sub-picosecond bunches and to demonstrate the versatility of the method, we consider two examples of implementation. The generic setup consists of an RF-gun electron source followed by a DLW as diagrammed in Fig. 4.3. Downstream of the DLW the beam is focussed with a second solenoid, e.g., to produce a waist at the location a transition-radiation target. The RF gun is taken to be an S-band (2.856 GHz) 1/2-cell cavity similar to the one currently in use at the linac coherent light source (LCLS) [26]. Similar results are then confirmed using a 1/2-cell L-Band (1.3 GHz) gun similar to the one used at the FLASH facility in DESY [90].

The photocathode-laser distribution was chosen to follow a plateau temporal distribution and its transverse size along with the location of the DLW, and solenoid strength were optimized using a multi-objective optimizer [40] to maximize beam transmission through the structure and minimize the transverse beam size at the DLW center. The list of optimized operating parameters are gathered in Tab. 4.1 (“S-band” column). We note that the choice of the DLW parameters is a compromise between modulation wavelength  $\lambda_1$ , energy modulation amplitude – which affects the bunching length – and beam transmission. For example, a shorter DLW structure relaxes the requirements on beam sizes and emittances at the structure, but necessitates a longer drift to bunch the beam (as the amplitude of the imparted energy modulation is smaller than for a longer structure). Additionally, the number of potential microbunches depends on the incoming bunch length and  $\lambda_1$ . For example, a

Table 4.1: Beamline settings and DLW-structure parameters used in the ASTRA simulations. The beamline configuration with some of the associated parameters is depicted in Fig. 4.3.

	S-Band	L-Band	
parameter			units
Laser pulse RMS duration	3	7	ps
Laser pulse rise time	100	100	fs
Laser RMS spot size	0.72	1.1	mm
Initial charge	1	1	nC
Peak field on cathode	120	34	MV/m
Solenoid 1 position	0.20	0.0	m
Solenoid 1 strength	0.26	0.17	T
Solenoid 2 position	1.35	1.0	m
Solenoid 2 strength	0.45	0.15	T
DLW position	0.9	0.34	m
DLW inner radius ( $a$ )	350	500	$\mu\text{m}$
DLW outer radius ( $b$ )	363	550	$\mu\text{m}$
DLW length	11	4	cm
DLW fund. frequency $f_1$	1000	400	GHz
Transmission through DLW	85	98	%
Average kinetic energy	6.1	3.8	MeV

Gaussian bunch with rms length  $\sigma_z$  will typically result in the formation of  $N_b \sim 4\sigma_z/\lambda_1$  microbunches. Additionally, varying  $\sigma_z$  for a given bunch charge and fundamental-mode wavelength  $\lambda_1$  affects the initial peak current and consequently the amplitude of the imparted energy modulation as inferred from Eq. 4.2.

We present, for the “S-band” case listed in Tab. 4.1, the evolution of the BFF over a frequency range  $f \equiv \frac{\omega}{2\pi} \in [0.5, 3.5]$  THz as a function of the drift distance from the DLW exit ( $z_{drift}$ ) in Fig. 4.4(a). The corresponding longitudinal-density evolution appears in Fig. 4.4(b). For this set of parameters, 10 microbunches are produced and a maximum bunching of  $\tilde{F}(\omega_1) \simeq 0.20$  is obtained at the DLW fundamental mode’s wavelength  $\lambda_1 \simeq 382 \mu\text{m}$ . In addition, harmonics of the fundamental mode  $f_{1,n} = n f_1$  are observed. For the selected DLW parameters and the corresponding thin dielectric layer, only the fundamental mode significantly influences the bunch dynamics.

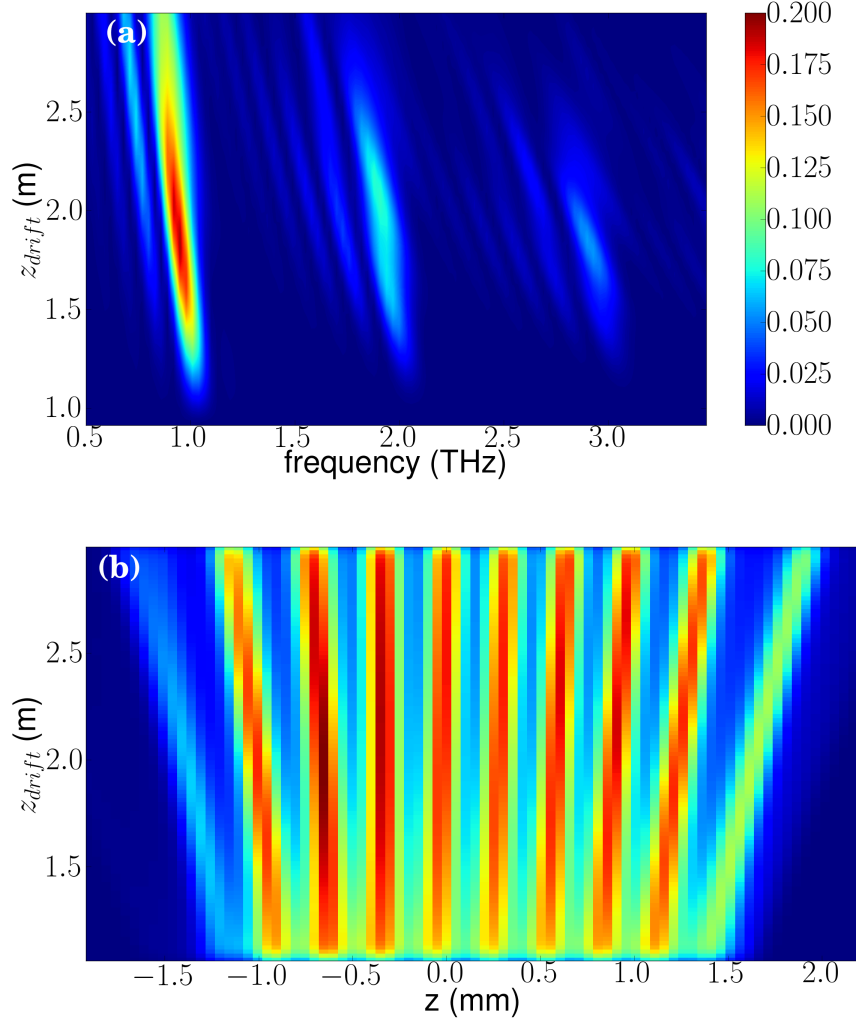


Figure 4.4: Bunch form factor (BFF) (a) and bunch longitudinal density (b) evolution as a function of the drift length referenced with respect to the DLW exit. The simulations correspond to the parameters listed under the “S-band” column in Tab. 4.1.

The current and LPS distributions at the DLW exit and at the location of maximum bunching (at  $s \simeq 1.30$  m from the photocathode) appear in Fig. 4.5. Peak currents on the order of 1 kA are achieved for a beam with mean momentum of  $\langle p_z \rangle \simeq 6.12$  MeV/c. The shortest current spike generated has an full-width half-max (fwhm) duration of  $\sim 30$  fs. These results are comparable to the ones experimentally obtained through wave-breaking in Ref. [81] albeit with a much higher contrast ratio [91]. The origin of the non-uniform

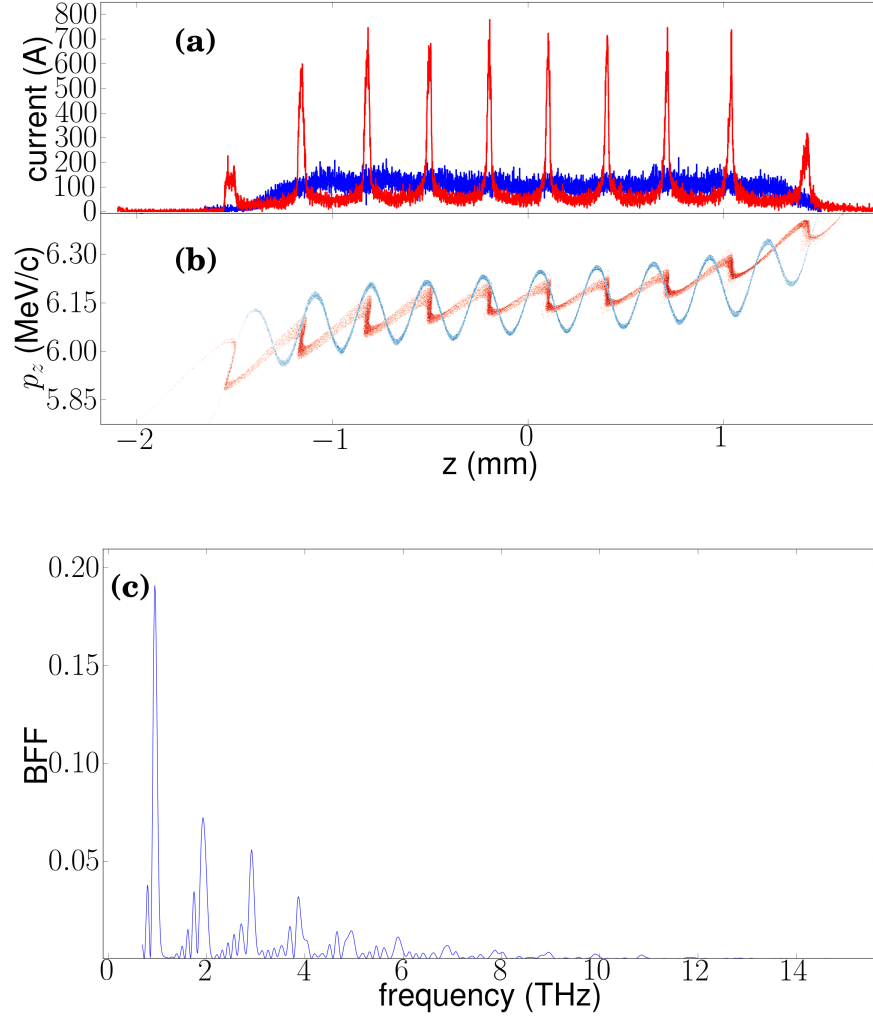


Figure 4.5: Current profiles (a) and associated longitudinal phase spaces (LPS) (b) simulated at the exit of the DLW (blue trace) and at the location of maximum bunching (red trace)  $z = 1.3$  m from the photocathode. Bunch form factor (BFF) (c) obtained at  $z = 1.3$  m from the photocathode. The simulations correspond to the parameters listed under the “S-band” column in Tab. 4.1.

bunching across the beam with peak-to-peak variation in the microbunch current is twofold. First, the slice-energy-spread positional variation along the bunch affects the shortest structure achievable at a given location. And secondly, the LPS prior to the DLW has initial correlations (as seen on the blue density plotted in Fig. 4.5(b)) which affect the bunching uniformity across the microbunches. This latter initial correlation is also responsible for the

apparent “walk-off” feature (the microbunches spread apart from each others as they drift) of the microbunches visible in Fig. 4.4(b). Figure 4.5(c) indicates strong harmonic content at the second and third harmonic frequencies of  $f_1$  – also observed at the location of maximum bunching.

Moreover, the higher harmonics are limited by the precision of the micro-bunch spacing within the bunch; a higher frequency DLW will lead to more micro bunches which will be more limited by the initial correlated LPS. We can investigate this feature by using a lower frequency structure of 500 GHz in the same context of the 1 THz example illustrated above. The current and LPS is shown in Fig. 4.6(a,b) as well as the associated BFF over the frequency range (0.25 THz, 10 THz), as shown in Fig. 4.6(c) for maximum compression (red trace). The very strong higher harmonic content is notably due to larger and more precisely spaced microbunches. Additionally, we may want to suppress higher harmonics or amplify the fundamental; this could easily be done by selecting a bunch which is under or over-compressed such that the micro-bunches span a larger spatial extent; see Fig. 4.6(a,b,c) blue trace.

Finally, the evolution of the transverse beam sizes and emittance is respectively shown in Fig. 4.7(a) and (b) for the case presented in Fig. 4.5. The addition of a second solenoid at  $s \simeq 1.2$  m can transversely focus the beam down to  $\sigma_x = \sigma_y \simeq 45 \mu\text{m}$  at an axial location close to the maximum bunching; see Fig. 4.7(c). The simulated small rms beam size confirms that the one-dimensional BFF approach adopted earlier can accurately be used to estimate the properties of radiation emitted at wavelengths  $\lambda \gg \gamma^{-1}\sigma_{x,y} \sim 5 \mu\text{m}$ . It is therefore applicable to the THz regime. The small transverse size could also permit the use of a second DLW as a narrowband THz radiator as explored in Ref. [92].

The location of maximum bunching depends primarily on the wakefield amplitude compared to the average bunch energy. Operating the RF gun at higher peak fields leads to larger ballistic bunching lengths downstream of the DLW structure and vice versa. Alter-

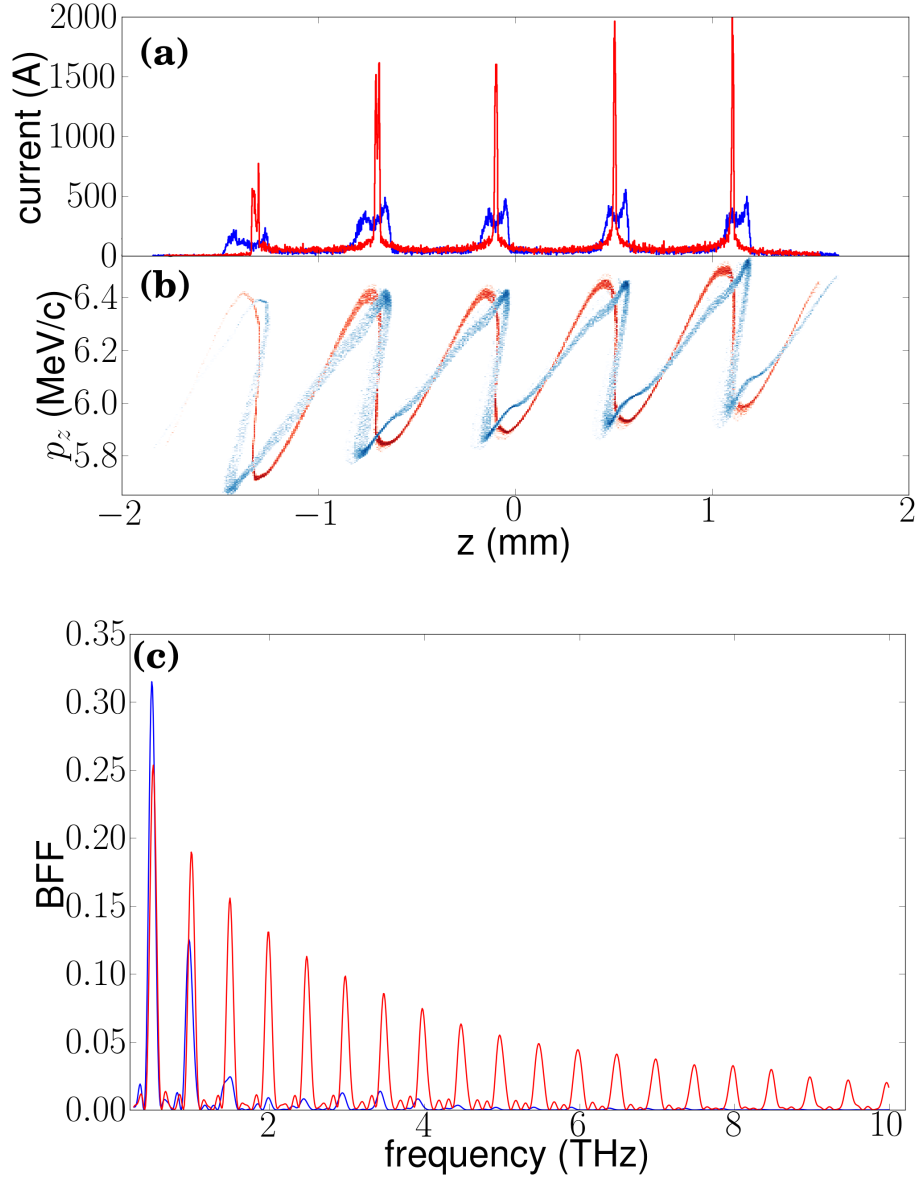


Figure 4.6: Current profiles (a) and associated longitudinal phase spaces (LPS) (b) simulated at maximum compression 31 cm downstream of the DLW (red traces) and at the location of slight over-compression 52 cm downstream of the DLW (blue traces). Bunch form factor (BFF) (c) obtained at the similar locations. The simulations correspond to the parameters listed under the “S-band” column in Tab. 4.1 with the exception of the geometric parameters of the DLW structure selected to be  $a = 350 \mu\text{m}$ , and  $b = 393 \mu\text{m}$ .

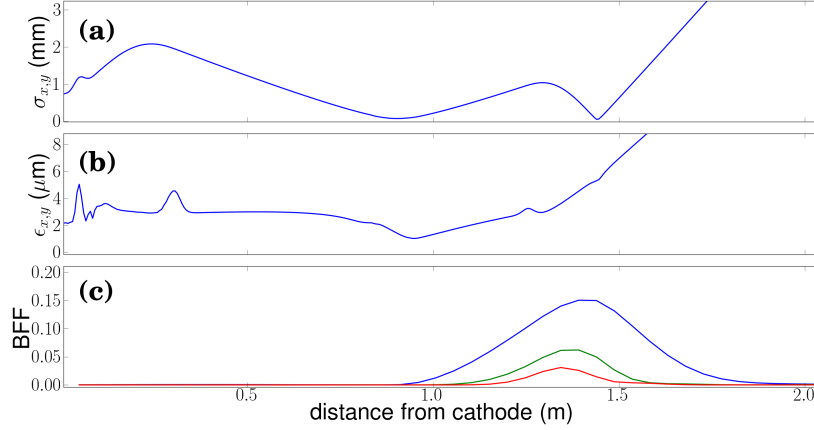


Figure 4.7: Transverse horizontal  $\sigma_x$  and vertical  $\sigma_y$  rms beam sizes (a), corresponding transverse emittances (b) and bunch form factor (BFF) (c) evolution along the beamline. The BFF is evaluated at  $f_1 = 1$  THz (blue trace) and at the second (green trace) and third (red trace) harmonics. The simulations correspond to the parameters listed under the “S-band” column in Tab. 4.1.

natively, shorter bunching lengths can be achieved by decreasing the bunch length at the cost of a lower number of microbunches. To confirm the applicability of our concept to other configurations we carried a similar study as the one presented above for the case of an L-band RF gun.

For this case we consider the setup available at the Fermilab’s A0 photoinjector [93] which incorporates a first-generation L-band gun used at the decommissioned Tesla-test facility at DESY [94]. The gun is nested in three solenoidal lenses. An optimization similar to the one carried for the S-band case was conducted and the resulting operating parameters are displayed in Tab. 4.1 (“L-band” column). For completeness the BFF and longitudinal density evolution downstream of the DLW are shown in Fig. 4.8. As in the S-band case we observe strong bunching at the DLW fundamental mode’s frequency (in this case  $\lambda_1 \simeq 750 \mu\text{m}$  as the DLW parameters are different). But in contrast with the S-band case the higher-harmonic content of the BFF are significantly suppressed. The change in the fundamental frequency

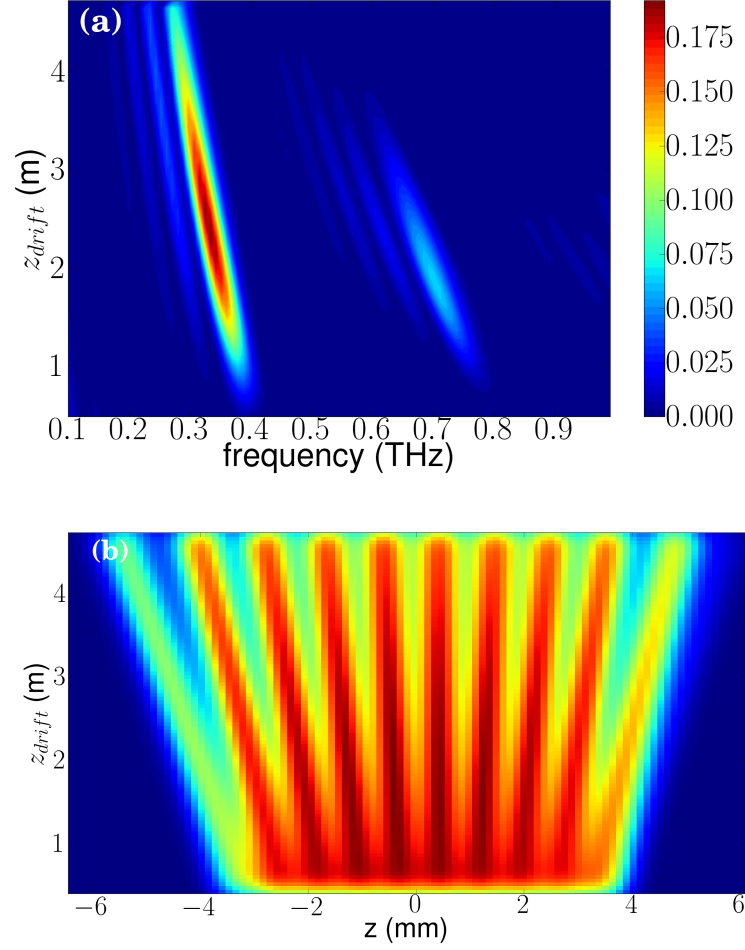


Figure 4.8: Bunch form factor (BFF) (a) and bunch longitudinal density (b) evolution as a function of the drift length referenced with respect to the DLW exit. The simulations correspond to the parameters listed under the “L-band” column in Tab. 4.1.

as the bunch drifts downstream of the DLW appear stronger than for the S-band case and is due to a more prominent “walk-off” effect due to the lower beam energy.



### 4.3.2 Passive Bunching

We now turn to another potential application of the scheme detailed in Section 4.2 to bunch or shape an electron beam produced via photoemission from an RF gun (this corresponds to the case when  $\sigma_z \lesssim \lambda_1$ ). Simply speaking we are interested in maximizing peak currents and charge densities as well as longitudinally tailoring a bunch for various applications (see 5).

To illustrate our point, we first consider the case of the L-band gun just discussed in the previous section and instead of using the DLW parameters of Tab. 4.1, we consider a structure with inner radius  $a = 650 \mu\text{m}$  to produce a global correlated energy spread as the fundamental-mode wavelength of the DLW becomes comparable to the bunch length. As mentioned earlier, the inherent nonlinear LPS distortion exhibits a correlation between the depleted energy location and tail that has the proper sign for compression via ballistic bunching.

We exemplify this possibility by exploring the change in the maximum peak current downstream of a DLW structure with different dielectric thicknesses. The DLW is chosen to have a fixed inner radius  $a = 650 \mu\text{m}$  and the mode's wavelength is varied with different dielectric thicknesses. Although thicker dielectrics generally lead to a larger population of modes, the Gaussian shape employed in this study mostly excites the fundamental. The results appear in Fig. 4.9 and indicate that a peak current on the order of  $\sim 10 \text{ kA}$  is attained when the fundamental-mode wavelength is  $\sim 2.06 \text{ mm}$  (corresponding to  $\sigma_z = 1.01 \text{ mm}$ ). It should be pointed out that the quoted currents are most likely over estimated due the absence of collisional effects in the space-charge algorithm implemented in ASTRA. The latter wavelength corresponds to a structure with outer radius  $b = 855 \mu\text{m}$  (or dielectric thickness

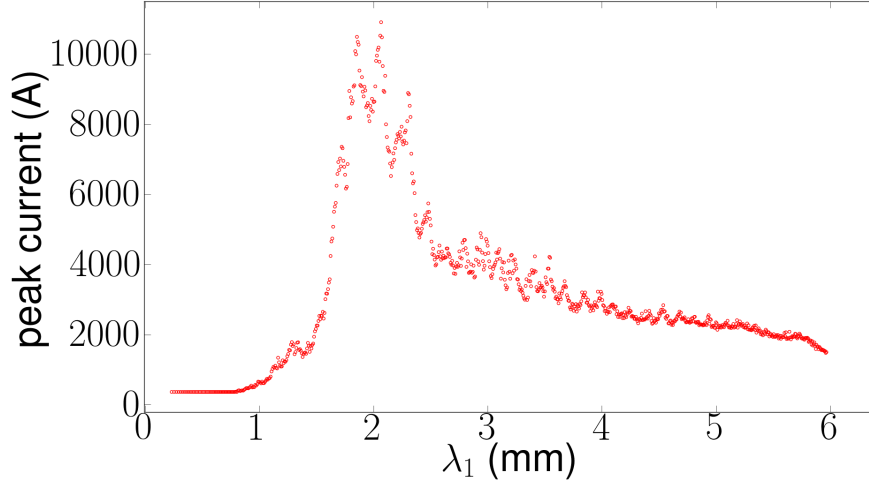


Figure 4.9: Maximum peak current as function of the fundamental-mode wavelength  $\lambda_1$ . The observed noise comes from numerical errors in precisely determining the value of the the axial position where the peak current is maximized. These simulations are carried with the beam parameters summarized in Tab. 4.1 “L-band” column but for a DLW structure with inner radius  $a = 650 \mu\text{m}$ . The fundamental-mode wavelength is varied by changing the structure outer radius  $b$ .

$\tau \equiv b - a = 205 \mu\text{m}$ ). The associated current profiles and LPS appear in Fig. 4.10 and illustrates the role of the initial longitudinal emittance of the bunch before the DLW (i.e. the maximum peak current is achieved for an initial axial slice with smallest slice energy spread). In Fig. 4.10 only 7.1% of the population resides within the current spike while the rest contributes to the formation of longitudinal tails. This low-current population of the bunch could in principle be reduced by exploring some energy-transverse correlations in conjunction with transverse collimators. Also, due to the relatively large inner radii needed to support wavelengths comparable to the bunch length, this technique can in principle easily be scaled to higher bunch charges. Finally, we note that the current profiles shown in Fig. 4.10 can actually find applications, e.g. to investigate wakefield effects in accelerating structures [95] and in compact beam-driven acceleration schemes utilizing low-energy drive

bunches.

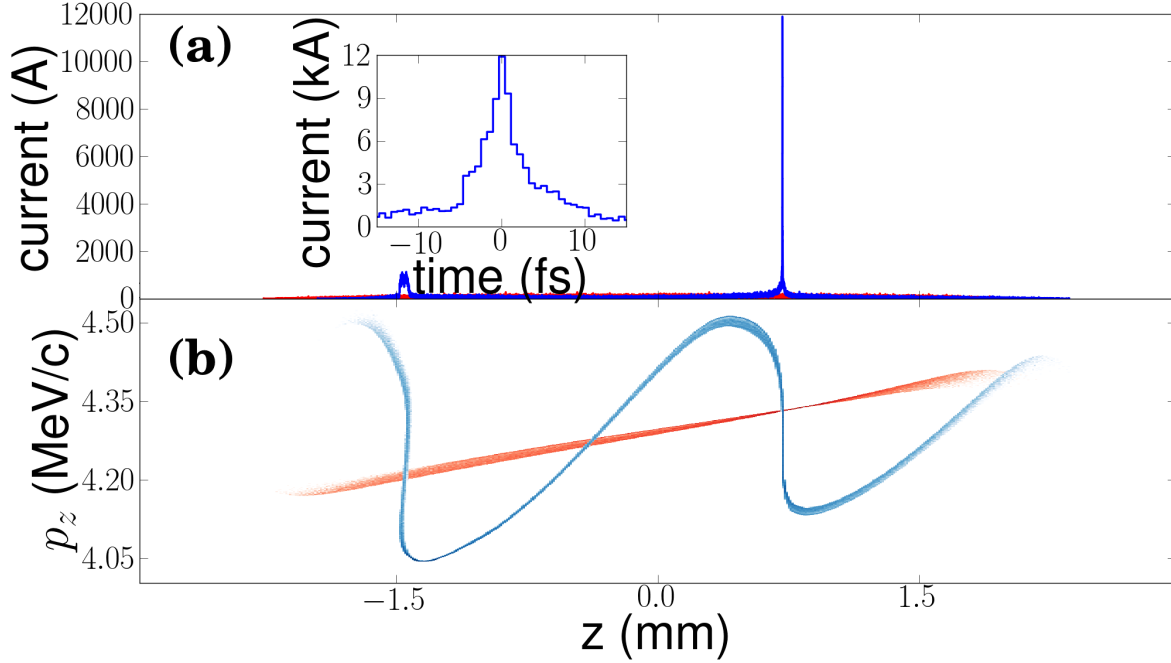


Figure 4.10: Current profiles (a) and longitudinal phase spaces (LPS) (b) at the entrance of the DLW structure (red traces) and at location of maximum compression (blue traces). The simulation correspond to the case  $\lambda = 2.06$  mm in Fig. 4.9. The inset in plot (a) corresponds to a zoom of plot (a) around the  $\sim 12$ -kA peak with its origin of the temporal axis corresponding to  $z = 0.693$  mm in plot (a) axial coordinate. Maximum bunching, in this scenario occurs 43.9 cm downstream of the DLW.

It can sometime be more useful to compress a larger portion of bunch however. As an example, we first consider a Gaussian bunch “tail-bunching,” where  $4\sigma_z \sim \lambda_0/2$ . In this regime, the rear half of the bunch acquires a quasi-linear negative chirp which leads to a compression after a drift of proper length. In Fig. 4.11(left) we present results for a DLW with dimensions  $(a, b) = (1 \text{ mm}, 1.05 \text{ mm})$ , relative dielectric permittivity  $\epsilon_r = 5.7$ , (corresponding to the fundamental-mode wavelength  $\lambda_0 = 0.974$  mm) and length  $L = 5$  cm. Such a configuration leads to  $\sim 50\%$  of the bunch population compressing into 100- $\mu\text{m}$  full-width spike.

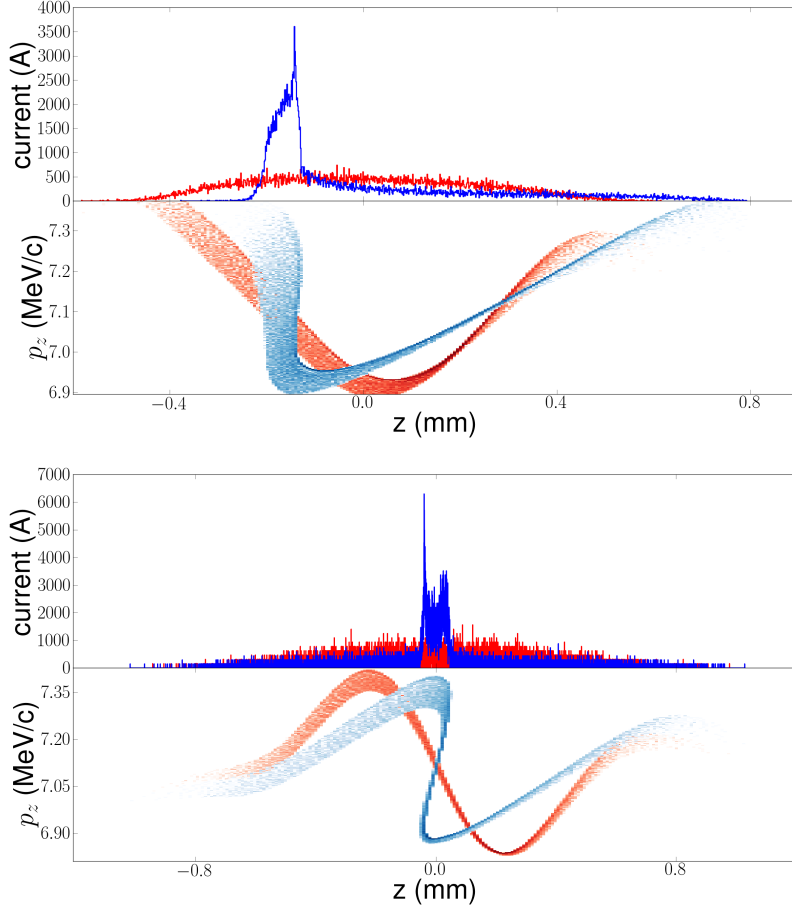


Figure 4.11: Example of bunch-tail (left) and central (right) bunching. For each cases, the current (top) and longitudinal phase space (bottom) are shown immediately downstream of the DLW (red trace), and 1.2 m (left) or 1.13 m (right) downstream of the DLW (blue trace).

Another choice is to modulate the bunch in the regime where  $4\sigma_z = \lambda_0$ , so that the largest concentration of charge (e.g., centrally for a symmetric bunch) is compressed. Again we explore a Gaussian bunch, now with full bunch length  $4\sigma_z \sim 1.7$  mm and a DLW with dimensions  $(a, b) = (0.8 \text{ mm}, 0.85 \text{ mm})$  which leads to  $\lambda_0 = 0.887$  mm. The length of the structure is doubled to  $L = 10$  cm for these simulations. In this simulation, a maximum of 55.8% is found in the 100- $\mu\text{m}$  full-width spike 1.13 m downstream of the DLW; see Fig. 4.11

(right). In principle this technique could also be scaled to longer wavelengths and bunch lengths while increasing the bunch charge.

It should be noted that this technique relies on the non-ultra-relativistic nature of the bunch and that the compressed bunch shapes presented in Fig. 4.11 are achieved at a given axial location and are still evolving. In order to freeze the bunch shape, e.g. for use at higher energy, the beam need to be accelerated and the DLW parameter would need to be optimized to include the effect of downstream acceleration. Finally, a key feature to the bunch compression is the local (or intrinsic) fractional momentum spread. As seen in Fig. 4.11 (red traces in the longitudinal phase space), the slice energy spread depends on the axial slice considered. Therefore, being able to control the slice energy spread at a given axial location (i.e. that matches the zero-crossing in the correlated energy spread imparted by the DLW) could lead to higher peak current containing larger amount of charge.

### 4.3.3 Shaping

As a final application we investigate the possibility of producing low-energy bunches with linearly-ramped current profiles for beam-driven applications. We demonstrate that a standard Gaussian distribution typically produced downstream of an RF gun can be transformed into a ramped bunch with quasi-linear dependency on  $z$ . We take the example of the S-band gun considered in Sec. 4.3.1 and set  $L/\lambda_1 \approx 1/2$  where  $L$  is the full longitudinal size of the bunch upstream of the DLW structure. For these simulations, the axial-field amplitude at the cathode is set to  $E_0 = 140$  MV/m. Such an increase (compared to the set of parameters displayed in Tab. 4.1) was required to mitigate bunch lengthening. Figure 4.12 depicts the LPS evolution and associated current profiles associate to the bunch as it enters (red trace), exits (blue trace) the DLW and after a drift of 0.2 m (green trace). The interplay of the

DLW wakefield and longitudinal-space charge force results in the appearance of nonlinear correlations in the LPS. These nonlinearities provide some control over the current profile.

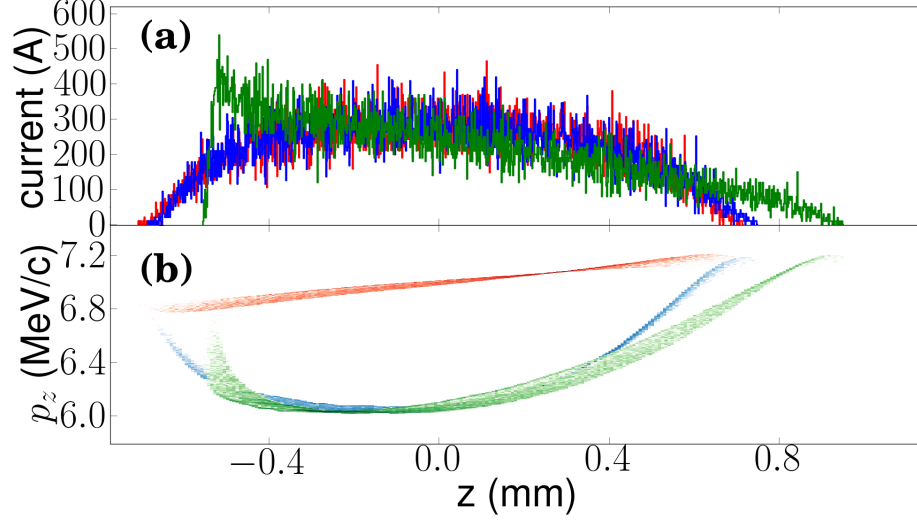


Figure 4.12: Current profiles (a) and longitudinal phase spaces (b) at the entrance (red traces) and exit (red traces) of the DLW structure and 0.2-m downstream of the structure ( $s \simeq 0.54$  m from the photocathode surface) where a quasi-linear current profile is achieved (green traces).

To quantify the performance of the current profile simulated in Fig. 4.12(b, green trace), we compute its wakefield in a DLW with inner and outer radii respectively  $a = 165 \mu\text{m}$ ,  $b = 197 \mu\text{m}$  and the relative dielectric permittivity is kept to  $\varepsilon_r = 5.7$ . The resulting wakefield behind the bunch has a peak accelerating field amplitude of  $E^+ \simeq 60$  MV/m; see Fig. 4.13. The transformer ratio is numerically inferred as  $\mathcal{R} \equiv |E_+/E_-|$  where  $E_- \simeq 8.2$  MV/m is the maximum amplitude of the decelerating electric field within the electron bunch. The achieved transformer ratio of  $\mathcal{R} \simeq 7.3$  is comparable to the ideal ratio of  $\mathcal{R} = n_p \pi \simeq 9.4$  predicted for an ideal linearly-ramped current profile (here  $n_p \simeq 3$  is the number of mode wavelength comprised within the total bunch length) [18]. Depending on the desired application, the photoinjector settings and DLW parameters could be adjusted to produce a ramped current profile after further acceleration in a subsequent linac.

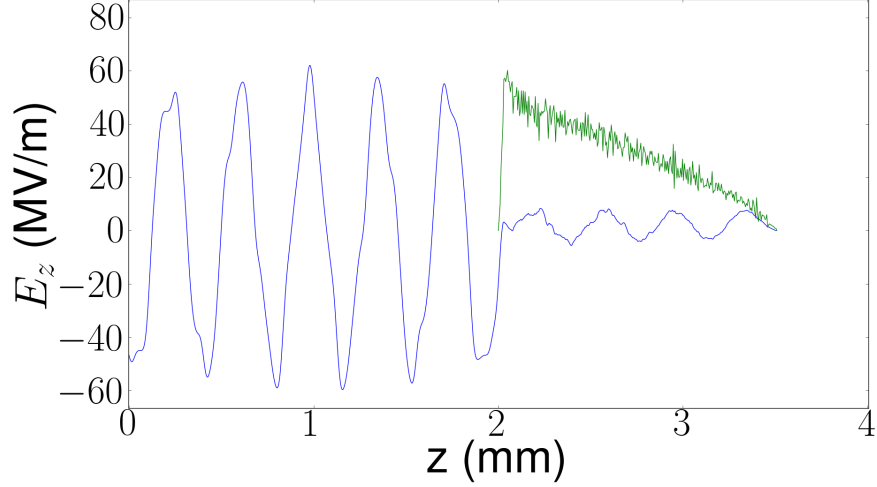


Figure 4.13: Longitudinal wakefield (blue trace) produced behind a bunch with the longitudinal distribution (green trace) identical to the one shown in Fig. 4.12 [plot (a), green trace] for a bunch charge of 1 nC. The structure used for the wakefield generation has the geometric parameters  $a = 165 \mu\text{m}$ ,  $b = 197 \mu\text{m}$  and  $\varepsilon_r = 5.7$ .

Finally, a finer control over the bunch shape could possibly be implemented using several DLW structures with properly selected fundamental-mode wavelengths. Such a multifrequency DLW approach would be an extension of the scheme described in Ref. [96] to higher frequencies.

## 4.4 SUMMARY

In summary, we presented a relatively simple technique to bunch non-ultrarelativistic beams commonly produced by photoinjectors. The method is shown to support the generation of bunch trains consisting of sub-picosecond microbunches. Moreover, we demonstrated that a DLW with a lower-frequency fundamental mode could act as a passive buncher and produce multi-kA bunches. In addition, we discuss the application of the technique to form bunches with linearly-ramped current profiles as needed to improve the transformer ratio in

beam-driven advanced-acceleration techniques. One of the main advantages of the method is that it relies on the bunch interaction with its self-wakefields which are inherently synchronized: the technique is therefore not prone to temporal jitter.

We expect the proposed method to find useful applications that span accelerator-based compact THz-radiation sources, ultra-fast electron diffraction and in photoinjectors for short-wavelength linacs.

It is also worth noting that the scheme could in principle be combined with other electron-emission process (e.g. thermionic- or field-emission) but a detailed exploration is beyond the scope of the present study.

Finally, other wakefield mechanisms, e.g., the use of a corrugated pipe [97, 98] could provide an alternative to DLWs and also lead to similar results [99]. Our selection of a DLW structure was mainly motivated by its manufacturing simplicity and wide use in advanced accelerator R&D.



## CHAPTER 5

### APPLICATIONS

The techniques and schemes proposed in the previous section allows for some interesting avenues to explore for applications ranging from acceleration to longitudinal shaping. In this section we briefly explore more applications, namely the possibility of generating echo enabled harmonic generation (EEHG) with successive DLWs at low energy, and also the possibility of a compact X-ray source based on ballistic bunching and beam-driven acceleration.

#### 5.1 THz via Echo-Enabled Harmonic Generation at Low-energy

Another interesting possibility to explore is echo enabled harmonic generation (EEHG). In the conventional two-stage EEHG technique, an ultra relativistic electron bunch is energy modulated with a laser in an undulator (the laser-undulator system is henceforth referred to as “energy modulator”). The frequency of the modulation corresponds to the laser-undulator resonant wavelength  $f_0^{(1)}$ . The bunch then passes through another chicane to locally over-bunch the beam, thereby producing a stratified longitudinal phase space. The bunch subsequently interacts with a laser in a second energy modulator yielding the superimposition of an energy modulation with frequency  $f_0^{(2)}$ . In the last stage of the process the bunch passes through a chicane with  $R_{56}$  selected to form very short microbunches. The frequency spectrum of the bunch is peaked at frequencies given by  $f_{echo}^{m,n} = mf_0^{(1)} + nf_0^{(2)}$  with  $n, m \in \mathbb{N}$ .

Here we note that a DLW structure with a proper fundamental mode can replace the laser and undulator system in EEHG configuration albeit at the price of longer modulation wavelength. We continue considering the setup described in this chapter and take the case of a non ultra-relativistic bunch. In such a case, a drift space with proper length between the modulators plays the same roles as the chicane in the conventional EEHG. We note that the idea of using an EEHG scheme to micro bunch non-relativistic beams was recently proposed in high-power W-band sources [100].

Considering the same configuration studied in the previous section, the  $\sim 5$  MeV bunch produced by the RF gun is injected in two successive DLW structures. We choose the fundamental frequencies of the first and second DLWs to be respectively  $f_0^{(1)} = 0.6$  and  $f_0^{(2)} = 0.4$  THz. This choice corresponds to the parameters  $(a, b, \epsilon, L) = (0.4 \text{ mm}, 0.43 \text{ mm}, 5.7, 10 \text{ cm})$  and  $(a, b, \epsilon, L) = (0.5 \text{ mm}, 0.55 \text{ mm}, 5.7, 5 \text{ cm})$  for the first and second DLW structures, respectively. The resulting longitudinal phase spaces and current densities are shown in Fig. 5.1 and demonstrate the capability of the system to support a EEHG-like harmonic bunching scheme.

The quality of the bunching can be further quantified by introducing the bunch form factor (BFF) defined as  $\tilde{F}(\omega) = N^{-2} |\sum_{k=1}^N e^{-i\omega z_k/c}|^2$  where the summation is carried over the number of macro particles  $N$ . The evolution of  $\tilde{F}(\omega)$  as a function of the distance from the exit of the second DLW is shown in Fig. 5.2 for the same case as the one presented in Fig. 5.1. The BFF is enhanced at  $f_0^{(2)}$  and its second harmonic at 0.8 THz. In addition we observe peaks at “echo” harmonics appearing as “islands” located at 1, 1.4, and 1.8 THz in Fig. 5.2. These frequencies are given from the “echo” unconverted frequency  $f_{echo}^{m,n} = m f_0^{(1)} + n f_0^{(2)}$  with  $m = 1$  and  $n = 1, 2, 3$  respectively.

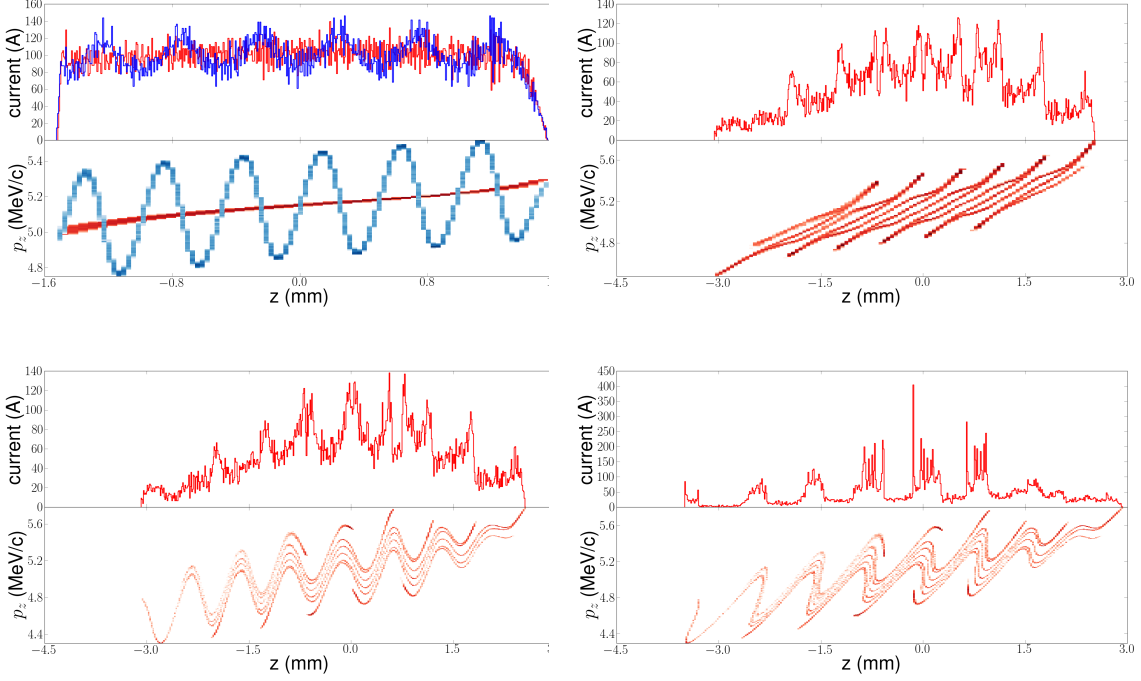


Figure 5.1: Generation of EEHG with two DLWs: A plateau distribution is shown immediately before (red trace) and after (blue trace) passing through a DLW with  $f_0^{(1)} = 0.6$  THz (top left). A snapshot of the bunch after a 1.6 m drift (top right) before entering the second DLW with  $f_0^{(2)} = 0.4$  THz. Finally, the bunch is shown immediately after the second DLW (lower left), and after a 25 cm drift (lower right). In each figure the longitudinal phase space and current distributions are shown (as lower and upper sub-plots respectively).

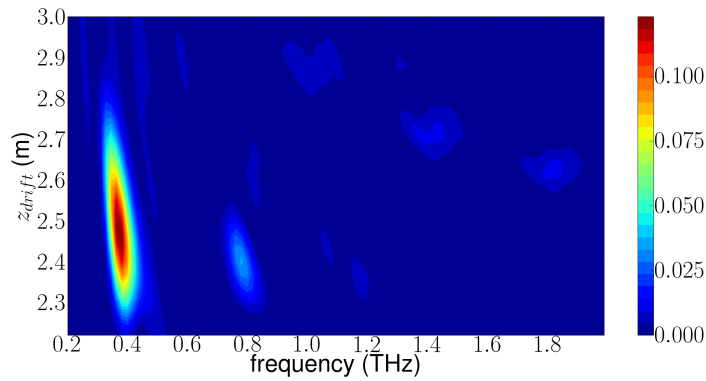


Figure 5.2: BFF evolution downstream of the second DLW for the same configuration as presented in Fig. 5.1.

## 5.2 Compact X-ray source

Modern accelerator-based X-ray sources have led to a wave of scientific advancements in various fields. Their inception relies primarily on energetic electrons which are manipulated to radiate either via undulators or inverse Compton scattering (ICS). In both radiation mechanisms the photon energy  $\mathcal{O}(\gamma^2)$ , therefore an increase in the beam energy is significant. Recently, compact X-ray sources based on X-band RF technology has been proposed [101]. Likewise an X-ray source utilizing laser-plasma wakefield accelerator have been demonstrated [102]. Finally, most recently the possible use of a THz pulse to accelerate electron bunches have been put forward [103] and tested [104]. These solutions, although appealing, are either costly (X-band technology) and/or require the use of high-power lasers currently operating at low repetition rates.

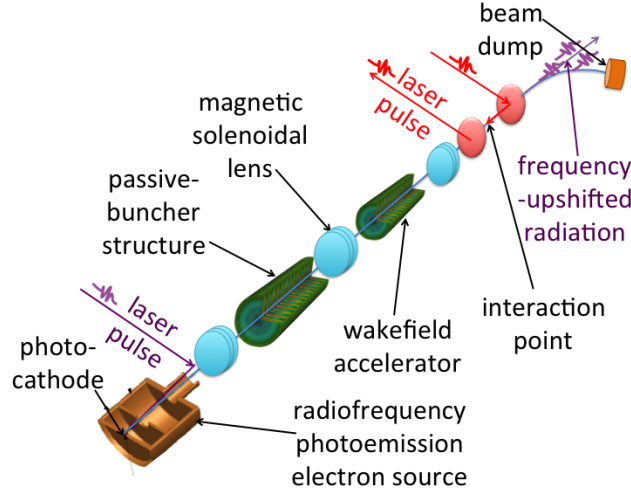


Figure 5.3: Overview of the compact source scheme: a photoinjected electron bunch passes through a series of DLWs for cascaded acceleration, the resulting high energy electrons are used with a laser to generate inverse Compton scattering.

Two practical challenges emerge for beam-driven acceleration at low energy. First, the geometric emittance associated to a low-energy photoinjected electron bunch sets an upper limit on the inner radius  $a$  and length  $L$  of the DLW structure. Second, the scheme relies on the production of a high-peak-current electron bunch along with the formation of a witness bunch.

To address some of these challenges, we propose an accelerator setup diagrammed in Fig. 5.3 based on a "cascaded acceleration" scheme. A high-quality electron bunch is produced in an RF gun and focused into a DLW structure (DLW1). The structure passively bunches the beam which can then be used to drive a large gradient wakefield in a second DLW structure (DLW2).

### 5.3 Cascaded Acceleration

Let us now consider the use of two DLWs in series to accelerate a low energy (e.g.  $< 10$  MeV) electron bunch. In this scheme, the first DLW is used to impart an energy modulation which leads to ballistic bunching as discussed in Ref. [105]. In this section we carry simulation of the beam dynamics considering the LCLS S-band gun operating with a peak surface field on the photocathode of 140 MV/m. Table 5.1 summarizes the accelerator settings employed. The large peak field helps preserve high-charge densities (especially peak current) which eventually results in higher transformer ratios. Our studies focus on the case of 2-nC bunch charge and it is important to note that this technique is very scalable to larger charges and wavelengths. The simulation was carried with ASTRA which is described in 2. The Green's functions used in the wakefield calculations are computed using the six lower-frequency modes supported by the DLWs following the methodology of Ref. [6].

Table 5.1: Accelerator beamline settings and DLW parameters used in the ASTRA simulations. The relative modes amplitude are normalized to the square sum of the amplitudes.

parameter	value	units
laser pulse RMS duration	2	ps
laser RMS spot size	1.3	mm
initial charge	2	nC
peak field on cathode	140	MV/m
average energy	7.01	MeV
<b>DLW1 parameters:</b>		
relative permittivity	5.7	—
position	0.6	m
length	10	cm
inner radius	0.8	mm
outer radius	1	mm
mode wavelengths	2.19, 0.72, 0.41	mm
relative mode amplitudes	1, 0.51, 0.23	—
<b>DLW2 parameters:</b>		
relative permittivity	5.7	—
position	1.7	m
length	8	cm
inner radius	0.5	mm
outer radius	0.55	mm
mode wavelengths	0.74, 0.19, 0.11	mm
relative mode amplitudes	1, 0.23, 0.07	—

### 5.3.1 Ballistic bunching using a DLW

A critical component to high-gradient wakefield acceleration is the requirement for a high-peak-current bunch. The needed currents are typically one order of magnitude larger than those typically produced downstream of an RF gun. Several bunching techniques could be employed but given our requirement for compactness and limited use of external power, we use a passive ballistic bunching method based on a DLW structure as investigated in Ref. [24]. The parameters of the first structure (see DLW1 in Tab. 5.1 are chosen to ensure the

relative amplitude of the first three modes are significant  $> 0.1$  and the fundamental-mode wavelength (2.19 mm) approximately corresponds to the total bunch length. Additionally, the radius of the aperture (1 mm) is large enough to allow for the electron beam to be fully transmitted. This wavelength choice together with the presence of significant higher-order mode confer to the longitudinal phase space a square-waveform; see Fig. 5.4. During a

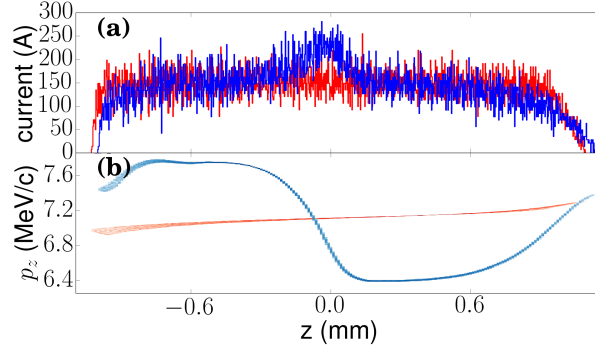


Figure 5.4: Longitudinal phase spaces (b) and current projection (a) before (red) and after (blue) DLW1 (with parameters listed in Tab. 5.1). The tail of the bunch corresponds to  $z < 0$ .

subsequent drift where ballistic bunching is at play, the center of the bunch will be compressed while the head and tail of the bunch will experience minor longitudinal displacements. The current profile immediately downstream of the DLW already shows sign of this "differential" compression: its center population has its peak current enhanced from  $\sim 150$  to  $\sim 250$  A; see current profiles in Fig. 5.4.

### 5.3.2 Acceleration with compressed bunch

Downstream of DLW1, the ballistic bunching occurs over a free-space drift of 1.1 m. The optimum locations and parameters of the following structure (DLW2) was empirically optimized to maximize the final energy of accelerated electrons in the tail. Finally, it should be noted that the evolution of the longitudinal phase space generates current profiles with

complicated shaped which can be used in combination with multi-mode DLW structures to support higher transformer ratios. This ultimately increases the maximum beam energy which can be transferred from the bunch center to its tail.

Given the large parameter space constrained by these dynamical processes, we only present one optimal case devise via empirical optimizations. A more comprehensive study would undoubtedly lead to higher performances and will be carried with the help of a genetic optimizer. Our trial-and-error approach consisted in varying the structure parameter and its location, compute the produce wakefield and parameters that maximize the transformer ratio. An example of generated current profile (green trace) and associated wakefield (blue trace) appear in Fig. 5.5. The transformer ratio  $\mathcal{R} \simeq 2.8$  is modest but the peak accelerating field experienced by electrons in the bunch-tail are on the order of 100 MV/m. The structure

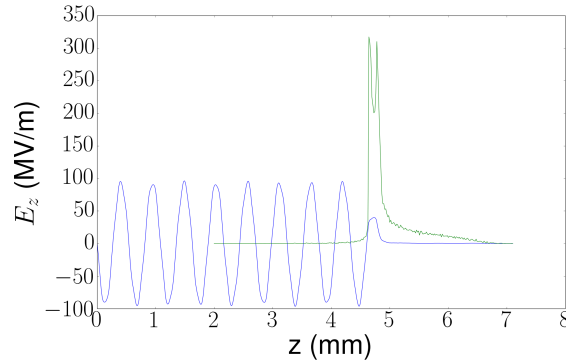


Figure 5.5: Longitudinal wake generated at the location of the second DLW (blue trace) from corresponding current (green trace). The tail of the bunch corresponds to  $z < 0$ .

parameters are gathered in Tab. 5.1. Compared to DLW1, DLW2 radius is twice as small and the dielectric-liner thickness is 50  $\mu\text{m}$  resulting in a fundamental mode with wavelength  $\sim 3$  times smaller. The small wavelength produces a modulated longitudinal phase space; see Fig. 5.6 (b). The modulation amplitude is comparable to the beam energy and results in highly nonlinear phase space distortions. The maximum energy reached by the electron in the tail is in excess of 12 MeV while the decelerated electrons have energies down to



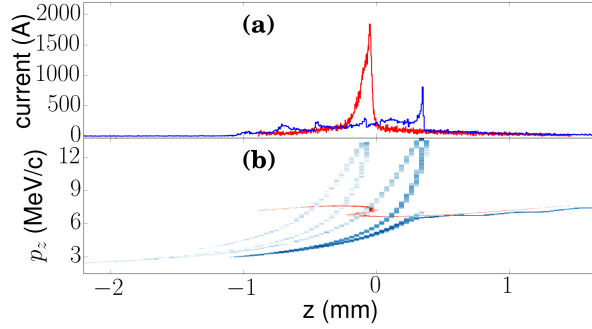


Figure 5.6: Longitudinal phase space (b) and current projection (a) of before (red) and after (blue) cascaded acceleration. The tail of the bunch corresponds to  $z < 0$ .

$\sim 3$  MeV. Other results showed larger final energies with correspondingly small decelerated-electron energies where dynamical wakefield effects would occur; a self-consistent particle tracking code would be necessary to investigate the properties of the bunch as it becomes non-relativistic.

### 5.3.3 Selection of accelerated population

Compared to a conventional drive-witness bunch, the scheme described in this section uses part of the drive bunch to accelerate its trailing population rendering the final step of extracting the accelerated beam more intricate. Here we mentioned to possible selection processes. A first approach consists in placing a small dispersive section downstream of the DLW2 combined with a collimator. A second approach makes use of chromatic effects to differentially focus the accelerated population and defocus the rest of the beam. Both approaches are under consideration and their compatibility with high-repetition-rate operation needs to be fully assessed.

## 5.4 Experimental investigation of THz-pulse propagation in a slab-symmetric dielectric structure

Throughout this dissertation we have discussed beam-driven approaches to drive large electromagnetic wakes in DLWs at the THz-scale. The recent development of semi-efficient (1%) laser-based THz sources (100-700 GHz) however, has opened the door to the development of THz-driven linacs [106, 107, 108, 109]. In this scheme, a radially-polarized THz pulse is co-propagated with an electron bunch in a dielectric-lined waveguide (DLW) with optimized geometry; THz pulses with mJ energies can support accelerating fields on the order of GV/m. The THz-pulse is also matched to the structure thereby mitigating possible excitation of spurious modes (e.g. dipole modes often excited in beam-driven schemes dielectric-wakefield acceleration [110]).

In this section we cover the development of a compact laser-based THz source at the A0 photoinjector laser room. The THz generation scheme is based a tilted-wavefront approach at room temperature. The goal was to characterize a slab-symmetric DLW using electro-optic sampling.

### 5.4.1 Simulation and Analysis of a THz pulse propagation in a SLAB DLW

To assess the performance of the described experimental setup we modeled the propagation of a THz pulse through the DLW and use these numerical results to develop analysis tools. It is useful to investigate the dispersion relations of the structure as well, as described in 2; see Fig.5.7. The simulation of a THz pulse through the DLW were performed using

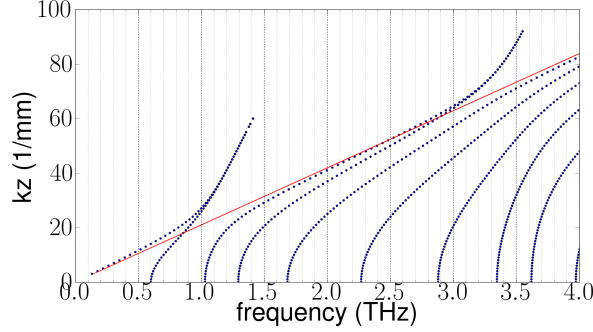


Figure 5.7: Dispersion relation associated to the LSM modes in a slab-symmetric DLW with parameter  $a = 100 \mu m$  and  $b = 120 \mu m$ . The red diagonal line correspond to  $k_z = \omega c$ .

the program VORPAL. VORPAL uses the conformal finite difference time domain (CFDTD) method to solve Maxwell's equations. The geometry of the problem simulated with VORPAL appears in Fig. 5.8.

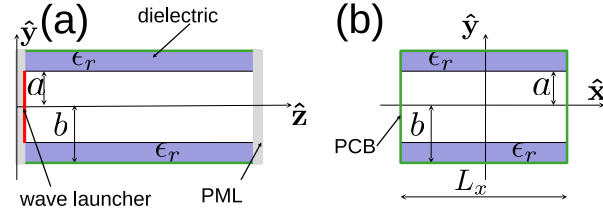


Figure 5.8: A diagram of the slab from the x-transverse direction (a) and the from the z-longitudinal direction (b). The slab is composed of a dielectric coating with dielectric permittivity  $\epsilon_r$  surrounded by a perfectly conductive boundary (PCB). In the VORPAL simulation, we inject the THz pulse using a current  $\vec{J}$  to drive a short pulse in  $z$ . Lastly, to remove reflections and to artificially produce the pulse leaving the structure we implement a perfectly matched layer (PML). We record the signal on axis, near the PML.

A THz pulse is launched on the first  $x=0$  grid plane:  $(0:N_X, 0:N_Y, 0:N_Z=1)$  with current:  $\vec{J}_z = A_0 t \sin(2\pi f_1 t) \sin(2\pi f_2 t) \sin(2\pi f_3 t) \exp(-(t - TPEAK)^2 / (FWHM^2))$ . The driven frequencies correspond to  $(f_1, f_2, f_3) = (0.8, 1.0, 1.2) THz$ ,  $TPEAK = 2$  ps, and  $FWHM = 1$  ps. Although the pulse peaks in frequency-intensity near the driven  $f_n$ , its shortness in time also helps excite higher frequencies and modes. The electromagnetic field of the guided pulse are recorded on a two-dimensional grid-line as a function of time at the entrance

$E_u(x, y = 80 \mu m, z = 0, t)$  and at the exit  $E_u(x, y = 80 \mu m, z = 2 \text{ cm}, t)$  (where  $u \in [x, y, z]$  corresponds to the three field components).

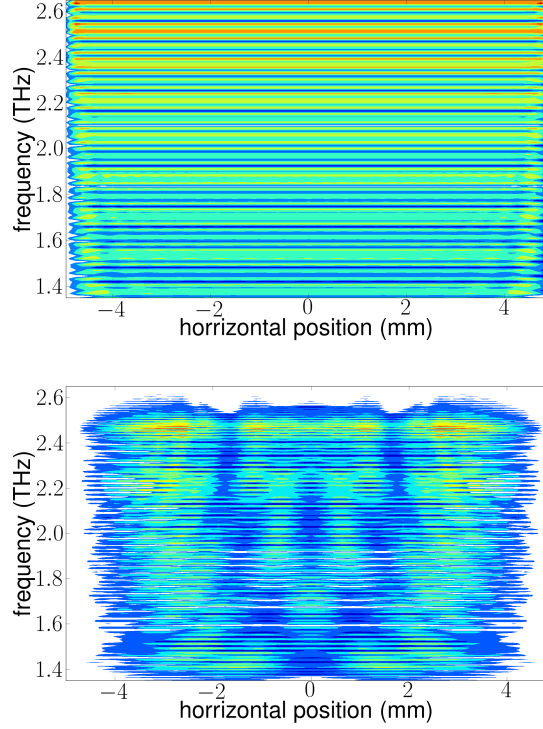


Figure 5.9: Fourier transform of the pulse at the entrance of the structure  $|E_y(x = 0, y = 80 \mu m, z = 0, f)|$  (top) and a Fourier transform of the pulse at the end of the structure  $|E_y(x = 0, y = 80 \mu m, z = 2 \text{ cm}, f)|$  (bottom).

The fourier transform of the pulse before and after propagating through the structure gives us a partial understanding of the propagation of the modes through the structure. The surviving frequencies correspond to the eigenmodes of the structure. And the frequencies which have faded correspond to the evanescent decay of non-eigenmodes through the structure.

Fig. 5.9 shows the Fourier transform of the  $+\hat{y}$  component at the entrance and exit of the structure. The varying horizontal frequency content of the pulses is due to the difference in the mode's spatial distributions.

Moreover, the slopes of the modes in Fig. 5.7 correspond to the respective mode's group velocity for a particular frequency. If we assume all of the modes are driven simultaneously at  $t=0$ , we can deduce the temporal spacing of the modes at the end of the structure.

We import the signal recorded at the end of the structure into another program for temporal-spatial analysis. For each gridpoint recorded on the transverse line at the exit of the structure, we use a moving window to scan through the signal temporally. At each window step, we perform a Fourier transform and plot the coefficient strength of the frequency of interest. To reduce any unwanted artifacts from sharp edges in the Fourier transforms, we apply a Hann window defined via:  $w(n) = 0.5 \left(1 - \cos\left(\frac{2\pi n}{N-1}\right)\right)$  for an individual point  $n$ , of  $N$  sampled points.

In Fig. 5.10 we show results for the 1.4 and 1.8 THz components of the frequency-time maps after passing through the slab structure. Using this method, and comparing to the dispersion curve above, we can confirm the propagation of the  $\text{LSM}_{2m}$  and  $\text{LSM}_{3m}$  for the 1.4 THz component as well as the propagation of the  $\text{LSM}_{2m}$ ,  $\text{LSM}_{3m}$ , and the near cutoff region of the  $\text{LSM}_{4m}$  which explains its tardiness passing through the structure.

## 5.5 Experimental setup

We use a broadband  $\delta\lambda \simeq 100$  nm Ti:Saph commercial laser system centered at 800 nm. The “Octavius” oscillator is pumped with 532 nm  $\sim 5$  W CW laser and is modelocked to 81.25 MHz which is the 16th subharmonic of the 1.3 GHz master oscillator at the A0 photoinjector. The laser passes through a “Dazzler” phase-shaper which is useful for controlling the chirp and broadband width for the amplifier. The laser is then regeneratively amplified over  $\sim 7$  passes to  $\sim 4$  mJ before being released via a voltage controlled switch (i.e. Pockels cell); see Fig. 5.11 for a schematic of the A0 laser lab.

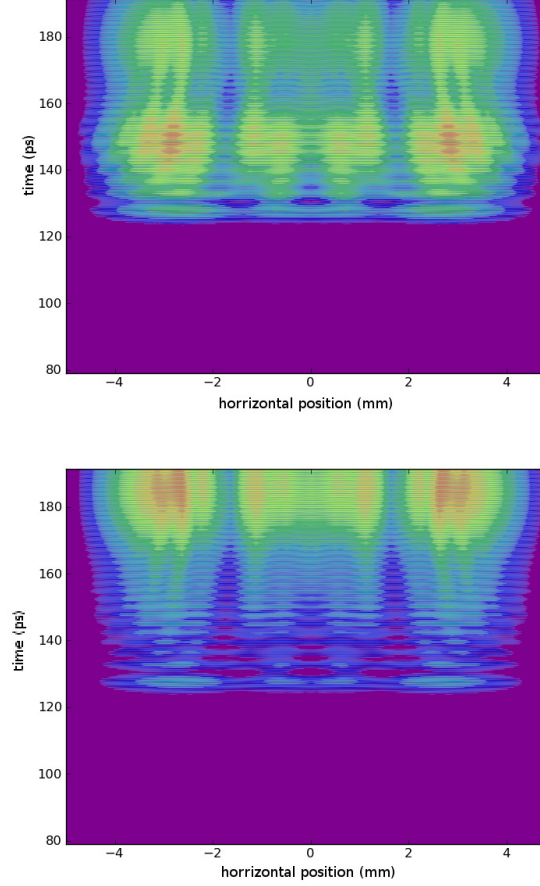
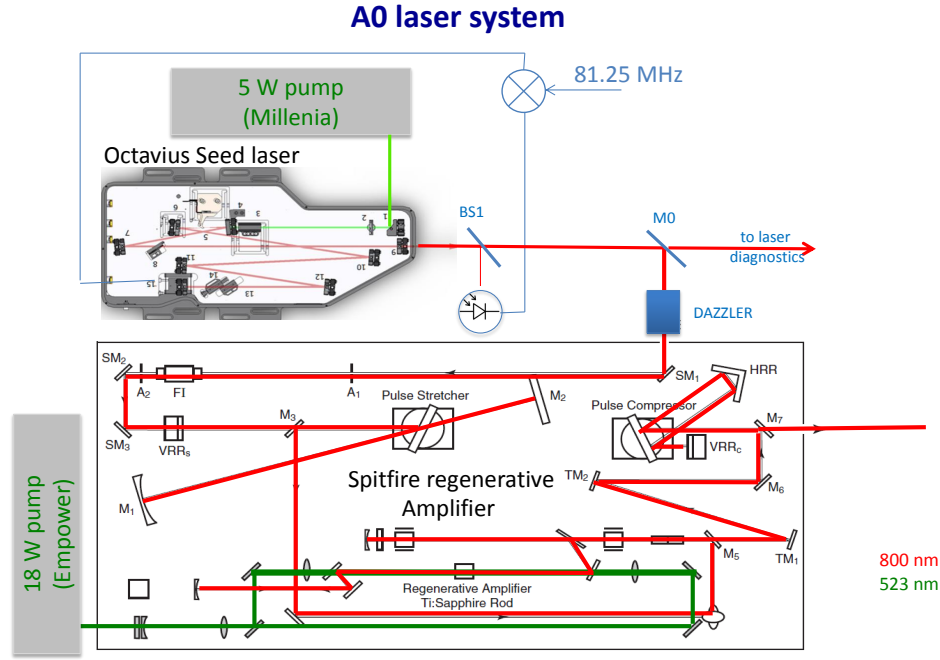


Figure 5.10: Frequency-time maps for the 1.4 THz (top) and 1.6 THz (bottom) components of the signal transmitted through the structure.

For THz generation we use a phase-matched optical rectification approach using the tilted-wavefront approach with a wedged crystal [106, 111]. Due to the large dispersion from the grating with our broadband laser, we use a telescope to reduce the initial beam size by a factor of  $\sim 2$ . We then use a beam splitter to send 5% of the beam through a delay line. The remaining majority of the laser beam impinges on a holographic grating with 1800 lines/mm to generate an initial tilt; we operate the grating near its blaze angle to maximize efficiency. The diffracted beam is relayed through a combination of cylindrical and spherical lenses which control the final spot size and tilt-angle into a stoichiometric  $\text{MgO}(0.6\%)\text{:LiNbO}_3$



1

Figure 5.11: Schematic of the A0 laser system. A Ti:Saph “Octavius” laser oscillator outputs 81.25 MHz 150 fs pulses and is regenerative amplified to  $\sim 4$  mJ per pulse. The amplified laser is used to generate photoelectrons and also in our laser-based THz-generation scheme.

crystal with dimensions  $5 \times 5 \times 9.81$  mm. The THz is then transported through a 4-F system designed to allow an insertable target (e.g. DLW). The THz and probe beam are finally recombined into an electro optic (EO) crystal which is sensitive to the electric field of the THz pulse (see Fig. 5.12); when the two beams arrive simultaneously in the EO crystal, the electric field can be mapped into a polarization rotation of the probe beam. Finally, the use of a polarizer to reject the original polarization of the probe beam can be used to convert the polarization rotation into an intensity modulation on an e.g. diode. The two beams were first temporally aligned using a fast scope with a fast diode; the probe beam and IR leaking from the THz-crystal were placed on the diode and a polarizer was used to make both signals have similar amplitude. When we were satisfied with the temporal alignment of the beams on the scope, we placed a thin polyethylene IR filter after the THz generation; the filter does

not reduce the amplitude of the THz pulse but does delay it. Knowing the direction of delay, the probe pulse was then accordingly scanned with a delay stage to finally recover the EO signal. We note we did not use balanced detection and therefore our results below may not represent the true waveform [112]. The experiment was operated at 1 Hz to reduce jitter; this stems from the A0 photoinjector system which follows a 1 Hz repetition rate, and Servo controller was used to phase lock the laser system with the diode trigger. The diode signal was sent to a digitizer which was accessible to the A0 control room computers, the delay stage was also operated from the control room computers to make data taking relatively simple. A slab-symmetric DLW with dimensions  $2 \times 1$  cm with  $20 \mu\text{m}$  thickness was placed at the interaction point; its aperture was controllable with a manual stage.

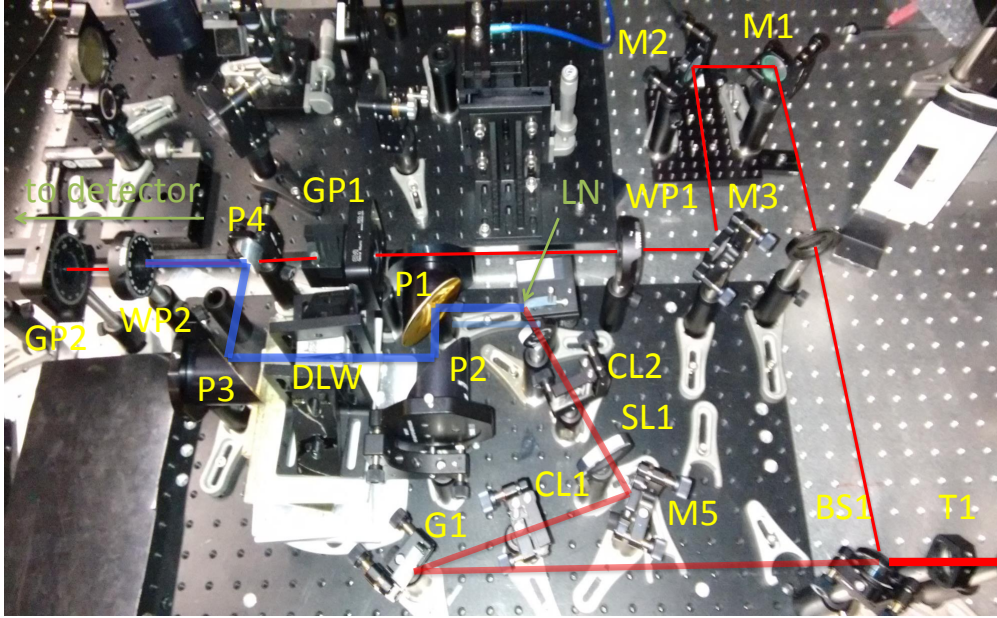


Figure 5.12: Experimental setup; an 800 nm laser comes from the right onto a beam splitter; 95% is used for the tilted wavefront THz generation; the rest of the beam passes through a delay stage before being recombined for EO detection.



## 5.6 Preliminary experimental results

The first result stems from the temporal alignment of the probe and THz pulse into the EO crystal. The autocorrelation of the two pulses through the crystal converts the electric field of the THz pulse into an intensity modulation as a function of delay; see Fig. 5.13.

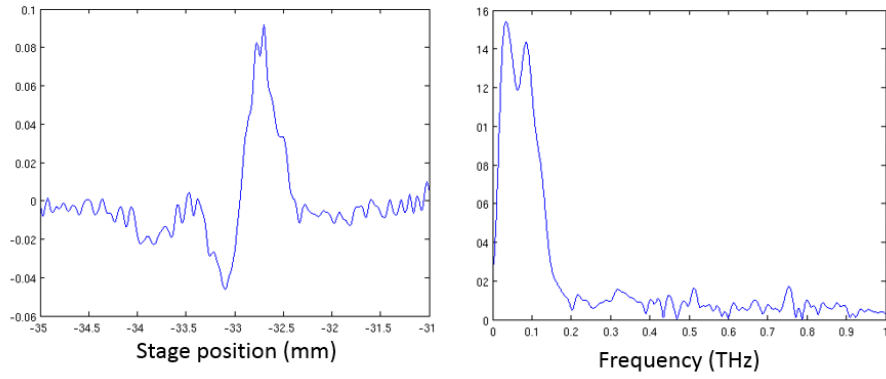


Figure 5.13: Data of the unbalanced EO detection (left) and its corresponding spectrum (right).

Next we investigated the dispersion in a slab-symmetric structure with different apertures. We present experimental results for inner gaps of 1.5 mm and 2 mm in Fig. 5.14; the results indicate that the smaller aperture sizes lead to slower group velocities in the structure. A difficulty of this scheme is the difference of the THz-beam path with and without the DLW structure present; this ultimately leads to the smaller amplitude signal for EO detection.

## 5.7 THz-based electron gun

Although conventional electron sources are often used to investigate the performance of advanced acceleration concepts [113], their adaptation to serve as an injector for an optimized advanced accelerator remains challenging. Instead several groups have developed short-pulse

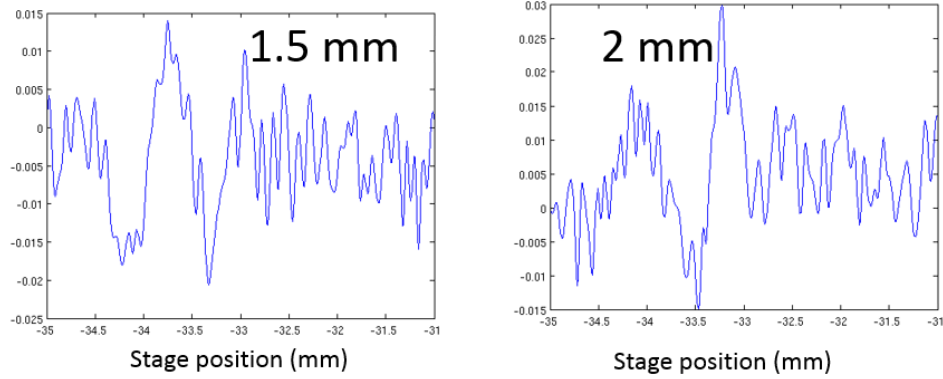


Figure 5.14: Unbalanced EO signal as a function of probe delay in mm. We show two inner gap results of 1.5 mm and 2 mm where there is noticeable slower group velocity in the smaller structure.

electron sources, e.g., based on dielectric grating [114], free-space THz streaking [115, 116], or the proposed optically driven dielectric-waveguide sources [117]. Unfortunately, electron sources using an optical wave are typically limited in the charge they can produce since space charge is predominant at low energy and needs to be mitigated. For instance at  $\lambda_{acc} = 800$  nm, a typical bunch length of a few nm would be required which would result in peak current,  $Qc/(2\pi\lambda_{acc}) \geq 6$  kA for a 1 pC bunch charge (here  $c$  is the light velocity). Alternatively, using a THz pulse with  $\lambda_{acc}=100$   $\mu\text{m}$  would result in a peak current on the order of 50 A (taking  $\sigma_z \simeq 10^{-2}\lambda_{acc} \simeq 1$   $\mu\text{m}$ ). The latter value is consistent with values typically achieved in conventional photoinjectors, see Ref. [118] for example. Likewise, the trade-off between electron bunch length and charge could enable the production of higher charge (up to 100 pC) in exchange for longer bunches.

A conceptual schematic of this low-energy electron source, henceforth dubbed “THz-gun”, appears in Fig. 5.15: two thin dielectric surfaces deposited on a metallic substrate (or free-standing with metalized outer surfaces) are faced to each other. The vacuum gap  $g(z)$  between the surfaces is a function of the axial position  $z$  (coincident with the direction of propagation of the electron bunch).

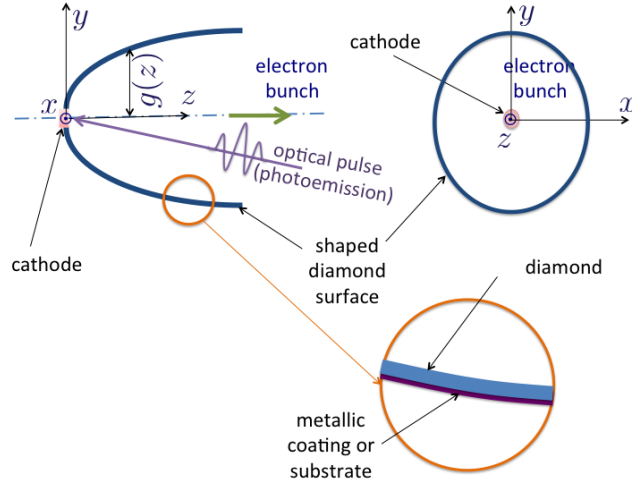


Figure 5.15: Section, top view and side view (respectively on top, bottom left and top right) of the proposed “THz gun” electron source.

The function  $g(z)$  is tailored to insure the phase velocity of the injected THz wave matches the electron beam’s velocity thereby resulting in a quasi-monotonic energy transfer from the THz wave to the electron bunch. Ideally, the phase slippage between the wave and beam can be suppressed. In this paper we focus on a slab DLW as its tapering is practically easier to realize.

### 5.7.1 Dispersion Controlled Acceleration

A very real problem with low-energy acceleration is phase slippage—where a mismatch between the accelerating phase of the electromagnetic wave and electron bunch velocities lead to poor energy gains. This problem can be mitigated by using large accelerating gradients with relatively long electromagnetic wavelengths like photoinjectors, where electron bunches typically sample a small portion of the wavelength. Considering the high frequencies of the THz regime, a correspondingly powerful driving pulse would be necessary appropriately scale the conventional photoinjector scheme which may be difficult.

Let us imagine an alternative: developing a longitudinally-asymmetric structure whose dispersion relations will lead to phase and group velocities that will match the velocity of an accelerating electron bunch. To give primitive insight into this possibility, we consider a the dispersion relations for the LSM modes detailed in 2.

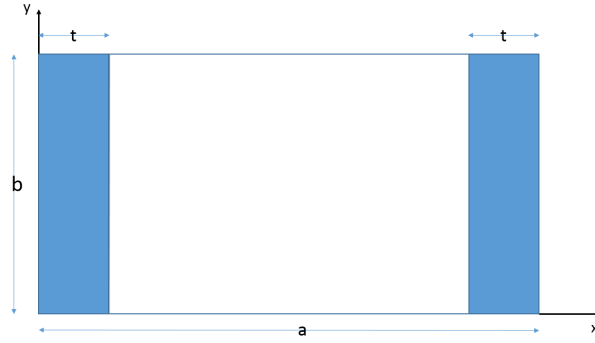


Figure 5.16: A transverse view of a dielectric loaded waveguide (DLW).

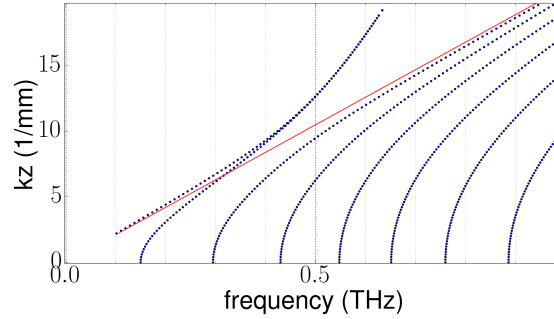


Figure 5.17: A transverse view of a dielectric loaded waveguide (DLW).

The equation of motion for an accelerating charge is given by

$$z(t) = \frac{1}{qE} \sqrt{(cqEt)^2 + E_0^2}, \quad (5.1)$$

here  $q$  is the charge,  $E$  is the electric field magnitude, and  $E_0$  is the initial starting energy (including rest mass).

Next we numerically explore the range of the fundamental accelerating mode ( $\text{LSM}_{11}$ ) over the range  $k_z = \omega / (\dot{z}(t))$  of one accelerating electron and look for solutions as a function of inner radius. To do this we need to hold constant several parameters (see Tab. 5.2).

Table 5.2: Parameters associated to single and multi-mode structure for central-bunching.

Parameter	value	Units
electric field (E)	100	MV/m
frequency (f)	300	GHz
thickness (t)	30	$\mu\text{m}$
open gap (b)	1	cm
relative permittivity	5.7	—

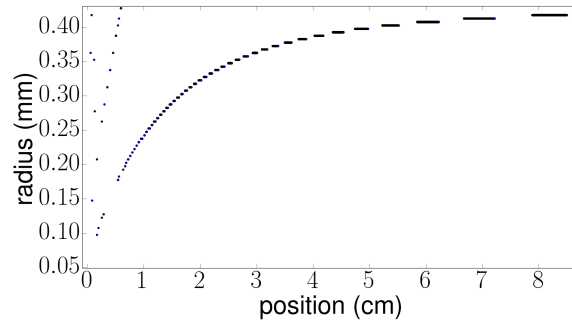


Figure 5.18: The inner radius of the structure shown as a function of longitudinal coordinate for the numerical solution discussed above.

## 5.8 Conclusion

The "cascaded acceleration" technique proposed in this contribution seems promising. Its main advantage is the low amount of RF components. The scheme still has several challenges to overcome before its viability is fully assessed. These challenges include investigating the scaling between bunch parameters (e.g. charge, laser spot size etc) with appropriate

choice of RF-gun, the investigation of transverse emittance growth, the improvement of transformer ratio (possibly using shaped photocathode laser as explored in Ref. [119]), and the investigation, via start-to-end simulation of possible options to select the accelerated population of the bunch (for further use in an inverse Compton scattering process). In addition, we have recently implemented the simulation in a particle-in-cell finite difference time-domain model based on WARP to confirm the preliminary work carried with ASTRA. Finally, the operation of the proposed compact accelerator at high-repetition rates (limited by the RF gun) will have to be explored. Finally we primitively explored the possibility of generating a tapered structure to lock the phase velocity of laser-generated THz pulse in a structure with an accelerating electron. Our theoretical results indicate it may be possible to generate such a structure by varying the gap and dielectric thickness size along the longitudinal axis of the structure. We also discuss our first experimental results of a laser-based THz generation scheme and our measurement of dispersion in a slab-symmetric structure.

## CHAPTER 6

### CONCLUSION

Next generation colliders and light sources will require high energy electron beams which will either require significant increases in footprints based on conventional acceleration approaches (e.g. RF-based), or require alternative acceleration techniques. One approach we have discussed is beam-driven acceleration using dielectric-lined waveguides (DLW) which are capable of sustaining significantly larger accelerating fields ( $E_+ \mathcal{O}(GV/m)$ ). Additionally DLWs are relatively inexpensive compared to conventional RF technology.

An important figure of merit in beam-driven acceleration is the transformer ratio  $\mathcal{R}$  which is proportional to the efficiency of acceleration and depends exclusively on the longitudinal current profile of a drive bunch. While several longitudinal current profiles had been suggested to produce large  $\mathcal{R}$  and  $E_+$ , the discontinuous nature of proposed profiles are experimentally challenging and required advanced beam manipulation techniques and transverse masks. We proposed several new smooth longitudinal current profiles as well as two new shaping techniques which could support high-repetition rate machines based. In the first technique was experimentally demonstrated at the FLASH facility and is based on using a 3.9 GHz linearizer to impart an energy modulation to generate an asymmetric and transformer enhanced drive bunch. In the second proposed technique, we showed that a longitudinally shaped laser pulse could be used to generate the quadratic-ramp distribution we discovered.

We also discussed the use of DLWs for ballistic bunching and beam-manipulation. Generally bunch-compression is done using a magnetic chicane which requires an initial energy chirp, or via ballistic bunching where usually an RF field operated at 0-crossing imparts a

linear field across the bunch; at low energy this leads to compression over a drift. We proposed the use of a DLW to impart an energy chirp directly from the self-wake of a bunch; as shown through calculations, this technique is quite feasible for low-energy bunches ( $> 10$  MeV) with peak-currents of  $\sim 100$  A (corresponding to 1 nC bunches from a photoinjector). This technique could be very useful for electron diffraction for example.

We also looked at alternative applications using DLWs for compact X-ray sources and possibly EEHG at low-energy. In the former scheme, we proposed the use of two DLWs; the first to generate ballistic bunching to increase the charge density of the bunch for a DWFA scheme in a second DLW. The technique could in principle increase the beam energy by a factor of  $\mathcal{R}$  and possibly generate X-rays with the inclusion of a laser for inverse Compton scattering. Moreover we looked at the use of DLWs and drifts to replace energy modulators and chicanes respectively in a conventional EEHG approach. This technique could in principle also work well at low energy to generate THz radiation from photoinjected bunches. Finally we briefly discussed the possible use of DLWs as an electron gun (a THz-gun) based on a laser-driven THz source. At low energy an accelerating electron in a single-cycle THz-pulse will incur a large phase-slippage from mismatches in phase velocity of the travelling mode and its increasing velocity. We briefly investigated the possibility of a longitudinally tapered DLW to match the phase acceleration of the mode with the accelerating electron bunch.



## REFERENCES

- [1] E. Haussecker and A. Chao. *Physics in Perspective*, 13:146, 2011.
- [2] V. Shiltsev. *Physics-Uspekhi*, 55.10:965, 2012.
- [3] V. Shiltsev. *JINST*, 9:T07002, 2014.
- [4] G. A. Voss and T. Weiland. Particle acceleration by wakefields. *DESY-M-82-10*, 1982.
- [5] P. B. Wilson. Introduction to wake fields and wake potentials. *SLAC-PUB-4547 and SLAC/AP-66, unpublished reports available from the Stanford Linear Accelerator Center*, 1989.
- [6] M. Rosing and W. Gai. *Phys. Rev. D*, 42:1829, 1990.
- [7] W. K. H. Panofsky and W. A. Wenzel. *Rev. Sci. Instrumentation*, 27:967, 1956.
- [8] A. Zholents, W. Gai, R. Limberg, J. G. Power, Y.-E Sun, C. Jing, A. Kanareykin, C. Li, C. X. Tang, D. Yu Shchegolkov, and E. I. Simakov. A collinear wakefield accelerator for a high-repetition-rate multi-beamline soft x-ray fel facility. *Proceedings of the 2014 Free-Electron Laser conference (FEL14)*, 2014.
- [9] A. Tremaine, J. Rosenzweig, and P. Schoessow. *Phys. Rev. E*, 56:7204, 1997.
- [10] D. Mihalcea, P. Piot, and P. Stoltz. *Phys. Rev. ST Accel. Beams*, 15:081304, 2012.
- [11] Liling Xiao, Wei Gai, and Xiang Sun. *Phys. Rev. E*, 65:016505, 2001.
- [12] R. E. Collin. Field theory of guided waves. 1960.

- [13] J. T. Bernhard and W. T. Joines. *1995 Journal of Microwave Power and Electromagnetic Energy*, 30:2, 1995.
- [14] R. D. Ruth, A. Chao, P. L. Morton, and P. B. Wilson. *Part. Accel.*, 17:171, 1985.
- [15] V. V. Tsakanov. *Nucl. Instrum. Meth. Phys. Res. Sec. A*, 432:202–, 1999.
- [16] J.G. Power, W. Gai, and P. Schoessow. *Phys. Rev. E*, 60:6061, 1999.
- [17] C. Jing, A. Kanareykin, J. G. Power, M. Conde, Z. Yusof, P. Schoessow, and W. Gai. *Phys. Rev. Lett.*, 98:144801, 2007.
- [18] K. L. F. Bane, P. Chen, and P. B. Wilson. On collinear wakefield acceleration. *SLAC-PUB-3662*, 1985.
- [19] B. Jiang, C. Jing, P. Schoessow, J. Power, and W. Gai. *Phys. Rev. ST Accel. Beams*, 15:011301, 2012.
- [20] P. Muggli, V. Yakimenko, M. Babzien, E. Kallos, and K. P. Kusche. *Phy. Rev. Lett.*, 101:054801, 2008.
- [21] P. Piot, Y.-E Sun, J. G. Power, and M. Rihaoui. *Phys. Rev. ST Accel. Beams*, 14:022801, 2011.
- [22] Y.-E Sun, P. Piot, A. Johnson, A. H. Lumpkin, T. J. Maxwell, J. Ruan, and R. Thurman-Keup. *Phys. Rev. Lett.*, 105:234801, 2010.
- [23] G. Ha, M.E. Conde, W. Gai, C.-J. Jing, K.-J. Kim, J.G. Power, A. Zholents, M.-H. Cho, W. Namkung, and C.-J. Jing. *Proceedings of the 2014 International Particle Accelerator Conference*, 1506, 2014.

- [24] F. Lemery and P. Piot. Alternative shapes and shaping techniques for enhanced transformer ratios in beam driven techniques. *Proceedings of the 16th Advanced Accelerator Concepts Workshop (AAC 2014)*, 2014.
- [25] F. Lemery, D. Mihalcea, and P. Piot. *Proceedings of the 2012 International Particle Accelerator Conference*, 3012, 2012.
- [26] D. T. Palmer, R. H. Miller, H. Winick, X.J. Wang, K. Batchelor, M. Woodle, and I. Ben-Zvi. Microwave measurements of the bnl/slac/ucla 1.6-cell photocathode rf gun. *Proceedings of the 1995 Particle Accelerator Conference (PAC95)*, 982, 1996.
- [27] K. Flöttmann. ASTRA: *A space charge algorithm, user's manual*. <http://www.desy.de/~simfpyflo/AstraDokumentation>.
- [28] F. Lemery and P. Piot. *Proceedings of the 2014 International Particle Accelerator Conference (IPAC14)*, 1454, 2014.
- [29] O. J. Luiten, S. B. van der Geer, M. J. de Loos, F. B. Kiewiet, and M. J. van der Wiel. *Phys. Rev. Lett.*, 93:094802, 2004.
- [30] A. M. Wiener. *Rev. Sci. Instrum.*, 71:1929, 2000.
- [31] J. W. Gibbs. *Nature*, 59:1539, 1899.
- [32] P. Piot, Y.-E Sun, T. J. Maxwell, J. Ruan, E. Secchi, and J. C. T. Thangaraj. *Phys. Rev. ST Accel. Beams*, 16:010102, 2013.
- [33] G. Ferrini, P. Michelato, and F. Parmigiani. *Solid State Commun.*, 106:21, 1998.
- [34] B. Aunes et al. *Phys. Rev. ST Accel. Beams*, 3:092001, 2000.
- [35] R. Legg, W. Graves, T. Grimm, and P. Piot. *Proceedings of the 2008 European Particle Accelerator Conference (EPAC08)*, 469, 2008.

- [36] *J. Bisognano, M. Bissen, R. Bosch, M. Efremov, D. Eisert, M. Fisher, M. Green, K. Jacobs, R. Keil, K. Kleman, G. Rogers, M. Severson, D. D. Yavuz, R. Legg, R. Bachimanchi, C. Hovater, T. Plawski, and T. Powers.* Proceedings of the 2013 North-American Particle Accelerator Conference (NAPAC'13), 622, 2013.
- [37] *J. Bisognano, R. A. Bosch, D. Eisert, M. V. Fisher, M. A. Green, K. Jacobs, K. J. Kleman, J. Kulpin, and G. C. R. Edit.* Proceedings of 2011 Particle Accelerator Conference (PAC11), 2444, 2011.
- [38] *K. Flöttmann, T. Limberg, , and P. Piot.* Generation of ultrashort electron bunches by cancellation of nonlinear distortions in the longitudinal phase space. DESY report TESLA FEL 2001-06, 2001.
- [39] *N. Solyak, I. Gonin, H. Edwards, M. Foley, T. Khabiboulline, D. Mitchell, J. Reid, and L. Simmons.* Proceedings of the 2003 Particle Accelerator Conference (PAC03), 1213, 2003.
- [40] *M. Borland and H. Shang.* GENETICOPTIMIZER, private communication, 2005.
- [41] *P. Emma.* Bunch compressor options for the new tesla parameters. Internal unpublished report DAPNIA/SEA-98-54 available from Service des Accélérateurs, 1998.
- [42] *T. Limberg, Ph. Piot, and F. Stulle.* Proceedings of the 2002 European Particle Accelerator Conference (EPAC2002), 1544, 2002.
- [43] *T. Smith.* Proceedings of the 1984 Linear Accelerator Conference (LINAC'84), SLAC report, 303:421, 1986.
- [44] *D. H. Dowell, J. L. Adamski, T. D. Hayward, C. G. Parazzoli, and A. M. Vetter.* Nucl. Instrum. Meth., A375:108, 1996.

- [45] *W. Ackermann and et al.* Nature Photonics, *1:336*, 2007.
- [46] *P. Piot, Y.-E Sun, T. J. Maxwell, J. Ruan, A. H. Lumpkin, M. M. Rihaoui, and R. Thurman-Keup.* Appl. Phys. Lett., *98:261501*, 2011.
- [47] *C. Behrens and C. Gerth.* Proceedings of the 2010 free-electron laser conference (FEL10), *133*, 2010.
- [48] *E. Saldin, E. Schneidmiller, and M. Yurkov.* Nucl. Instrum. Methods Phys. Res., *Sect. A (539):499*, 2005.
- [49] *M. Dohlus and T. L. Limberg.* Proceedings of the 2004 free-electron laser conference (FEL04), *18*, 2004.
- [50] *W. Gai, P. Schoessow, B. Cole, R. Konecny, J. Norem, J. Rosenzweig, and J. Simpson.* Phys. Rev. Lett., *61:2756*, 1988.
- [51] *C. Nieter and J. R. Cary.* J. Comp. Phys., *169:448*, 2008.
- [52] *M. Ferrario and L. Serafini.* AIP Conference Proceedings, *581:87*, 2001.
- [53] *R. Brinkmann, Y. Derbenev, and K. Flöttmann.* Phys. Rev. ST Accel. Beams, *4:053501*, 2001.
- [54] *K.-J. Kim.* Phys. Rev. ST Accel. Beams, *6:104002*, 2003.
- [55] *Y.-E Sun and et al.* Phys. Rev. ST Accel. Beams, *7:123501*, 2004.
- [56] *P. Piot and et al.* Phys. Rev. ST Accel. Beams, *9:031001*, 2006.
- [57] *P. Piot and et al.* Proceedings of IPAC10, *4316*, 2010.
- [58] *C. Prokop D. Mihalcea and P. Piot.* Proceedings of the International Particle Accelerator Conference (IPAC13), *2003:TUPWO060*.

- [59] *C. Prokop and P. Piot.* Proceedings of the International Particle Accelerator Conference (IPAC13), *3103:THOBB101*.
- [60] *Y.-M. Shin and et al.* Proceedings of International Particle Accelerator Conference (IPAC2014), *TUPME061, 2014*.
- [61] *J. Zhu and et al.* Fermilab-PUB-14-103-AD-APC, *2014*.
- [62] *J. Qiang and et al.* Phys. Rev. ST AB, *9:044204, 2006*.
- [63] *M. Borland.* Advanced Photon Source LS-287, *2000*.
- [64] *A. H. Zewail and J. M. Thomas.* 4D Electron Microscopy: Imaging in Space and Time. *Imperial College Press, London, 2010*.
- [65] *R. K. Li, P. Musumeci, H. A. Bender, N.S. Wilcox, and M. Wu.* J. Appl. Phys., *110:(7), 074512, 2011*.
- [66] *A. Gover.* Phys. Rev. ST Accel. Beams, *8:030701, 2005*.
- [67] *A.-S. Müller.* Rev. Accl. Sci. Tech., *03:165, 2010*.
- [68] *D.F. Gordon, A. Ting, T. Jones, B. Hazi, R.F. Hubbard, and P. Sprangle.* *Particle-in-cell simulation of optical injector for plasma accelerators.* Proceedings of the 2003 Particle Accelerator Conference (PAC'03), *1846, 2003*.
- [69] *A. Modena, Z. Najmudin, A.E. Dangor, C.E. Clayton, K.A. Marsh, C. Joshi, V. Malka, C.B. Darrow, C. Danson, D. Neely, and F.N. Walsh.* Nature, *377:606, 1995*.
- [70] *B. E. Carlsten and S. M. Russel.* Phys. Rev. E, *53:R2072–R2075, 1996*.
- [71] *X. J. Wang, X. Qiu, and I. Ben-Zvi.* Phys. Rev. E, *54:R3121, 1996*.

- [72] *X. J. Wang and X. Y. Chang.* Nucl. Instr. Meth. A, 507:310, 2003.
- [73] *P. Piot, L. Carr, W. S. Graves, and H. Loos.* Phys. Rev. ST Accel. Beams, 6:033503, 2003.
- [74] *M. Ferrario et al.* Phys. Rev. Lett., 104:054801, 2010.
- [75] *K. Flöttmann.* Nucl. Instr. Meth. A, 740:34, 2014.
- [76] *C. Sung, S. Ya. Tochitsky, S. Reiche, J. B. Rosenzweig, C. Pellegrini, and C. Joshi.* Phys. Rev. ST Accel. Beams, 9:120703, 2014.
- [77] *L. J. Wong, A. Fallahi, and F. X. Kärtner.* Optics Express, 21:(8), 9792, 2013.
- [78] *Y.-C. Huang.* Int. Jour. Mod. Phys. B, 21:287, 2007.
- [79] *M. Bolosco, I. Boscolo, F. Castelli, S. Cialdi, M. Ferrario, V. Petrillo, and C. Vaccarezza.* Nucl. Instr. Meth. A, 577:409, 2007.
- [80] *Y. Li and K.-J. Kim.* Appl. Phys. Lett., 92:014101, 2008.
- [81] *P. Musumeci, R. K. Li, and A. Marinelli.* Phys. Rev. Lett., 106:184801, 2011.
- [82] *S. Antipov, C. Jing, M. Fedurin, W. Gai, A. Kanareykin, K. Kusche, P. Schoessow, V. Yakimenko, and A. Zholents.* Phys. Rev. Lett., 108:144801, 2012.
- [83] *D. R. Hamilton, J. K. Knipp, and J. B. Horner Kuper.* MIT Radiation Laboratory Series, *Klystron and Microwave Triodes.* McGraw-Hill, New York, 1948.
- [84] *B. C. Yunn.* *Physics of the jlab 350-kev photoinjector.* Proceedings of the 1999 Particle Accelerator Conference, PAC'99, 2453, 1999.

- [85] Z. Huang, D. Dowell, P. Emma, and C. Limborg-Duprey. *Uncorrelated energy spread and longitudinal emittance of a photoinjector beam*. Proceedings of the Particle Accelerator Conference, (PAC2005), 3570, 2005.
- [86] M. Hüning and H. Schlarb. *Measurements of the beam energy spread in the ttf photoinjector*. Proceedings of the 2003 Particle Accelerator Conference (PAC03), 2074, 2003.
- [87] M. Dohlus, K. Flöttmann, and C. Henning. *Fast particle tracking with wake fields*. DESY 12-02 (available from DESY Hamburg, Germany), 2012.
- [88] H. Boersch. *Z. Phys.*, 139:115, 1954.
- [89] J. S. Nodvick and D. S. Saxon. *Phys. Rev.*, 96:180, 1954.
- [90] B. Dwersteg and et al. *Nucl. Instr. Meth. A*, 393:93, 1997.
- [91] P. Musumeci, R. K. Li, K. G. Roberts, and E. Chiadroni. *Phys. Rev. ST Accel. Beams*, 16:100701, 2013.
- [92] A. M. Cook, R. Tikhoplav, S. Y. Tochitsky, G. Travish, O. B. Williams, and J. B. Rosenzweig. *Phys. Rev. Lett.*, 103:095003, 2009.
- [93] J.-P. Carneiro, N. Barov, H. Edwards, M. Fitch, W. Hartung, K. Floettmann, S. Schreiber, and M. Ferrario. *Phys. Rev. ST Accel. Beams*, 8:040101, 2005.
- [94] J. Andruszkow and et al. [TESLA Collaboration]. *Phys. Rev. Lett.*, 85:3825, 2000.
- [95] C. Adolphsen et al. 1:2, 2000.
- [96] P. Piot, C. Behrens, C. Gerth, M. Dohlus, F. Lemery, D. Mihalcea, P. Stoltz, and M. Vogt. *Phys. Rev. Lett.*, 108:034801, 2012.



- [97] *M. Hüning, H. Schlarb, P. Schmüser, and M. Timm.* Phys. Rev. Lett., 88:074802, 2012.
- [98] *P. Emma, M. Venturini, K. L. F. Bane, G. Stupakov, H.-S. Kang, M. S. Chae, J. Hong, C.-K. Min, H. Yang, T. Ha, W. W. Lee, C. D. Park, S. J. Park, and I. S. Ko.* Phys. Rev. Lett., 112:034801, 2014.
- [99] *G. Mishra and G. Sharma.* Progress In Electromagnetics Research M, 36:47, 2014.
- [100] *G. Travish.* AIP Conf. Proc., 1507:85, 2013.
- [101] *W. S. Graves and et al.* Phys. Rev. ST Accel. Beams, 17:120701, 2014.
- [102] *N. D. Powers and et al.* Nature Photonics, 8:28, 2014.
- [103] *L. J. Wong and et al.* Optics Express, 21:(8), 9792, 2014.
- [104] *E. Nanni and et al.* 2014.
- [105] *F. Lemery and P. Piot.* Phys. Rev. ST Accel. Beams, 17:112804, 2014.
- [106] *J. Hebling et al.* Opt. Exp., 21:1161, 2002.
- [107] *K. Ravi et al.* Opt. Exp., 23:(4), 5253–5276, 2014.
- [108] *X. Wu et al.* Opt. Lett., 39:(18), 5403–5406, 2014.
- [109] *E. Nanni et al.* Proceedings of International Particle Accelerator Conference (IPAC2014), 2014.
- [110] *C. Li and et al.* Phys. Rev. ST Accel. Beams, 17:091302, 2014.
- [111] *J. A. Fülöp et al.* Opt. Lett., 37:4, 2012.
- [112] *Y. Li.* Applied Physics Letters, 88:251108, 2006.

- [113] *E. A. Peralta and et al.* Nature, 2013.
- [114] *J. Breuer and P. Hommelhoff.* Phys. Rev. Lett., 111:134803, 2013.
- [115] *L. Wimmer et al.* 2013.
- [116] *W. R. Huang and et al.* 2014.
- [117] *G. Travish et al.* Proceedings of the European Particle Accelerator Conference (EPAC08), 2927, 2008.
- [118] *Y. Ding et al.* Phys. Rev. Lett., 102:254801, 2009.
- [119] *F. Lemery and P. Piot.* Submitted to Phys. Rev. ST Accel. Beams, 2014.
- [120] <http://www.nvidia.com/object/tesla-supercomputing-solutions.html>.
- [121] <http://www.amd.com/us/products/server/processors/6000-series-platform/Pages/6000-series-platform.aspx>.

## **APPENDIX**

### **PERFORMANCES OF VORPAL-GPU SLAB-SYMMETRIC DLW**

## A.1 Introduction

The development of computational power in the past several decades has led to our capability to solve complicated problems numerically, which would otherwise be very difficult or impossible.

The rapid pace at which processor architecture evolves must be matched with improvements in program/software design to take advantage of the full capability of a processing unit. The most recent development include the deployment of hardware with large numbers of Graphical Processing Units (GPU). GPU's and their highly parallel structure makes them more effective than general-purpose Central Processing Units (CPUs) for algorithms where processing of large blocks of data is done in parallel.

Although a CPU is faster than a GPU on a per-core basis, each GPU may contain several thousand cores [120] while each CPU is presently limited to 16 cores [121]. Moreover, GPUs are capable of processing many parallel streams of data simultaneously which makes them highly efficient for parallel computation. Finally GPUs are capable of performing vector operations and double-precision floating-point numbers, which makes them useful in electromagnetic simulations such as VORPAL [51].

VORPAL is a three-dimensional electromagnetic and electrostatic PIC code. VORPAL uses a conformal finite difference-time domain (FDTD) method to solve Maxwell's equations and that includes an advanced technique known as cut-cell boundaries to allow accurate representation of curved geometries within a rectangular grid.

To test the scalability of VORPAL-GPU on a recently acquired TOP1000-grade hybrid GPU/CPU, "Gaea," we use a familiar problem on collinear beam driven wakefield acceleration. The GAEA computing cluster at NIU includes 60 compute nodes with 3 additional nodes to handle disk and terminal services. Each compute node contains 2 hex core CPUs

(Intel Xeon X5650 operating at 2.67 GHz), 72 GB of RAM, 2 TB of local storage and 2 GPU cards. Each GPU card is an NVIDIA TESLA M2070 capable of 515 Gigafllops of double precision floating point arithmetic, 1030 Gigafllops of single precision floating point arithmetic, each GPU card has 448 CUDA cores, with access to 6 GB of GDDR5 memory, and 150 GB/s memory bandwidth. The cluster also possesses approximately 192 TB of disk storage accessible to all compute nodes. Lastly, the compute nodes and storage nodes are interconnected with a 40 Gb/s QDR INFINIBAND network.

## A.2 Problem Setup

We explored the scaling of a dielectric wakefield accelerator (DWFA) simulation using VORPAL-GPU. In DWFA's a drive bunch is used to excite an electromagnetic wake in a dielectric-lined waveguide (DLW). The trailing wake can be used to accelerate a properly timed witness bunch. Currently VORPAL-GPU does not support particle-in-cell functionalities, instead the electron bunch is modeled by the time-dependent current density

$$\vec{J}(x, y, z, t) = \frac{cQ(2\pi)^{-\frac{3}{2}}}{\sigma_x\sigma_y\sigma_z} e^{\left(-\frac{z^2}{2\sigma_z^2} - \frac{y^2}{2\sigma_y^2} - \frac{(x-ct)^2}{2\sigma_x^2}\right)} \hat{x}, \quad (\text{A.1})$$

where the charge  $Q = 1$  nC, the transverse sizes are  $\sigma_x = \sigma_y = 30\mu m$ , the longitudinal size is  $\sigma_z = 100\mu m$  and  $c$  is the speed of light.

The computational domain associated to the problem appears in Fig. A.1. The current distribution enter the computation domain from  $x = 0$  time  $t = 0$  and propagates through the structures until it exists on the  $x >$  side. The boundaries on the  $y$  and  $z$  sides are perfectly conducting boundary (PCB) to mimic the conducting plates surrounding the DLW. In addition, perfectly matched layers (PMLs) are use on both ends ( $x$ ) of the structure to

mimic an open boundary and avoid spurious reflection of the electromagnetic field generated by the current distribution.

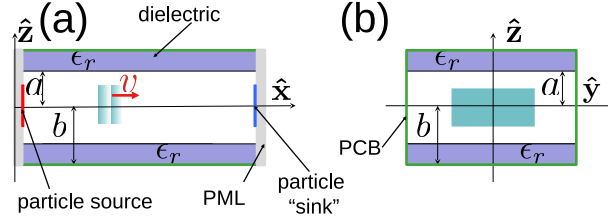


Figure A.1: A diagram of the slab seen from the y-transverse direction (a) and the from the x-longitudinal direction (b). The slab is composed of a dielectric coating with dielectric permittivity  $\epsilon_r$  surrounded by a PCB. In the VORPAL simulation, we use a wave launcher to drive a short pulse in  $z$ . Lastly, to remove reflections and to artificially produce the pulse leaving the structure we implement a PML. We record the signal on axis, near the PML.

In this problem, Maxwell's equation were solved using VORPAL's **FieldCombo** algorithm and because of the dielectric medium the updated included the construction and update of the  $\epsilon$  permittivity matrix necessary to define and update the  $\vec{D}$  electric-displacement field components.

### A.3 Scaling studies

In high-performance computing, there are generally two figure of merits used to describe scaling performance: the strong and weak scalings. Strong scaling refers to how the solution time changes for a parallel computation with a fixed computational volume. Weak scaling refers to how the solution time changes for a fixed parallel computation with different computational volumes. With respect to VORPAL-GPU, we are interested in knowing the cost of the solution time per processor(s) for an increase in resolution (finer grid).

A larger number of processors will not necessarily decrease the solution time; instead this relationship depends on many factors and is problem specific. Examples of such factors

include, e.g., (i) increase in time to split the jobs to more cores (ii) increase in time to send information to more cores (iii) increase in time to allocate less memory to more cores (iv) and the finite bandwidth available to communicate between the cores.

In VORPAL-GPU we use a cartesian grid  $(N_X, N_Y, N_Z)$  to describe number of cells in  $\hat{x}, \hat{y}, \hat{z}$  directions (see Tab. A.1). To improve the scaling capability, it was important to choose the decomposition of the grid wisely.

The simulation was designed such that the electron bunch propagation direction was in the long, longitudinal direction of the simulation ( $\hat{x}$ ). This was a convenient choice which enabled several clear benefits. First it allows for a simple one dimensional decomposition of the gridded field quantities. This leads to a simple messaging pattern of the quantities in the halo—that is each GPU sends and receives data only from the other GPUs on each side of the decomposition. This choice leads to a minimization of the messaging costs leading to optimal efficiency. Moreover, VORPAL-GPU is designed such that the x-dimension represents the slowest dimension in the memory layout of the field quantities while the z-dimension is the fastest. This is a very important choice which enables contiguous chunks of memory in the planes perpendicular to the x-axis (i.e. the halo guard cell planes) to be transferred back to the host in a single memory transfer across the PCI Express bus. This yields the optimal performance as it enables one to effectively overlap communication costs with the update of the main "body" region on each GPU.

However, one must also be careful to choose the dimensions of the simulation domain carefully. Even a simple one-dimensional domain decomposition can perform poorly if the ratio of the cells needing to be messaged to the cells needing to be updated in the body region is too large.

Because we decompose in the  $\hat{x}$  direction, our message volume will be  $2N_Y N_Z$ . For a problem involving  $N$  GPUs, our update volume will be  $\frac{N_X N_Y N_Z}{N}$ . When  $\frac{2N_Y N_Z}{(N_X * N_Y * N_Z)/N}$  becomes large (i.e. greater than .02) we expect the performance to degrade substantially. In

these situations, the amount of work in the body update region will be too small to effectively hide the communication costs. In particular, the body update region kernels will simply run too fast to hide these costs.

Table A.1: Cartesian grid dimensions and volumes used in this scaling study.

Size	NX	NY	NZ	Volume
S	602	128	128	9863168
M	1552	256	256	101711872
L	7752	256	256	508035072
XL	3852	512	512	1009778688
XXL	7702	512	512	2019033088
XXXL	5002	768	768	2950299648

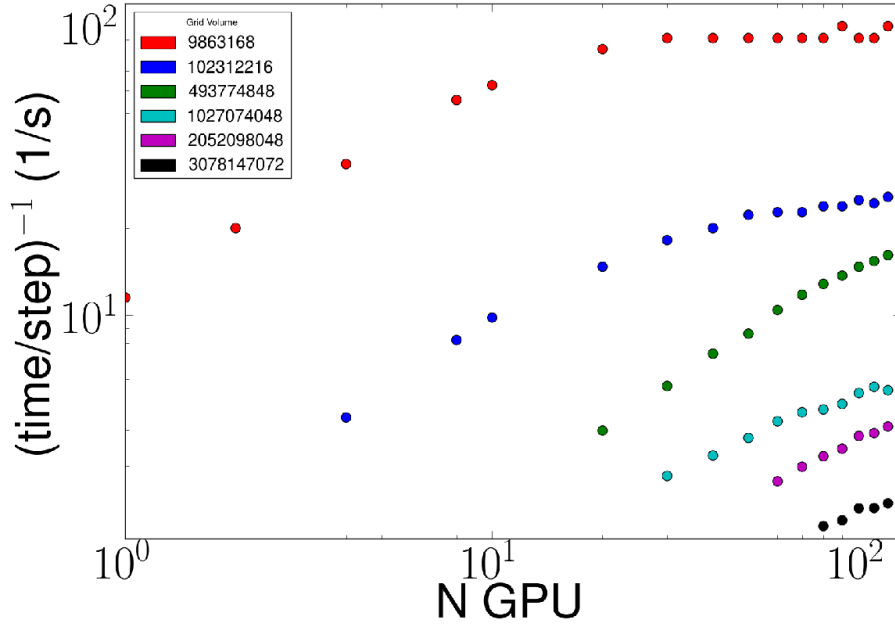


Figure A.2: Strong and weak scaling of VORPAL-GPU on GAEA. On the horizontal, N GPU refers to the number of GPUs used for a given simulation (see below for list). The vertical axis shows the inverse of the time per step.



We investigated the scaling over 1, 2, 4, 8, 10, 20, 30, 40, 50, 60, 70, 80, 90, 100, 110, 120 GPUs. However, because of the limited memory on each GPU, larger problems cannot run on a smaller number of GPUs. The results are presented in Fig. A.2. In each case, several hundred steps were taken and we use the minimum time per step; an alternative method would be to take the average time per step over the run sample, however the loading and dumping time of the larger volumes skews this data significantly. In this figure, the volume curves represent the strong scaling, while the weak scaling is presented by the different volume sizes for a fixed number of GPUs (i.e. vertical points). We see linear scaling up to certain numbers of GPUs for each volume, after which it falls off. The fall off comes from the aforementioned changing update and communication volume ratios.

## A.4 Comparison and Conclusion

For comparison we benchmarked VORPAL-GPU with an analytical model based on Ref. [9, 10]. We see very good agreement and notice convergence of better resolution toward the analytical model (see Fig. A.3). We also confirmed accordance between both gpu, and cpu versions of VORPAL.

Some of the transverse and longitudinal characteristics of the wakefields produced in these simulations are nearly impossible to see at low resolution, therefore the powerful capability of VORPAL on GAEA, allows us to potentially do optimization studies due to the small runtimes needed for large scale problems (see Fig. A.4).

The next decades in computational development, both in hardware and software will lead to faster, more powerful computation capabilities; which, will make possible the optimization of large scale problems and large data analysis.

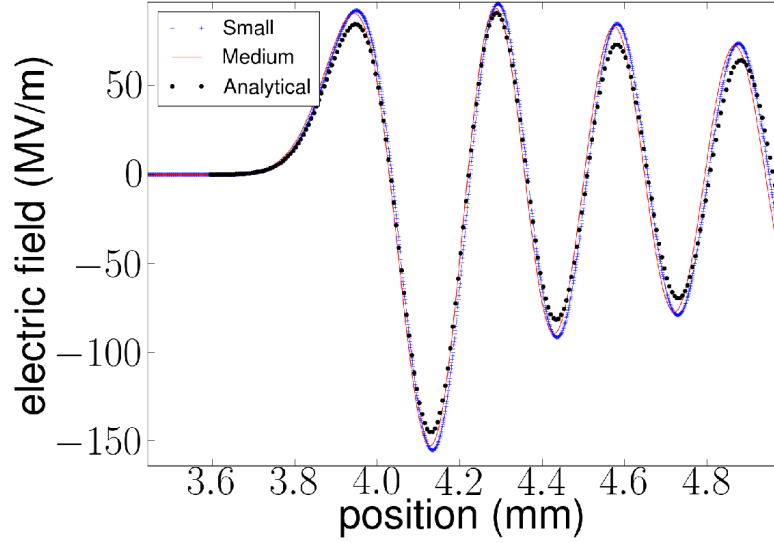


Figure A.3: Comparison plot between VORPAL-GPU and an analytical code. The small and medium volume sizes correspond to the first two volumes in Tab. tab:gridsize. The structure has dimensions  $a = 100\mu m$  with  $b = 120\mu m$  with  $\epsilon = 5.7$ .

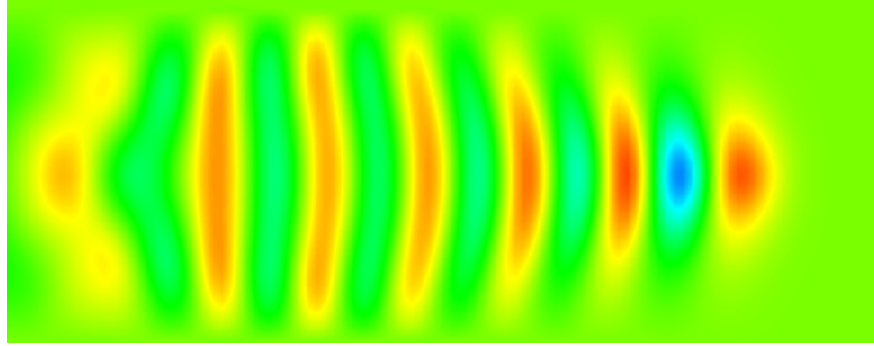


Figure A.4: A contour plot of the simulation carried out with VORPAL-GPU shown from a slice in  $z=0$  plane on a L grid volume. A gaussian bunch ( $1nC$ ,  $\sigma_x = 100\mu m$ ) passes through a dielectric structure exciting a wake. The transverse-extended shape corresponds to the combination of the LSE and LSM modes. The peak accelerating field (blue) corresponds to  $150 MV/m$ . The structure has dimensions  $a = 100\mu m$  with  $b = 120\mu m$  with  $\epsilon = 5.7$ .

We are thankful to Dr. Clyde Kimbal for his support and Dave Ulrick for his help with the GAEA cluster.